HELSINKI UNIVERSITY OF TECHNOLOGY

Faculty of Electronics, Communications and Automation

Department of Radio Science and Engineering

Aki Karttunen

Design of feed systems for hologram-based compact antenna test ranges

The thesis was submitted in partial fulfilment for the degree of Licentiate of Science in Technology in Espoo,

Supervisor

Professor Antti Räisänen

Second examiner

Pasi Ylä-Oijala, Ph.D.

Author: Aki Karttunen

Name of the Thesis: Design of feed systems for hologram-based compact antenna test ranges

Date: August 26, 2009 **Number of pages:** 106

Faculty: Faculty of Electronics, Communications and Automation

Professorship: Radio Engineering

Supervisor: Professor Antti Räisänen

Second examiner: Pasi Ylä-Oijala, Ph.D.

A designing method for feed systems for hologram-based compact antenna test ranges (CATR) is developed. A hologram-based CATR can be used to test large antennas at millimetre and submillimetre wavelengths. Feed systems are used to provide a modified illumination for the hologram. Using the modified illumination from a feed system, narrow slots can be avoided in the hologram pattern. Narrow slots are difficult to manufacture accurately and limit the polarisation properties of the hologram.

Feed systems use two shaped reflector or lens surfaces to shape the radiation pattern of a feed horn. The shaped surfaces are calculated with a ray-tracing based synthesis method and iteratively optimised based on simulation results. This synthesis method was previously used to design a 310 GHz dual reflector feed system (DRFS). In this work a 650 GHz DRFS is designed as part of large antenna measurement campaign in which a large antenna was tested in a hologram-based compact antenna test range. The DRFS is measured by near-field scanning with a planar scanner at 650 GHz. The measured amplitude ripple is about 0.8 dB peak-to-peak and the phase ripple is about 15° peak-to-peak. These measurements prove that no significant design or manufacturing errors were made.

The feed system design and synthesis method has been extended also for feed systems based on shaped dielectric lenses. A dual lens feed system design example is designed, with same design goals as those with the 650 GHz DRFS. The design example proves that the synthesis method can be used also for feed systems based on shaped lenses.

In this thesis, the designing method for feed systems based on either shaped reflector or lenses is presented. A 650 GHz DRFS is designed, tested, and used in a hologram-based CATR.

Keywords: feed system, geometrical optics (GO), ray tracing, shaped lens antenna, shaped reflector antenna, sub-millimetre wavelengths, synthesis

Tekijä: Aki Karttunen

Työn nimi: Syöttöjärjestelmien suunnittelu hologrammiin perustuviin kompakteihin antennimittauspaikkoihin

Päivämäärä: 26.08.2009 **Sivumäärä:** 106

Tiedekunta: Elektroniikan, tietoliikenteen ja automaation tiedekunta

Professuuri: Radiotekniikka

Työn valvoja: Professori Antti Räisänen

Toinen tarkastaja: Pasi Ylä-Oijala, Ph.D.

Tässä työssä kehitetään syöttöjärjestelmien suunnittelumenetelmä hologrammiin perustuviin kompakteihin antennimittauspaikkoihin. Hologrammiin perustuvaa antennimittauspaikkaa voidaan käyttää suurten antennien testaamiseen millimetri- ja alimillimetriaaltoalueella. Syöttöjärjestelmiä käytetään muotoillun valaisun aikaan saamiseksi hologrammille. Kun käytetään muotoiltua valaisua voidaan välttää kapeat raot hologrammissa. Kapeat raot ovat vaikeita valmistaa tarkasti ja rajoittavat hologrammin polarisaatio-ominaisuuksia.

Syöttöjärjestelmässä käytetään kahta muotoiltua heijastin- tai linssipintaa syöttötorven säteilykuvion muokkaamiseen. Muotollut pinnat lasketaan säteenseurantaan perustuvalla synteesimenetelmällä ja optimoidaan iteratiivisesti simulaatiotulosten perusteella. Tätä synteesimenetelmää on aiemmin käytetty kaksiheijastimisen syöttöjärjestelmän suunnitteluun 310 GHz:lle. Tässä työssä kaksiheijastiminen syöttöjärjestelmä suunnitellaan 650 GHz:lle osana isoa antennimittaus kampanjaa, jossa mitataan suurikokoinen antenni hologrammiin perustuvassa anitennimittauspaikassa. Suunniteltu syöttöjärjestelmä mitataan planaarisella lähikenttämittauksella 650 GHz:n taajuudella. Mitattu amplitudivaihtelu on 0,8 dB huipusta huippuun ja vaihevaihtelu on noin 15° huipusta huippuun. Mittaukset osoittavat, että merkittäviä suunnittelu- tai valmistusvirheitä ei ole tehty.

Syöttöjärjestelmäsuunnittelu ja synteesimenetelmä yleistetään myös dielektrisiin linsseihin perustuville syöttöjärjestelmille. Kaksilinssinen syöttöjärjestelmä suunnitellaan samoilla suunnittelutavoitteilla kuin 650 GHz:n kaksiheijastiminen syöttöjärjestelmä. Tämä suunnitelu esimerkki todistaa, että kyseistä suunnittelumenetelmää voi käyttää myös linsseihin perustuvien syöttöjärjestelmien suunnitteluun.

Tässä työssä esitetään suunnittelumenetelmä muotoiltuihin linsseihin tai heijastimiin perustuville syöttöjärjestelmille. Kaksiheijastiminen syöttöjärjestelmä suunnitellaan, testataan ja sitä käytetään antennimittauksissa hologrammiin perustuvassa antennimittauspaikassa.

Avainsanat: alimillimetriaallot, geometrinen optiikka (GO), muotoiltu heijastinantenni, muotoiltu linssiantenni, synteesi, syöttöjärjestelmä, säteenseuranta

Preface

This work has been done in MilliLab, the Department of Radio Science and Engineering of Helsinki University of Technology, and partially funded by the Academy of Finland through its Centre-of-Excellence program SMARAD. This work has been done as a part of project supported by ESA, ESTEC Contract No. 19131/05/NL/LvH. VTT and Ticra are acknowledged for allowing the author to use their GRASP8W software for the simulations. The financial support of Jenny and Antti Wihuri Foundation is greatly appreciated.

I would like to thank the whole hologram CATR team. Especially I would like to thank my master's thesis instructor Janne Häkli. I am also thankful to Juha Ala-Laurinaho and Antti Räisänen for their help in preparing this thesis.

Tahdon myös kiittää Raija Aaltoa, Teuvo Aaltoa ja Reetta Lahtea tuesta ja kannustuksesta.

Espoo, August 26, 2009.

Aki Karttunen

Table of contents

List of symbols

a	Index
b	Index
e	Eccentricity
e_m	Eccentricity of a main reflector
e_s	Eccentricity of a subreflector
f_{holo}	Hologram focal length
f_{sub}	Subreflector focal length
i	Index
j	Imaginary unit
k	Wave number, index
k_0	Wave number in free-space
$\bar{k}$	Local wave vector, wave vector
l	Length, index
m_{ray}	Number of the ray
m_{tube}	Number of the ray tube
n	Index of refraction, index
n_{ray}	Number of the ray
n_{tube}	Number of the ray tube
$\bar{n}$	Normal vector
r	Distance, far-field criterion, spherical coordinate
r_{main}	Main reflector distance from the output aperture
r_{sub}	Distance between reflectors
$\bar{r}$	Vector, direction, position
s	Distance along a ray
t	Time, thickness
$\bar{t}$	Tangential vector, tangential unit vector of a ray
$\bar{u}$	Unit vector
$\bar{u}_i$	Unit vector in direction i
x, x'	Cartesian coordinate
y, y'	Cartesian coordinate
z, z'	Cartesian coordinate, cylindrical coordinate

A	Area, number of points
B	Number of points
C	Constant
D	Diameter of an antenna, diameter of an aperture
D_{holo}	Diameter of a hologram

$\overline{E}, \overline{E}_0$	Electric field
E_a	Electric field strength in aperture
E_h	Electric field strength of hologram illumination
$\overline{E}_a$	Electric field in aperture
$\overline{E}_h$	Electric field in hologram illumination
$\overline{E}_{PO}$	Electric field calculated with PO
$\overline{E}_{PTD}$	Electric field calculated with PTD
F	Focal point, phase centre point
$\overline{F}$	Function
F_{feed}	Focal point of a feed
F_{holo}	Focal point of a hologram
F_{main}	Focal point of a main reflector
G	Green's function
$\overline{\overline{G}}$	Green's dyad
$\overline{H}$	Magnetic intensity
$\overline{H}_a$	Magnetic intensity in aperture
$\overline{H}_i$	Incident magnetic intensity
$\overline{J}$	Electric current density
$\overline{J}_m$	Magnetic current density
$\overline{J}_{ms}$	Magnetic surface current density
$\overline{J}_s$	Electric surface current density
K	Number of points
L	Eikonal function, number of points
M	Number of rays in a ray ring
N	Number of ray rings, degree of Butterworth function
N_{surf}	Number of surfaces
P	Power
R	Distance, radius
S, S'	Surface
T	Total transmission coefficient
α	Scaling factor, angle between axis
α_{feed}	Feed offset angle
α_{sub}	Subreflector offset angle
β	Angle between axis
ε	Permittivity
ε_0	Permittivity of free-space

ε_r	Relative permittivity
η	Wave impedance
η_0	Wave impedance in free-space
θ	Angle
θ_{feed}	Feed horn half-beam width
θ_{main}	Output half-beam width
λ	Wavelength
μ	Permeability
μ_0	Permeability of free-space
μ_r	Relative permeability
ρ	Cylindrical coordinate, reflection coefficient
ρ_c	Half power (–3 dB) point of Butterworth function
σ	Conductivity
σ_m	Magnetic conductivity
τ	Transmission coefficient
ϕ	Cylindrical coordinate
ω	Angular frequency
Ψ	Phase

List of abbreviations

AUT	Antenna under test
CATR	Compact antenna test range
DRFS	Dual reflector feed system
ESA	European space agency
FDTD	Finite-difference time-domain
GA	Genetic algorithm
GO	Geometrical optics
JAXA	Japan aerospace exploration agency
NASA	National aeronautics and space administration
NICT	National institute of information and communications technology
NURBS	Non-uniform rational B-spline
PEC	Perfect electric conductor
PMC	Perfect magnetic conductor
PO	Physical optics
PTD	Physical theory of diffraction
QPS	Quintic pseudosplines
RAM	Radar absorbing material
RCS	Radar cross-section
RTO	Representative test object
TE	Transverse electric
TKK	Teknillinen korkeakoulu (Helsinki University of Technology)
TM	Transverse magnetic
QZ	Quiet zone

1 Introduction

Large millimetre and submillimetre wave antennas are used to study the earth and the universe at millimetre and submillimeter wavelengths. Several ongoing space research projects will study the universe at submillimetre wavelengths, e.g., Herschel (ESA) [1], [2], Planck (ESA) [1], [2], SPIRIT (NASA) [3], and SPECS (NASA) [3]. Examples of missions to study the atmosphere at submillimetre wavelengths are EOS MLS (NASA) [4], and SMILES (NICT, JAXA) [5], [6]. Electrically large reflector antennas are needed for high angular resolution. Accurate manufacturing of the reflector is very difficult and therefore the operation of the antenna should be verified with measurements prior to the launch.

A compact antenna test range (CATR) is best suited for testing large antennas at high frequencies. In a CATR, the far-field conditions, i.e., a quiet zone (QZ), needed for testing the antenna under test (AUT), are created with a collimating element. Conventionally, the collimating element in a CATR is a reflector or a set of reflectors. The highest usable frequency of a reflector-based CATR is typically limited by the surface accuracy of the reflectors.

MilliLab at TKK Helsinki University of Technology has developed a hologram-based CATR since the 1990's [7], [8]. A hologram-based CATR can be used to test large antennas at millimetre [9], [10] and submillimetre wavelengths [11], [12]. The hologram is a light weight planar structure and therefore much easier and cheaper to manufacture than the large reflectors in the conventional CATRs.

Traditionally a corrugated feed horn has been used to illuminate the hologram. Because of the high edge illumination, narrow slots have been needed at the edges of the hologram. These narrow slots are difficult to manufacture accurately and limit the use of the hologram to a polarisation parallel to the slots, i.e., the vertical polarisation. The narrow slots can be avoided by using shaped illumination of the hologram. The shaped illumination can be realised by designing a feed system that modifies both amplitude and phase pattern of the primary feed, i.e., a corrugated feed horn.

A dual reflector feed system (DRFS) can be used as a feed system for a hologram-based CATR [13], [12]. Previously, a 310 GHz DRFS for hologram-based CATR has been demonstrated at 310 GHz [14]. A numerical ray-tracing based synthesis method [15], [13] was developed specifically for this purpose. Later, a 650 GHz DRFS [16], [17] was designed as part of a large antenna measurement project [12]. Same ray-tracing principles can be used to design a feed system based on shaped lenses.

In this thesis, the design principle of the feed systems for hologram-based compact ranges is presented. The synthesis method and design procedure, used to design the dual reflector feed systems, is generalised also for shaped lens feed systems. The 650 GHz DRFS and a design example of a shaped lens feed system are presented in detail.

2 Antenna measurement techniques

Antenna measurement techniques can be divided into three basic types: far-field measurements, near-field scanning techniques and compact antenna test ranges (CATR). In general, antenna measurement aims at determining the antenna radiation pattern. Also, for example, antenna impedance, radiation efficiency, etc. can be measured.

Antenna pattern includes relative amplitude, relative phase, polarisation, and the power gain [18]. Often antenna pattern is expressed as amplitude and phase patterns for main and cross-polarisations.

Far-field and near-field measurements are briefly explained in Sections 2.1 and 2.2, respectively. In Section 2.3 compact antenna test ranges are explained.

Antenna measurement results of this thesis are in Chapter 8. Many different antenna measurement techniques are used. In Section 8.1, the 650 GHz feed horns are measured in the far-field of the AUT. In Section 8.2, the 650 GHz DRFS is measured by near-field scanning. In Section 8.3, the 650 GHz DRFS is used in a compact antenna test range and the quiet-zone quality is tested with near-field scanning.

2.1 Far-field measurement

Far-field measurement setup is illustrated in Figure 2.1. The antenna under test is placed in the far-field of the range feed. The field illuminating the AUT is (nearly) a plane wave, i.e., planar wave front and constant amplitude in the whole volume where the AUT is placed. The radiation pattern of the AUT is recorded as function of the rotation angle θ.

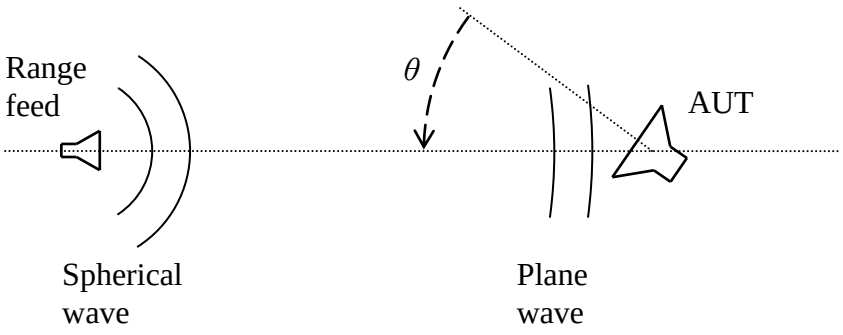

Figure 2.1: Far-field measurement.

In far-field region the radiation pattern is a function of angle and does not depend on the distance from a specified point in the antenna region [19]. Field depends on the distance r as

$$\overline{E}(r) \sim e^{-jkr} / r \quad , \tag{2.1}$$

where $k = 2\pi/\lambda$ is the wave number. Field amplitude decreases as $1/r$. The phase changes in direction of propagation in same way as a plane-wave field. In far-field the

ratio of electric and magnetic field is a constant called a wave impedance η. In vacuum (and in air) $\eta_0 \approx 377\ \Omega$. The electric and magnetic fields are orthogonal to each other and to the direction of propagation.

Typically far-field criterion is defined as:

$$r \geq \frac{2D^2}{\lambda}, \tag{2.2}$$

where D is the diameter of the antenna and λ is the wavelength. The far-field criterion is defined as the distance from the antenna where the distance to the edge of the antenna is $\lambda/16$ longer than the distance to the centre of the antenna, i.e., phase deviation from a plane wave is 22.5°. For example, if the first side lobe is at –40 dB then side lobe level measurement error is 1 dB at a distance of $6D^2/\lambda$ [20].

At sub-millimetre wavelengths for a large antenna the far-field criterion can be tens of kilometres and atmospheric attenuation is very high; therefore far-field measurements can be impossible. For example, the far-field criterion (2.2) gives about 10 km for a 1.5 m diameter antenna at 650 GHz. Far-field measurements are possible for small antennas, as for example the far-field criterion is only about 4 cm for a 3 mm diameter antenna at 650 GHz.

The 650 GHz feed horns, in Section 8.1, are measured in the far-field of the AUT. Instead of rotating the AUT, the radiation pattern is measured with a planar scanner. The measurement distance of about 1 m is clearly in the far-field region. A so-called three antenna method is used to measure the beam widths of the three feed horns.

2.2 Near-field measurement

In near-field antenna measurements the antenna radiation is measured in the near field and the far-field radiation is calculated from the near-field data for example using the Fourier-transform. The near field is sampled with a probe antenna on a surface in the radiating near-field of the AUT. The sampling surface can be planar, spherical or cylindrical.

The sampling interval has to be smaller than $\lambda/2$ for the full angular coverage [21] and position accuracy better than $\lambda/100$. The measurements of large high frequency antennas are very challenging because of the required high dynamic range, probe position accuracy and very high number of sampling points.

Example of near-field measurements at frequencies up to 650 GHz is in [22]. A very high precision granite scanner mechanism was used to achieve the required planar accuracy.

Error sources in near-field measurement are analysed for example in [23], [24]. Error analysis of a near-field measurement system is in general a combination of closed-form equations, simulations, and measurement tests.

In planar near-field measurements the planarity error of the scanner can be very significant error source. Planarity errors can affect the measured phase significantly at high frequencies as the planarity affects directly the measurement distance, i.e., the

electrical path length. The phase error $\Delta\Psi(x,y)$ caused by planarity error $z(x,y)$ can be expressed simply as:

$$\Delta\Psi(x,y) = -\frac{z(x,y)}{\lambda} \cdot 360° . \tag{2.3}$$

Equation (2.3) is valid only for incident plane wave but can be used also for incident spherical wave if the resulting path length error is small (incident angle is small). Planarity errors can be corrected from the measurement results if the planarity of the scanner is known.

The 650 GHz DRFS is measured by near-field scanning in Section 8.2. The far-field pattern was not calculated as the DRFS is used in the near-field region (far-field criterion gives a few hundred meters and the distance to the hologram is 12.72 m). Averaging of measurements, drift compensation with tie-scans, probe correction, and a planarity error correction techniques were used to reduce the measurement errors.

2.3 Compact antenna test range

Compact antenna test range (CATR) is based on using a collimating element that creates the needed far-field conditions for the antenna measurement. The area where the far-field conditions are created is called the quiet zone (QZ). The antenna under test (AUT) is rotated as in the far-field measurements and the radiation pattern is recorded. The collimating element can be a reflector, a set of reflectors, a lens, or a hologram. Compact ranges can also be used in radar cross-section (RCS) measurements.

The development of CATRs started in 1950's with lenses [25], [26]. The reflector based CATRs have been developed since the 1960's [27], [26]. A hologram-based CATR was first proposed in 1992 [7].

Main advantage of a CATR is that the measurements can be done inside in controlled environment in relatively small space. Also, there is no need to calculate near to far-field transformation as in the near-field measurements. Usually ripple of 1 dB peak-to-peak and 10° peak-to-peak is allowed at maximum in the quiet-zone field amplitude and phase, respectively.

2.3.1 Reflector-based compact antenna test range

The most common CATR is based on a reflector or a set of reflectors. Reflector based compact antenna test ranges are commonly used at frequencies up to 200 GHz [28], [29]. A reflector-based CATR has been used in antenna test up to 500 GHz [30]. The highest usable frequency of a reflector-based CATR is typically limited by the surface accuracy of the reflectors. The surface accuracy requirement is approximately λ/100 [18]. The lowest usable frequency is limited by the diffracted fields from the edges of the reflectors as the diffracted fields are strongest at low frequencies [26].

The main reflector has to be larger than the quiet-zone. The quiet-zone diameter is typically about 1/3 of the main reflector diameter for a single reflector CATR and 2/3 for dual reflector CATR. Reflector geometries used are: a single offset reflector [27], a dual

cylindrical reflector [32], a dual offset reflector [29], [33], [34] and a triple offset reflector [35], [36]. Examples of CATR geometries are illustrated in Figure 2.2.

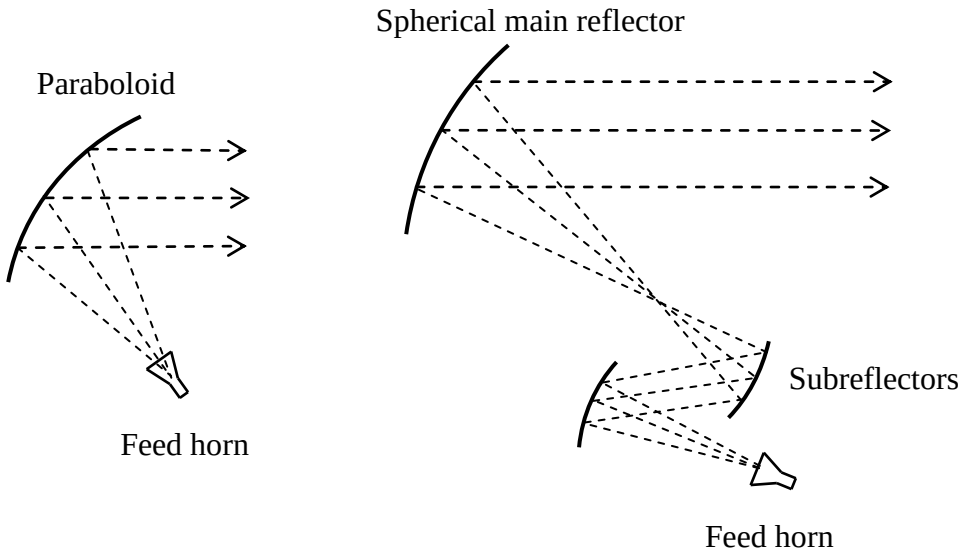

Figure 2.2: Examples of a single offset reflector and a trireflector CATR.

Offset paraboloidal reflectors produce typically about –30 dB cross-polarisation level to the QZ [26]. The cross-polarisation performance can be improved by using two reflectors and by choosing the parameters of the CATR so that the cross-polarisation is minimised [37], [38]. Examples of cross-polarisation compensated CATRs are in [29], [33].

Diffraction from the reflector edges causes ripples to the QZ. The edge diffraction can be reduced with reflector edge treatment, e.g. serrations [39], rolled edge [39], or by reducing the edge illumination by shaping the reflectors [34], [35].

2.3.2 Lens-based compact antenna test range

A lens can be used as a collimating element in a CATR. Geometry of a classical lens-based CATR is presented in Figure 2.3 [40]. The lens is designed to correct the phase pattern of the range feed to a plane wave. In [41], plastic foam lens is used with added loss into the lens so that also the amplitude is nearly uniform behind the lens.

Advantages of the lens-based CATR are [26]: high utilisation factor (ratio of diameter of the collimating element to the diameter of the QZ), low cross-polarisation level, and that there is no direct radiation from the feed to the QZ. Disadvantages are [26]: amplitude taper (due to feed horn amplitude pattern and transmission coefficient at larger incident angles), relatively long length, and the need to achieve homogeneity in the dielectric.

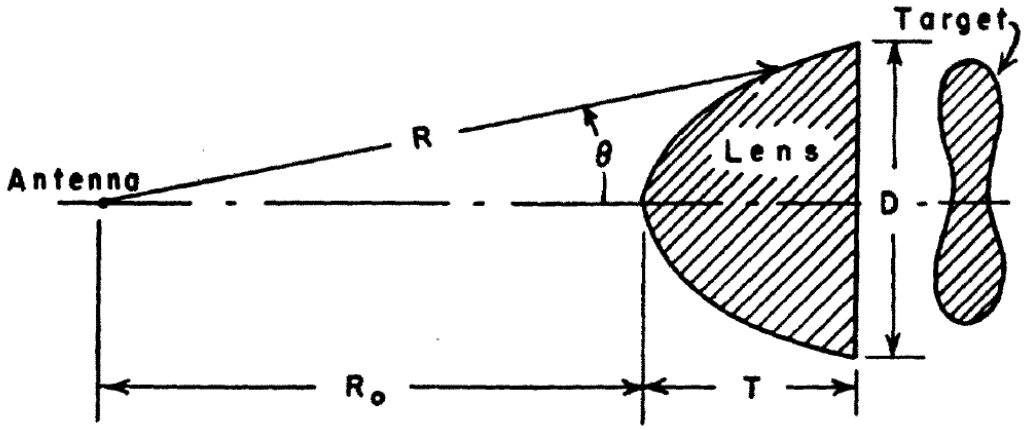

Figure 2.3: Geometry of a classical lens-based CATR designed for radar cross-section (RCS) measurements [40].

Lens-type compact antenna test range at mm-waves is studied in [42], in which the lens shape is calculated with a ray-tracing method presented in [43].

Compact antenna range based on a lens is mainly potential at very high frequencies as the surface accuracy requirement for a reflector becomes too stringent. Because a lens is a transmission-type element and because the wave length is shorter inside the lens, the surface accuracy requirement is weighted by $\left(\sqrt{\varepsilon_r}-1\right)/\sqrt{2}$ compared to a reflector [42]. ε_r is the relative permittivity of the lens material. The difference of the effect of a surface error is illustrated in Figure 2.4.

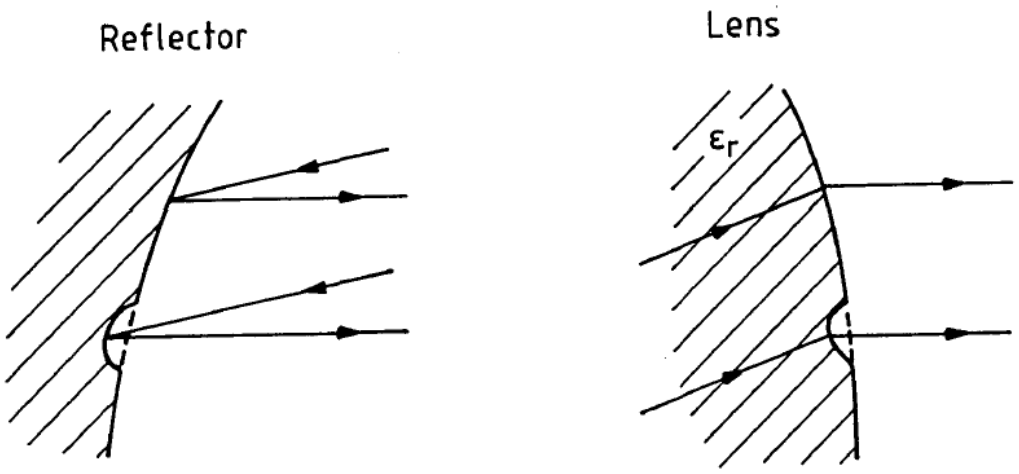

Figure 2.4: The effect of a surface error in case of a reflector and in case of a lens [42].

2.3.3 Hologram-based compact antenna test range

A computer-generated radio-wave hologram can be used as a collimating element in a compact antenna test range [8]. The hologram is an interference pattern of the wave-front illuminating the hologram and the desired goal field [44]. In a CATR, the goal field is a plane wave in the quiet zone.

Antenna tests that have been done in hologram-based CATRs are listed in Section 2.3.3.1. All holograms used in antenna tests have been transmission-type amplitude holograms. Also, phase holograms [45], [46], and reflection-type holograms [47] have been studied.

A schematic layout of a hologram-based CATR using a transmission-type amplitude hologram is shown in Figure 2.5. Typically, an offset angle of 33° is used to avoid direct radiation through the hologram from affecting the QZ. The hologram pattern is etched on a metal layer on a thin Mylar film. The pattern consists of vertical, slightly curved slots in the copper-laminate. Because of the planar structure and because the hologram is a transmission type element, the manufacturing accuracy requirement is not as high as for reflectors. The accuracy requirement is only 1/10 of that required for a reflector. A hologram is light weight and inexpensive device compared to other types of collimating elements in CATRs.

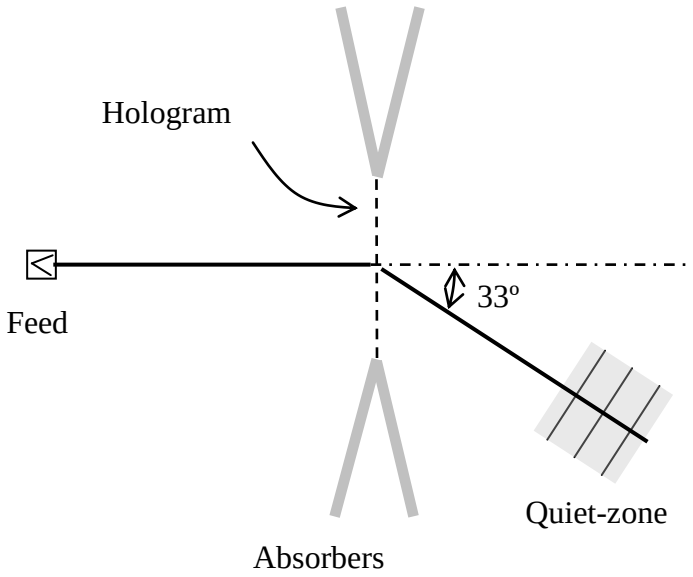

Figure 2.5: Schematic layout of a hologram-based CATR.

The hologram is designed with electromagnetic simulations [44]. An example of a hologram pattern is presented in Figure 2.6. The structure of the hologram is analysed with finite-difference time-domain method (FDTD) and the quiet-zone field is calculated with physical optics (PO) from the aperture field. Because the whole hologram is too large to simulate in one simulation, only one cut of the nonuniform metal grating is analysed [44]. The cross-polarisation is not analysed in these two-dimensional simulations, therefore cross-polarisation is calculated with a method presented in [48].

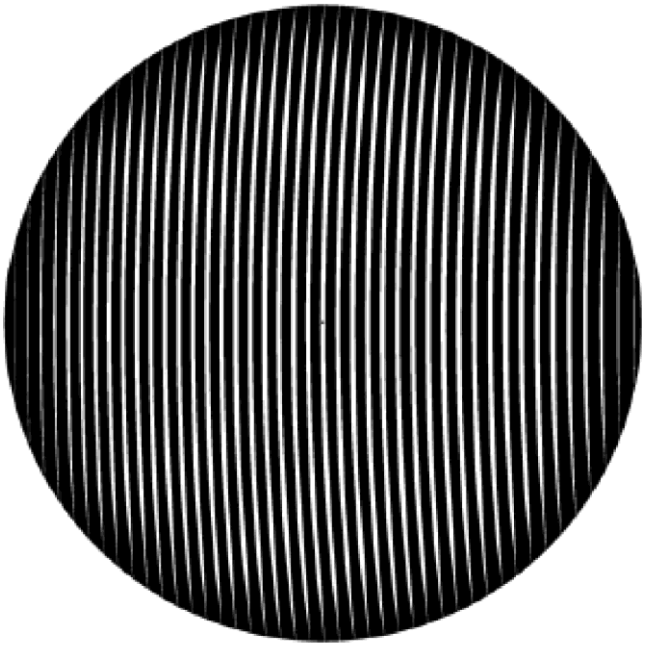

Figure 2.6: Example of a transmission-type amplitude hologram pattern. Metal is in black and slots in white.

A transmission-type hologram can be an amplitude hologram or a phase hologram. In an amplitude-type hologram the radiation is partially blocked by metal strips and partially transmitted through slots between the metal strips. A phase hologram is based on locally varying the effective electrical path length, for example by varying the effective thickness pattern. A phase hologram can be realized by milling grooves on a dielectric substrate [45]. With a phase hologram it is possible to have higher conversion efficiency, i.e., lower losses.

A phase hologram has been used in a hologram-based compact radar cross section (RCS) range for scale model measurements at 310 GHz [45]. The layout of the RCS range is similar to the layout in Figure 2.5. The scale model is placed in the QZ and the transmitter and receiver are separated with a dielectric slab working as a directional coupler.

A reflection-type phase hologram CATR has also been designed [47]. In a reflection-type phase hologram grooves are milled into a metal slab. The main advantages compared to transmission-type holograms are lower losses and that the harmful reflections inside the hologram are avoided.

2.3.3.1 History of antenna tests in a hologram-based CATR

Hologram-based CATRs have been used in antenna tests at frequencies from 39 GHz up to 650 GHz [9]–[12].

In [9], a planar antenna made of array of waveguide fed horns [49] is measured in a hologram CATR at 39 GHz. The QZ is measured to be 70 cm × 45 cm. The same antenna was measured also with near-field scanning and with conventional far-field technique and

the measurement results are found to agree well down to side-lobe levels 30–35 dB below peak [9].

Measurement of the Odin telescope [50] at 119 GHz is presented in [10]. The Odin telescope has a 1.1 m offset reflector antenna shown in Figure 2.7. The 2.4 m × 2.0 m hologram produces about 1.65 m × 1.55 m QZ. The measured main lobe is symmetric and the beam-width is as designed [10].

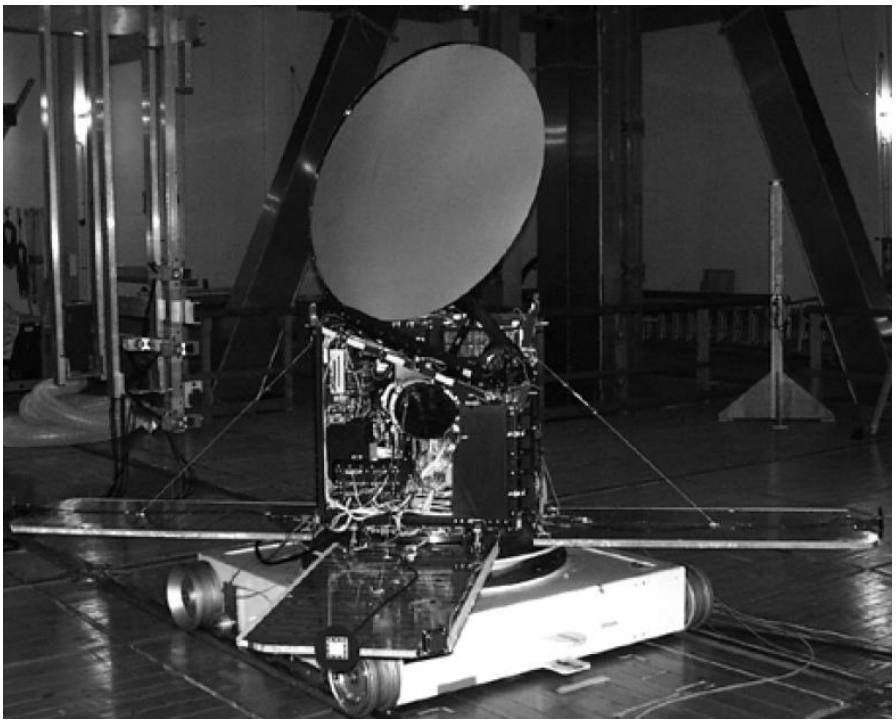

Figure 2.7: The 1.1 m offset reflector antenna on the Odin satellite [10].

A 1.5 metre diameter antenna was measured at 322 GHz in 2003. The design and construction of the CATR and the QZ tests are presented in [51]. The antenna test results are presented in [11]. The antenna under test was ADMIRALS representative test object (RTO) [30]. A photograph of the RTO is in Figure 2.8. The 3-m-diameter hologram is soldered together from three separate pieces. The measured antenna radiation pattern corresponds reasonably well to the simulated pattern. The effect of the non-ideal quiet-zone field on the measured radiation pattern was investigated by computing the radiation of the simulated antenna including the effect of the measured quiet-zone field in [11].

Figure 2.8: ADMIRALS RTO on the antenna positioner [11].

In 2006, the ADMIRALS RTO was tested at 650 GHz in a hologram-based CATR [12]. This is the highest frequency at which a large antenna has ever been measured in any CATR. The hologram diameter is 3.16 m. A DRFS is used to provide a modified illumination for the hologram for a first time in an antenna measurement. The range feed, i.e., the DRFS, is placed 12.72 m from the hologram and the AUT is placed about 9 m from the hologram. Layout of the CATR is shown in Figure 2.9.

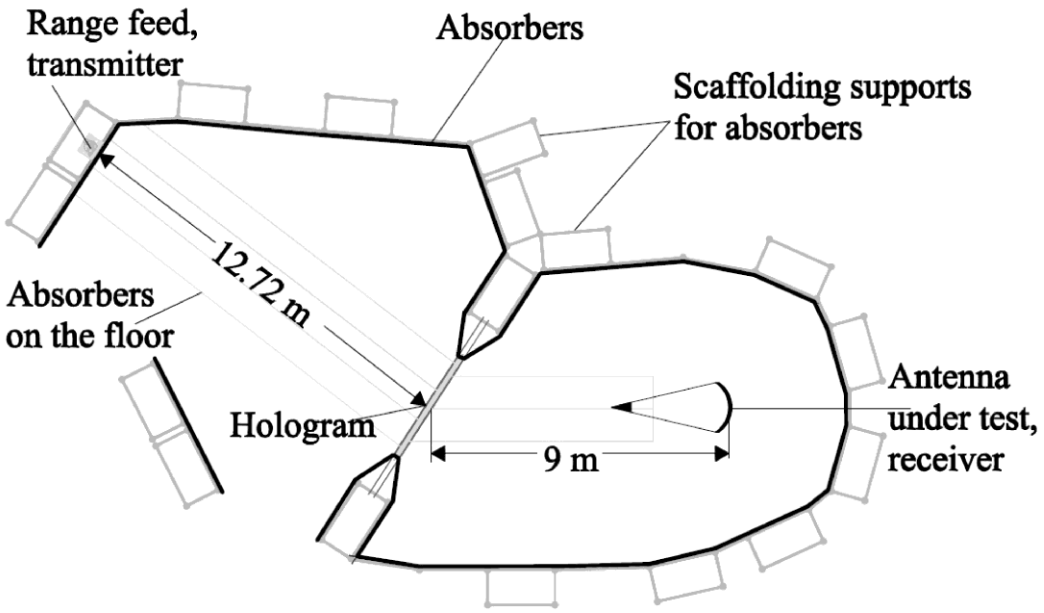

Figure 2.9: Layout of the CATR [12].

2.3.3.2 Feed system for a hologram-based CATR

Traditionally a corrugated feed horn has been used to illuminate the hologram [9], [10], [11]. This leads to high edge illumination of the hologram and the slots in the hologram pattern need to be narrowed towards the edges to reduce the ripple caused by edge diffractions.

Traditionally the holograms have been limited to be used only at the linear vertical polarisation. That is because transmission of a horizontal polarisation through the vertical slots is nearly independent of the slot width [52]; and therefore edge diffraction at the horizontal polarisation is not avoided with the narrowing of the slots.

The narrow slots are also difficult to manufacture accurately. It may happen that the narrow slots are not completely etched and that reduces the hologram size and increase edge diffraction [44].

The narrow slots can be avoided if the hologram is illuminated with a modified illumination. For example, a dual reflector feed system (DRFS) can be used to modify the hologram illumination [14], [17]. The hologram illumination can be designed to have a flat amplitude to the centre of the hologram and amplitude tapering to the edge of the hologram. Hologram designed for such modified illumination does not need to change the amplitude distribution and therefore the narrow slots can be avoided. The hologram is only used to transform the spherical phase front to a planar one [44]. Avoiding the narrow slots has several advantages.

An example of slot widths of holograms designed for a modified illumination and for the traditional Gaussian illumination is shown in Figure 2.10.

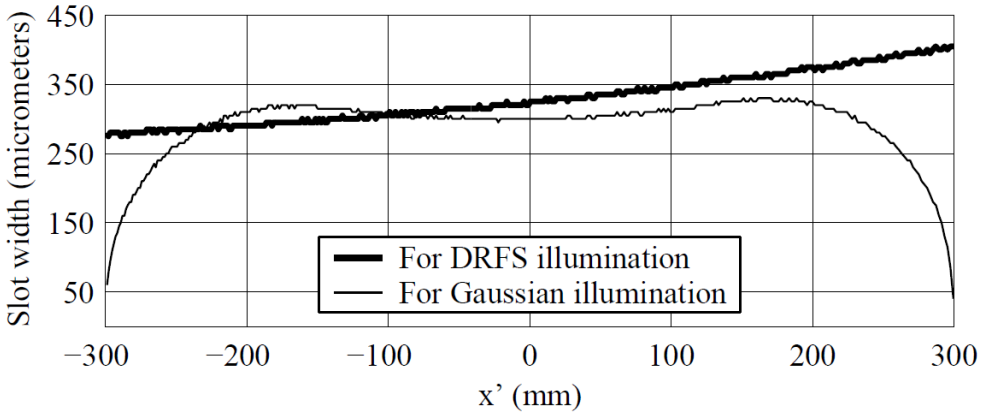

Figure 2.10: Example of slot widths of a 310 GHz holograms along the centreline designed for modified illumination (from DRFS) or for a traditional Gaussian illumination [53].

The advantages of using the modified illumination are listed in the following paragraphs.

1) The slots in the hologram pattern can be wider and the slot widths can be almost uniform which simplifies the manufacturing of the hologram.

2) The hologram can be optimised for both vertical and horizontal polarisations [53].

3) The hologram can be designed to operate almost identically at both linear polarisations [52]. Hologram that operates identically at both linear polarisations could be used to test antennas at circular polarisation.

4) Cross-polarization in the QZ with a hologram designed for a corrugated feed horn is from –15 dB to –20 dB [44], [48]. By using the modified illumination the cross-polarisation performance of the hologram is improved by about 10 dB [52], without taking into account the cross-polarisation in the illuminating field. If the feed system provides sufficiently low cross-polarisation level, the cross-polarisation in the QZ can be reduced by using a modified illumination from a feed system.

5) The quiet-zone size is in practice determined by the –1 dB beam width of the hologram illumination [13], [44]. The QZ diameter is approximately cos(33°) times the –1 dB beam width in the horizontal direction because of the offset angle. By designing a feed system with wider beam width it is possible to increase the QZ to hologram size ratio.

Amplitude and phase ripples in the illumination increase directly the overall ripples in the quiet-zone field. QZ field ripples are a combination of ripples in the illumination and ripples caused by the hologram. The ripples in the illuminating field should be as small as possible.

Two dual reflector feed systems have been made; one at 310 GHz [13], [14] and one at 650 GHz [16], [17]. The numerical synthesis method that is used to design feed systems for hologram-based CATRs is presented in detail in Chapter 5. The designed DRFSs are presented in Chapter 6. The same synthesis method is used for a feed system based on shaped lenses in Chapter 7.

3 Calculation of field radiated by an antenna

Calculation of field radiated by an antenna is always based on solving the Maxwell's equations [54]:

$$\nabla \times \overline{E} = -j\omega\mu \overline{H} - \overline{J}_m \tag{3.1}$$

$$\nabla \times \overline{H} = j\omega\varepsilon \overline{E} + \overline{J}, \tag{3.2}$$

where $\overline{E}$ is the electric field, $\overline{H}$ is the magnetic field, $\overline{J}$ and $\overline{J}_m$ are the electric and magnetic current densities, ω is the angular frequency, μ is permeability, and ε is permittivity. Time dependence of $e^{j\omega t}$ is assumed. Sometimes the current densities are known with good accuracy. For example for a dipole the current is known and the radiated field can be calculated with Maxwell's equations.

Often the antenna structure is too complex to directly determine the current densities. The antenna structure can be replaced with equivalent current sources without changing the radiated field. When the equivalent current sources are determined the radiated field can be calculated with Maxwell's equations. There are many methods that can be used to determine these equivalent current sources. Calculation of equivalent current sources from a known aperture field, and calculation of radiated field from these currents, is explained in Section 3.1.

If a field illuminating a known metal object (antenna) is known, the surface currents can be calculated using physical optics (PO). PO is described in Section 3.2. Physical optics does not take into account diffraction from edges of the antenna structure. Physical theory of diffraction (PTD) can be used to include the diffracted fields to PO, as explained in Section 3.3. PO (with PTD) is commonly used to analyse electrically large reflector antennas. In this thesis, PO and PTD are used to simulate the radiated field of a dual reflector feed systems (DRFS), as explained in Section 5.4.1.

Geometrical optics (GO) is a high frequency approximation of the Maxwell's equations. GO is commonly used to analyse lens and reflector antennas. The basic equations of geometrical optics are introduced in Section 3.4. The numerical synthesis method used to design feed systems for hologram-based compact ranges is a GO-based ray-tracing synthesis method. The numerical synthesis method is explained in detail in Chapter 5. In this thesis, field radiated by a shaped lens antenna is analysed by calculating the aperture field with ray-tracing and the radiated field is calculated from the equivalent current sources. This ray-tracing method is explained in Section 5.4.2.

The antenna radiation analysis methods used in designing the feed systems are described in Sections 3.1–3.4.

3.1 Radiation of an aperture

Radiation of an aperture antenna can be calculated with Huygens' principle [54]. Examples of aperture antennas are open-ended waveguide, horn antenna, and reflector or lens antennas. According to Huygens' principle sources inside a closed surface *S* can be

replaced with surface sources $\overline{J}_s$ and $\overline{J}_{ms}$ on the surface. These are called equivalent sources (or Huygens' sources) [19]. The equivalent surface currents depend on the electric and magnetic fields on the surface as: [54], [55]

$$\overline{J}_s = \overline{n} \times \overline{H} \tag{3.3}$$

$$\overline{J}_{ms} = -\overline{n} \times \overline{E}\,, \tag{3.4}$$

where $\overline{n}$ is the surface normal pointing out of the surface. The original antenna problem can be replaced with these surface currents and air inside the closed surface *S*. Then the field radiated by the antenna can be calculated with Maxwell's equations with these surface currents as sources.

The problem can be simplified if the volume inside *S* is filled with either perfect electric (PEC) or perfect magnetic (PMC) conductor [54]. If the volume is filled with magnetic conductor, with $\sigma_m = \infty$ ($\mu = \infty$), $\overline{J}_{ms}$ can be eliminated, and if the volume is filled with electric conductor, with $\sigma = \infty$ ($\varepsilon = \infty$), $\overline{J}_s$ can be eliminated. Therefore, it is necessary to evaluate only either magnetic or electric field on the surface *S* and the sources are calculated using either (3.3) or (3.4).

It is often convenient to define the surface *S* to be the aperture plane of the antenna. The aperture plane divides the antenna problem into two half-spaces, one with the antenna structure and sources and one source-free half-space where the field is calculated. If the aperture plane is infinite it is a closed surface and Huygens' principle applies.

For simplicity from now on we assume that the electric field on the aperture $\overline{E}_a$ is known, and the antenna problem is replaced with perfect electric conductor and equivalent magnetic surface currents, as shown in Figure 3.1.

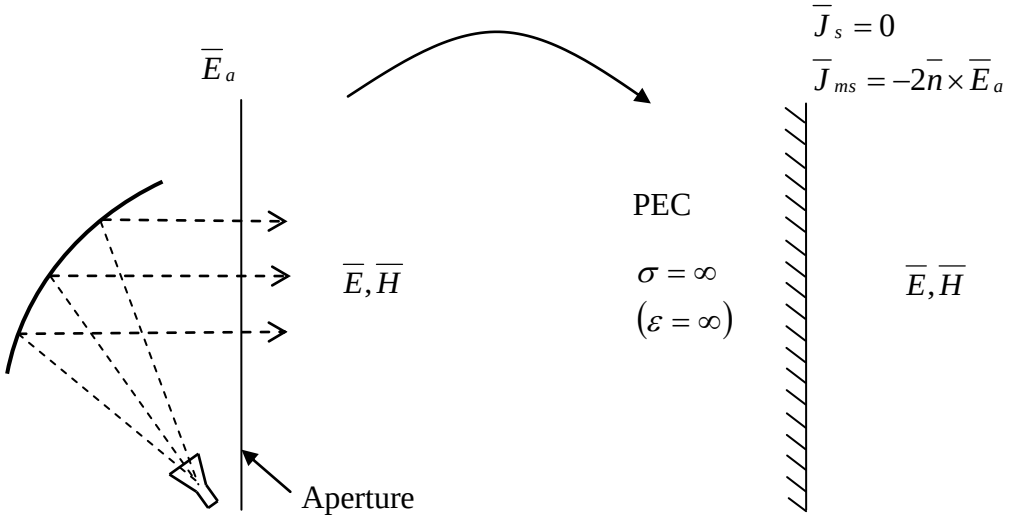

Figure 3.1: The original antenna problem is replaced with perfect conductor and equivalent magnetic surface currents.

The method of images gives the equivalent surface currents on the surface *S*:

$$\bar{J}_s = 0 \tag{3.5}$$

$$\bar{J}_{ms} = -2\bar{n} \times \bar{E}_a . \tag{3.6}$$

The electric field outside the aperture surface, caused by the surface currents $\bar{J}_{ms}$, can be expressed with the scalar Green's function $G(\bar{r} - \bar{r}')$ as an integral [54]:

$$\bar{E}(\bar{r}) = -\oint_S \left[\nabla G(\bar{r} - \bar{r}')\right] \times \bar{J}_{ms}(\bar{r}') dS' , \tag{3.7}$$

where $G(\bar{r} - \bar{r}')$ is the scalar Green's function:

$$G(\bar{r} - \bar{r}') = \frac{e^{-jk|\bar{r} - \bar{r}'|}}{4\pi|\bar{r} - \bar{r}'|} , \tag{3.8}$$

and $\bar{r} = x\bar{u}_x + y\bar{u}_y + z\bar{u}_z$ is a point where the field is calculated, $\bar{r}' = x'\bar{u}_x + y'\bar{u}_y + z'\bar{u}_z$ is a point on the aperture, and $k = \omega\sqrt{\varepsilon\mu}$ is the wave number.

Lets examine in detail a situation where the aperture plane is the *xy*-plane and its unit surface normal $\bar{n} = \bar{u}_z$, and aperture electric field is expressed as a combination linear polarisations.

For a linearly polarised aperture field $\bar{E}_a(\bar{r}') = E_a(\bar{r}')\bar{u}_y$:

$$\begin{aligned} \bar{E}(\bar{r}) &= -\oint_S \left[\nabla \frac{e^{-jk|\bar{r} - \bar{r}'|}}{4\pi|\bar{r} - \bar{r}'|} \right] \times \left(-2\bar{u}_z \times E_a(\bar{r}')\bar{u}_y \right) dS' \\ &= \oint_S \left[\frac{E_a(\bar{r}')e^{-jkR}}{2\pi} \left(\frac{jk}{R^2} + \frac{1}{R^3} \right) \left((z - z')\bar{u}_y - (y - y')\bar{u}_z \right) \right] dS' , \end{aligned} \tag{3.9}$$

where $R = |\bar{r} - \bar{r}'| = \sqrt{(x - x')^2 + (y - y')^2 + (z - z')^2}$.

Similarly it is possible to derive equations for the radiated electric field $\bar{E}_a = E_a\bar{u}_x$. It is easy to see that for $\bar{E}_a = E_a\bar{u}_z$ we get $\bar{E}(\bar{r}) = 0$.

The magnetic field outside the aperture surface caused by the surface currents $\bar{J}_{ms}$ is [54]:

$$\bar{H}(\bar{r}) = -j\omega\varepsilon \oint_S \bar{\bar{G}}(\bar{r} - \bar{r}') \cdot \bar{J}_{ms}(\bar{r}') dS' , \tag{3.10}$$

where $\bar{\bar{G}}(\bar{r} - \bar{r}')$ is the Green's dyad:

$$\overline{\overline{G}}\left(\bar{r}-\bar{r}'\right)=\left(\overline{\overline{I}}+\frac{1}{k^2}\nabla\nabla\right)G\left(\bar{r}-\bar{r}'\right). \tag{3.11}$$

Alternatively, if the volume inside S is filled with magnetic conductor the surface currents $\bar{J}_s$ are calculated by the method of images and $\bar{J}_{ms}=0$. The electric and magnetic fields caused by the surface currents $\bar{J}_s$ are: [54]

$$\bar{E}\left(\bar{r}\right)=-j\omega\mu\oint_S \overline{\overline{G}}\left(\bar{r}-\bar{r}'\right)\cdot\bar{J}_s\left(\bar{r}'\right)dS' \tag{3.12}$$

$$\bar{H}\left(\bar{r}\right)=\oint_S\left[\nabla G\left(\bar{r}-\bar{r}'\right)\right]\times\bar{J}_s\left(\bar{r}'\right)dS' \quad . \tag{3.13}$$

In far-field $\left|\bar{r}\right|>>\left|\bar{r}'\right|$ and the distance from field point to integration point $\left|\bar{r}-\bar{r}'\right|$ can be approximated: (with first two terms of Taylor series)

$$\left|\bar{r}-\bar{r}'\right|\approx r-\bar{u}_r\cdot\bar{r}'. \tag{3.14}$$

The far-field approximation of the Green's function is: [54]

$$G\approx\frac{e^{-jkr}}{4\pi r}e^{jk\bar{u}_r\cdot\bar{r}'}, \tag{3.15}$$

and the approximation of the Green's dyad is: [54]

$$\overline{\overline{G}}\approx\left(\overline{\overline{I}}-\bar{u}_r\bar{u}_r\right)\frac{e^{-jkr}}{4\pi r}, \tag{3.16}$$

where $\bar{r}=r\bar{u}_r$, r is the distance from the antenna, and $\bar{u}_r$ is the direction from the antenna to the field point. The far-field is calculated from (3.7), (3.10), (3.12), or (3.13), using the far-field approximation of the Green's function (3.13) or Green's dyad (3.16). In far-field the relation of electric and magnetic fields is:

$$\bar{E}=\eta\bar{H}\times\bar{u}_r \tag{3.17}$$

$$\bar{H}=\frac{1}{\eta}\bar{u}_r\times\bar{E}. \tag{3.18}$$

3.2 Physical optics

Field reflected by a reflector can be calculated using physical optics (PO). Physical optics is an approximation of surface currents. The physical optics approximation is valid for scatterers made of perfect electric conductor that are large in terms of wavelengths [56].

In PO, the surface currents on a reflector surface are calculated from the incident field. Reflected fields are calculated from these surface currents. Using Huygens' principle, as

explained in Section 3.1, the antenna structure can be replaced with perfect electric or magnetic conductor and equivalent surface currents.

The surface is assumed locally flat and infinite. Surface current densities on a perfect electric conductor are [54], [56]

$$\overline{J}_s = 2\overline{n} \times \overline{H}_i \tag{3.19}$$

$$\overline{J}_{ms} = 0, \tag{3.20}$$

where $\overline{n}$ is the surface normal pointing out of the surface and $\overline{H}_i$ is the incident magnetic field. In the shadow region, i.e., surface area that is not directly illuminated by the incident field, the surface currents are assumed to be zero. The reflected fields are calculated with (3.12) and (3.13).

The surface currents are calculated in discrete points on the antenna surface [56]. At these points the surface is approximated with the tangential plane and surface currents are calculated from (3.19). In order to get sufficient accuracy with this approximation the dimensions and radius of curvature have to be at least a few wavelengths. The number of current elements has to be large enough for the PO to give accurate prediction of the reflected field. The required number of the current elements depends on the size and the shape of the object compared to the wavelength and the desired field accuracy.

3.3 Physical theory of diffraction

Physical theory of diffraction (PTD) can be used to include edge diffractions to PO [56]. In PTD edge currents are calculated from the shape of the edge and the incident field. The field calculated from edge current is added to PO fields

$$\overline{E} = \overline{E}_{PO} + \overline{E}_{PTD}. \tag{3.21}$$

In the edge current calculations the edge is approximated locally to be a perfectly conducting half plane. The radius of curvature of the edge and the number of current elements has to be sufficiently large for this approximation to be valid. The PTD field is calculated by integrating over the illuminated part of the edge from PTD equivalent edge currents. These currents are calculated from fringe wave currents along incremental steps on the edge [56]. A closed form expressions for PTD equivalent edge currents are derived for truncated incremental wedge strips in [57].

3.4 Geometrical optics

Geometrical or ray optics is widely used in design of electrically large lens and reflector antennas. The theory is explained in detail for example in [58], [55] (in English) or in [54] (in Finnish).

Geometrical optics (GO) is a high frequency approximation of the Maxwell equations. The high frequency approximation is accurate if all distances, radii of curvature, etc. are large compared to the wavelength. The electric and magnetic fields can be expanded as power series of inverse powers of the angular frequency ω [55]

$$\overline{E}\left(\omega,\bar{r}\right)=e^{-jk_0L\left(\bar{r}\right)}\sum_{i=0}^{\infty}\frac{\overline{E}_i\left(\bar{r}\right)}{\left(j\omega\right)^i} \tag{3.22}$$

$$\overline{H}\left(\omega,\bar{r}\right)=e^{-jk_0L\left(\bar{r}\right)}\sum_{i=0}^{\infty}\frac{\overline{H}_i\left(\bar{r}\right)}{\left(j\omega\right)^i}, \tag{3.23}$$

where $L\left(\bar{r}\right)$ is the so called eikonal function and $k_0=\omega\sqrt{\mu_0\varepsilon_0}$. At high frequencies the 0^{th} order dominates. The 0^{th} order equations describe the geometrical optics field:

$$\overline{E}_0\times\nabla L=-\frac{\omega\mu}{k_0}\overline{H}_0 \tag{3.24}$$

$$\overline{H}_0\times\nabla L=\frac{\omega\varepsilon}{k_0}\overline{E}_0 \tag{3.25}$$

$$\overline{E}_0\cdot\nabla L=0 \tag{3.26}$$

$$\overline{H}_0\cdot\nabla L=0\,. \tag{3.27}$$

The geometrical optics field vectors $\overline{E}_0\left(\bar{r}\right)$, $\overline{H}_0\left(\bar{r}\right)$ and $\bar{k}\left(\bar{r}\right)=k_0\nabla L\left(\bar{r}\right)$ are perpendicular to each other. The surface where the phase is constant is given by the surface where $\mathrm{Re}\{L\}$ is constant. When L is real power propagates in the direction of $\bar{k}$, i.e., perpendicular to the constant phase front. The eikonal function determines the ray directions and the wave fronts. The eikonal function is determined from the so the called eikonal equation:

$$\nabla L\left(\bar{r}\right)\times\nabla L\left(\bar{r}\right)=\mu_r\left(\bar{r}\right)\varepsilon_r\left(\bar{r}\right)=n^2\left(\bar{r}\right), \tag{3.28}$$

where $n\left(\bar{r}\right)=\sqrt{\mu_r\left(\bar{r}\right)\varepsilon_r\left(\bar{r}\right)}$ is the index of refraction of the medium.

The ray equation represents the direction of propagation. For a ray $\bar{r}(s)$ the ray equation derived from the eikonal equation is [54]:

$$\bar{t}\cdot\nabla\left(n\bar{t}\right)=\frac{d}{ds}\left(n\left(\bar{r}\right)\frac{d\bar{r}}{ds}\right)=\nabla n\left(\bar{r}\right), \tag{3.29}$$

where $\bar{t}$ is the tangential unit vector of the ray and *s* is the distance along the ray. The ray equation is a second order non-linear differential equation. It can be solved analytically for some cases, but usually it is solved numerically.

Field amplitude is calculated from the transport equation [54]:

$$\frac{d\overline{E}_0}{ds} = -\frac{1}{n}\bar{t}(\nabla n)\cdot\overline{E}_0 - \frac{\mu_r}{2n}\nabla\cdot\left(\bar{t}\frac{n}{\mu_r}\right)\overline{E}_0 . \tag{3.30}$$

The transport equation is a differential equation for an unknown vector $\overline{E}_0$. If $\overline{E}_0$ is known at some point it can be solved at all points along the ray. It can be proved from (3.30) that $\left|\overline{E}_0\right|^2$ integrated over the cross-section of a ray tube is constant. Power propagates inside the ray tube and the power density depends on the cross-sectional area of the ray tube. Also polarisation and phase along the ray can be calculated from (3.30).

In geometrical optics the concept of rays is useful in understanding and illustrating the propagation of geometrical optics fields. A ray is a line in space that represents the direction of propagation. The ray path and field along the ray can be calculated. The volume between rays is called a ray tube. Ray tubes are useful in understanding and calculating propagation of power. In general, rays and ray tubes are used as conceptual aid in deriving equations or functions that describe analytical solution to the given problem. In general in geometrical optics, the properties of single rays are not calculated.

In ray-tracing fields are calculated by determining the path of a finite number of rays. First rays are calculated from a known field and then these rays are traced one by one (their path is calculated) through material, reflections, refractions, etc., and finally the desired field is calculated from the resulting ray distributions, ray lengths, etc. Complex systems can be analysed as it is not necessary to derive an analytical solution.

4 Reflector and lens antennas

Large reflector and lens antennas are aperture antennas used to redirect the radiation of a primary feed. Reflector and lens antennas are typically designed and analysed using GO and PO [54]. The primary feed can be, e.g., a horn, a microstrip or a dipole antenna. Reflector and lens antennas can be divided to common antenna types and to shaped antennas. Reflector and lens antennas can also be divided to collimating and diverging-beam antennas. High gain can be achieved with a collimating antenna. A feed system for a CATR is an example of a diverging-beam shaped antenna [13], [16].

Common reflector antennas are presented in Section 4.1 and lens antennas in Section 4.2. Synthesis methods for shaped antennas are presented in Section 4.4. The antenna type and requirements for a feed system for hologram-type CATR are specified in Section 4.5.

4.1 Reflector antennas

Reflector antennas are widely used in telecommunication applications, radars, and radio astronomy. Most high-gain antennas are reflector antennas. Reflector antennas are secondary radiators, which redirect the radiation of the primary source, the feed. The feed is usually a small horn antenna. Also feed arrays can be used. Reflector antenna has usually one or two reflectors.

In general, the reflector can be of any shape but most reflector antennas are based on a rotated conic section [59]: plane, hyperboloid, paraboloid, ellipsoid, or sphere. Properties of rotated conic sections are discussed in Section 4.1.1. Also shaped reflectors are usually based on these basic shapes and can be described as (nearly) planar, hyperbolical, etc.

In Section 4.1.2, collimating reflector antennas are presented. Collimating reflector antennas are based on a parabolic reflector. Diverging-beam antennas based on hyperboloids and/or ellipsoids are presented in Section 4.1.3.

4.1.1 Rotated conic sections

Many reflector antennas are based on rotated conic sections because of their geometrical properties. An illustration of conic sections is in Figure 4.1. A line, a hyperbola, a parabola, an ellipse, and a circle are special cases of a general conic section.

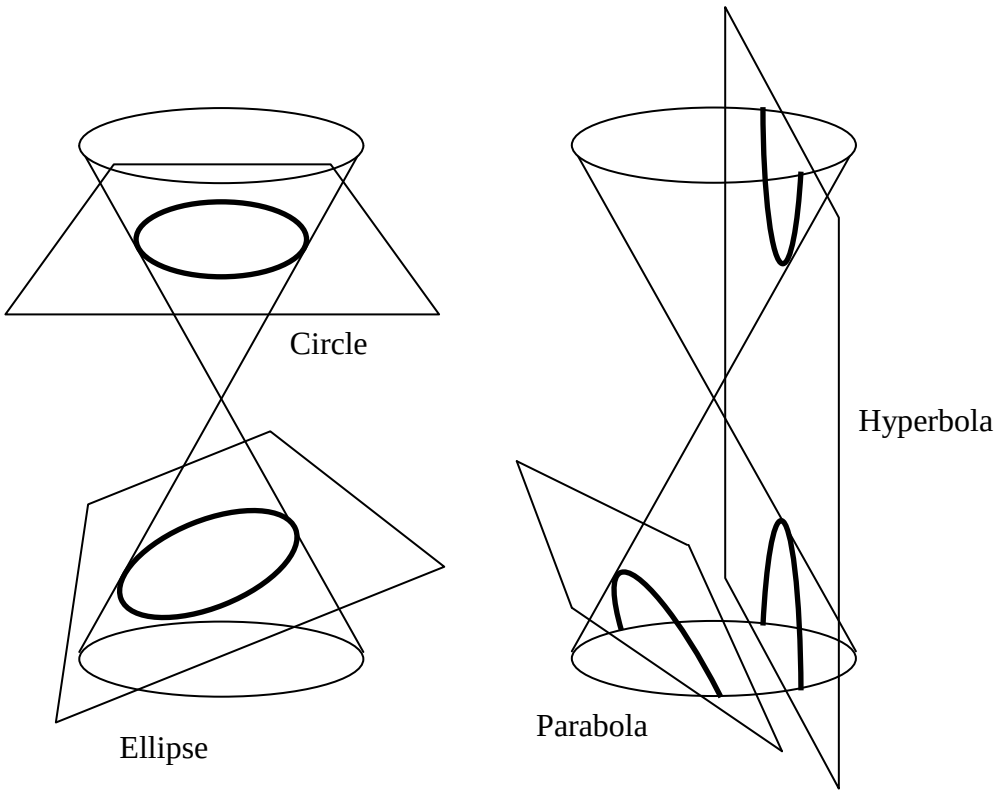

Figure 4.1: A conic section is an intersection of a plane and one or two napes of a cone.

Paraboloid, ellipsoid, and hyperboloid have special focusing properties. Focusing properties reflectors based on these rotated conic sections are illustrated in Figure 4.2. Rays starting from a focal point (one of the focal points) are also drawn in Figure 4.2.

Rays reflected from a paraboloid are parallel, i.e., collimated.

Rays starting from one focal point of an ellipsoid are reflected to the other focal point.

Rays starting from one focal point of a hyperboloid are reflected so that they appear to come from the other focal point.

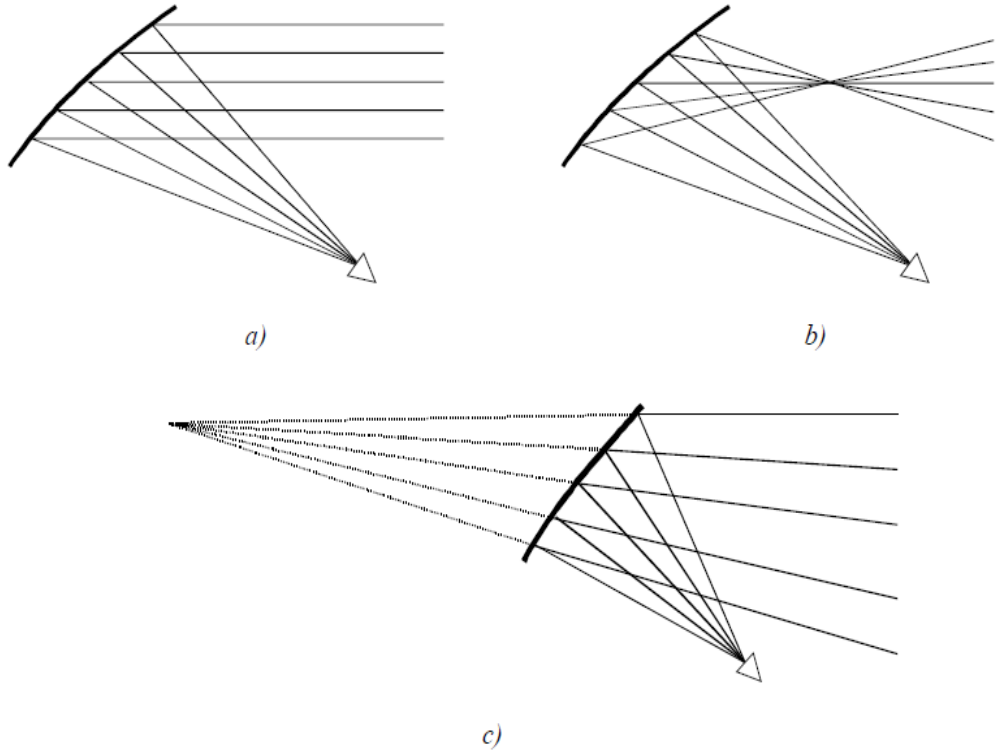

Figure 4.2: Focusing properties of rotated conic sections; a) paraboloid, b) ellipsoid, and c) hyperboloid [13].

All rotated conic sections can be expressed with the following equation [54]:

$$r(\theta) = \frac{(1+e)\,f}{1+e\cdot\cos(\theta)}, \tag{4.1}$$

where r is distance from a focal point to the surface in direction θ, e is eccentricity, and f is the focal length (or radius). For a sphere $e = 0$, an ellipsoid $e < 1$, a paraboloid $e = 1$, a hyperboloid $e > 1$ and for a plane $|e| \to \infty$.

4.1.2 Collimating reflector antennas

Collimating reflector antennas are usually based on a paraboloid reflector. A paraboloid reflector antenna is the easiest and cheapest type of antenna to get a high directivity, for example in communication applications.

A paraboloid collimates the radiation coming from a focal point, i.e., transforms a spherical wave to a plane wave, as illustrated in Figure 4.2 a). The paraboloid can be fed directly from the focal point or a subreflector antenna can be used whose focal point coincides with the focal point of the paraboloid. In a Cassegrain antenna a hyperboloid subreflector is used. If an ellipsoid subreflector is used then it is called a Gregorian antenna. The Cassegrain geometry is more common because the structure is more compact.

A single paraboloid reflector, Cassegrain, or Gregorian antenna can be either centre fed or offset antenna. With offset structure the aperture blockage effect of the feed or

subreflector and its supports can be avoided. Aperture blockage causes lowered aperture efficiency and increased side-lobe level. Figure 4.3 shows a Cassegrain antenna fed from the vertex of the paraboloid and an offset Cassegrain antenna.

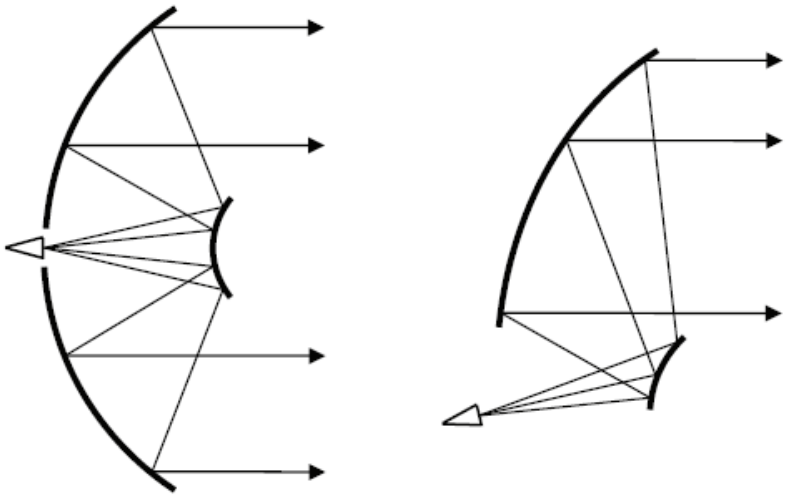

Figure 4.3: Centre fed and offset Cassegrain antennas.

The offset structure causes higher cross-polarisation than the symmetrical centre fed geometry. For example, the cross-polarization level is typically -20 dB to -25 dB for a single offset reflector [55]. The cross-polarization caused by the offset structure can be minimized with so called compensated design that is based on the Mizugutch condition [37]. The Mizugutch condition is also called "the basic design equation" for offset dual reflector antennas and its derivation is given e.g. in [60]. The Mizugutch condition is based on choosing correctly the subreflector eccentricity and the angles between subreflector and main reflector.

The Mizugutch condition to cancel the cross-polarisation component of an offset paraboloidal reflector antenna is [37]:

$$\tan(\alpha) = \frac{\left|1 - e^2\right| \sin(\beta)}{\left(1 + e^2\right)\cos(\beta) - 2e}, \tag{4.2}$$

where α is the angle between the feed axis and axis of the subreflector, β is the angle between the axis of the subreflector and that of the paraboloidal main reflector, and e is the eccentricity of the subreflector (ellipsoid $e < 1$ or hyperboloid $e > 1$) [37]. As an example, a Gregorian geometry is illustrated in Figure 4.4.

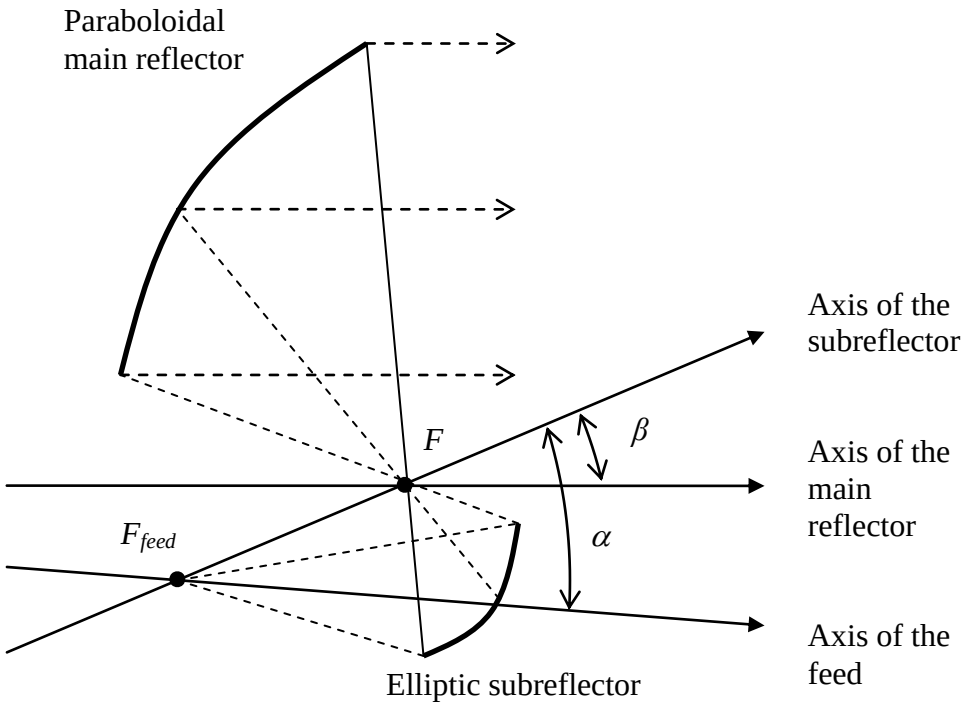

Figure 4.4: Geometry of a Gregorian type offset reflector antenna. The focal point of the main reflector is F and the focal points of the subreflector are F and F_{feed}.

4.1.3 Diverging-beam reflector antennas

The basic diverging-beam reflector antennas are based on using ellipsoid and/or hyperboloid reflectors. Ellipsoid and hyperboloid reflectors, due to their optical focusing properties, can be used to relocate the focal point of the antenna system. Ellipsoids/hyperboloids do not collimate the radiation to one direction and therefore they alone cannot be used for high gain antenna. Dual reflector ellipsoid/hyperboloid geometry is mainly usable for initial condition for a shaped-beam reflector antenna.

The Mizugutch condition for hyperboloids and ellipsoids is derived in [38]:

$$\tan(\beta) = \frac{-e_m\left(1-e_s^{\,2}\right)\sin(\alpha)}{e_m\left(1+e_s^{\,2}\right)\cos(\alpha)-e_s\left(1+e_m^{\,2}\right)}, \tag{4.3}$$

where the subscripts *m* and *s* stand for the main and the subreflector, respectively, and *e*'s are the eccentricities of the surfaces, α is the tilted angle of the subreflector axis with respect to the axis of main reflector and β is the angle between the axis of subreflector and the axis of feed [38]. As an example, ellipsoid-hyperboloid geometry is illustrated in Figure 4.5.

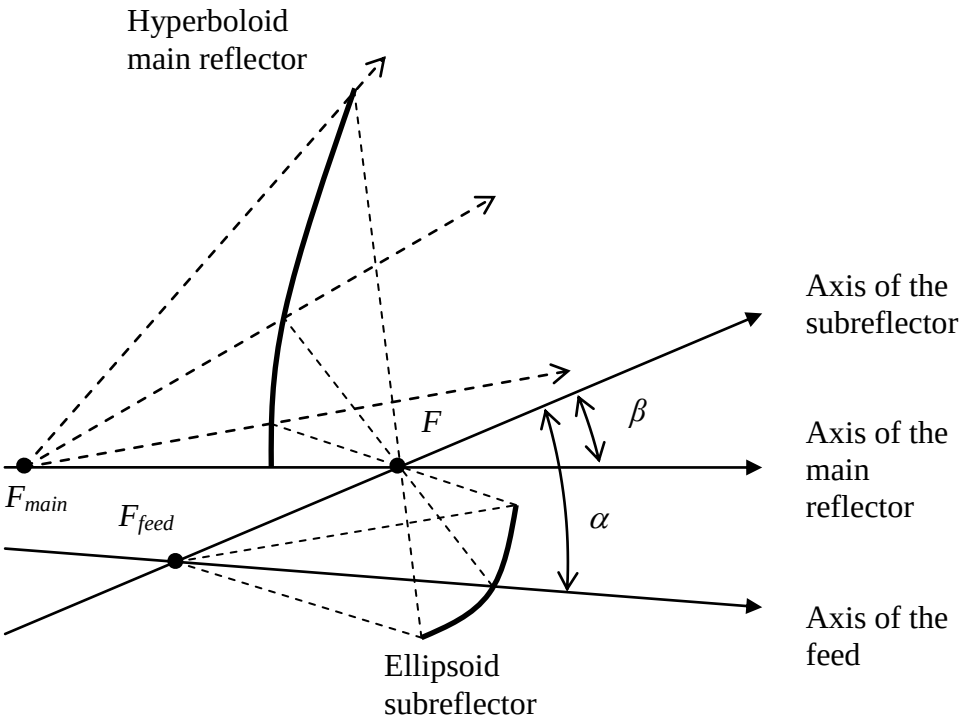

Figure 4.5: Geometry of ellipsoid-hyperboloid reflector antenna. The focal points of the ellipsoid subreflector are F and F_{feed} and the focal points of the hyperboloid main reflector are F and F_{main}.

The dual reflector feed systems, in Chapter 6, are based on the dual offset hyperboloid-hyperboloid geometry. The reflector surfaces are shaped surfaces, not hyperboloids. For both sub- and main reflectors one focal point is behind the reflector surface, therefore the geometry is similar to the hyperboloid-hyperboloid geometry.

4.2 Lens antennas

Lens antennas use refraction from an interface between two media to change the radiation pattern of a primary feed. Most lens antennas are made of dielectric material. Large lens antennas are usually designed and analysed with geometrical optics. Lens antennas can be divided into dielectric lens antennas and substrate lenses [61]. Dielectric lens antenna is illuminated from one side by the primary source, e.g. a horn. In substrate lenses the source is attached directly to the back of the lens. Lens antennas can be made of homogenous material, pieces of different homogenous materials or non-homogenous material.

Lens shape can be made of rotated conic section. A simple collimating dielectric lens antenna can be made of lens with hyperboloid and planar surface [54], shown in Figure 4.6 (right-hand-side). Both the eccentricity of the hyperboloid surface and the permittivity of the lens material need to be chosen correctly. This kind of lens can be very thick and heavy. The lens can be made thinner by removing the material in the direction of the rays. This kind of thin lens is called a Fresnel lens, shown in Figure 4.6 (left-hand-side).

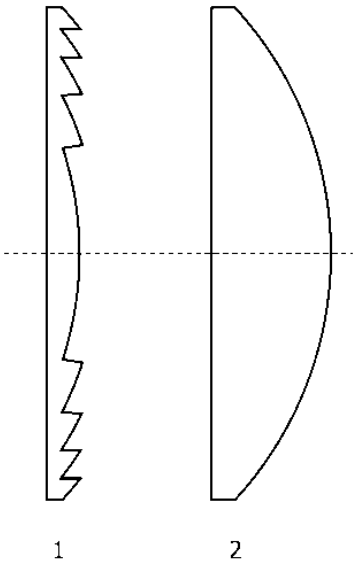

Figure 4.6: Examples of dielectric lens antennas; 1) Fresnel, and 2) hyperboloid.

Substrate lens made of an ellipsoid fed from a focal point is a collimating antenna. The eccentricity has to be equal to 1/*n*, where *n* is the refractive index of the lens material [62]. The elliptical lens can be approximated with a simple extended hemispherical lens [62]. The synthesised ellipsoid with an extended hemispherical lens and a true ellipsoid lens shape examples are illustrated in Figure 4.7.

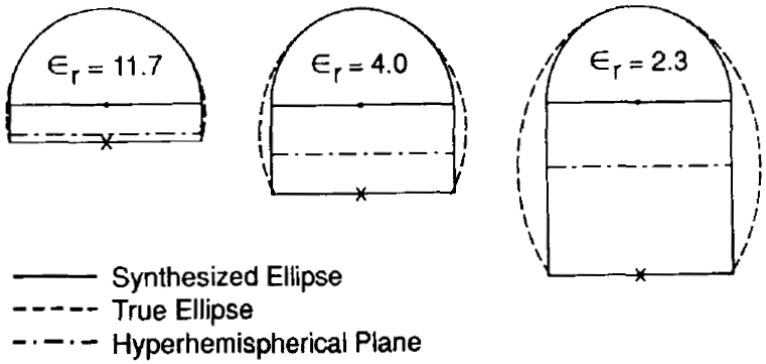

Figure 4.7: An example of a substrate lens: synthesised ellipsoid with an extended hemispherical lens [62].

Classical example of a non-homogenous lens antenna is a Luneburg lens [63], [64]. An ideal Luneburg lens is a sphere with a varying relative permittivity that follows the following equation: [63]

$$\varepsilon_r(r) = 2 - \left(\frac{r}{R}\right)^2, \tag{4.4}$$

where *r* is distance from the centre and *R* is the radius of the lens. The ray paths inside a Luneburg lens are illustrated in Figure 4.8. The lens collimates all rays from the focal

point. In practice, the Luneburg lens is usually realised as a radially uniform multishell spherical lens [63].

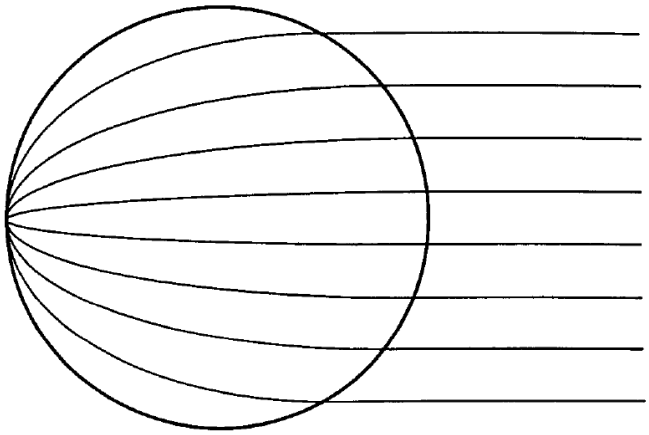

Figure 4.8: Ray paths in a Luneburg lens [64].

4.3 Shaped antennas

Reflector and lens antennas with non-canonical shape are called shaped antennas. The antenna performance can be improved by shaping the reflector or lens surfaces. The surfaces are shaped to achieve the desired property, such as for example; maximum gain, the shape or size of the antenna, desired edge illumination, minimal cross-polarization, nulls to desired directions, side lobe level, desired output beam shape, etc. The design goal depends on the application. Synthesis methods for shaped antennas are presented in Section 4.4.

4.4 Synthesis methods for shaped antennas

Antenna synthesis means that the reflector or lens surfaces are calculated, i.e., synthesised, by some means from known feed radiation and desired radiation of the antenna. Synthesis methods can be divided into different groups in many ways.

The synthesis methods can be divided into direct and indirect methods. In indirect methods the aperture field of the antenna is calculated from the desired far-field and the shaped surfaces are synthesised to produce that aperture field. The direct methods use the desired far-field in the synthesis.

The synthesis methods can be divided based in which method is used to calculate the electromagnetic fields. Most synthesis methods are based on geometrical optics or physical optics. Physical optics methods are sometimes called diffraction synthesis methods because diffracted fields are often included by using physical theory of diffraction. Also other methods can be used, such as integral equations or FDTD.

Some synthesis methods are based on using an optimisation method, in which, the surface shape is changed directly and then the antenna is analysed and compared to the design objective. Usually synthesis method is used with some kind of optimisation. Then

the synthesis objective (or basic geometry etc.) is changed, the shaped surfaces synthesised, and then the antenna is analysed and compared to the design objective.

Synthesis methods are usually developed for a specific antenna type. Synthesis method can be divided for reflector synthesis methods and lens synthesis methods. Some synthesis methods can be used for both reflector and lens antennas.

The synthesis method used to design feed systems for hologram-based CATR is numerical geometrical optics based direct synthesis method that is used together with an iterative optimisation. This synthesis method is explained in detail in Chapter 5.

In Sections 4.4.1 and 4.4.2, some examples of reflector synthesis methods are presented. Examples of lens synthesis methods are presented in Sections 4.4.3 and 4.4.4.

4.4.1 Reflector synthesis methods

A GO-based indirect synthesis method is presented in [65]. The shaped dual reflector surfaces are determined by solving a pair of first-order ordinary nonlinear differential equations. Example of dual-reflector system which will produce a uniform phase and amplitude distribution in the aperture of reflector is given.

A GO-based indirect synthesis method based on solving a nonlinear second-order partial differential equation of the Monge-Ampère type is presented in [66]. The method is used for offset dual reflectors. A similar method is presented in [67].

An example of direct PO-based synthesis is in [68]. The reflector surfaces are characterized with polynomials and Fourier series and optimised based on PO simulations in comparison to desired gain pattern.

An indirect PO-based method is described in [69]. In this method, GO using Monge-Ampère approach is used as a starting point for the final PO optimisation. A numerical example of a contour-beam shaped reflector antenna is given.

A generalized diffraction synthesis technique is described in [70], where the synthesis method combines optimisation procedures, physical optics and diffraction analysis with the physical theory of diffraction. The shaped reflectors are represented by a set of orthogonal global expansion functions and optimised with a safeguarded Newton's method. The synthesis is generalized for single- and dual-reflector antennas fed by either a single feed or an array feed.

A direct PO-based method using the successive projections method is presented in [71]. As an example, the technique is used to design a satellite antenna providing shaped beam for a regional coverage area.

4.4.2 Ray-tracing based reflector synthesis methods

An indirect ray-tracing based synthesis method is presented in [72]. It is formulated for a shaped dual offset reflector antenna based on a basic geometry of either a Cassegrain or a Gregorian system. Rotational symmetry is assumed for feed pattern and for the desired aperture field pattern. First-order approximation is used for the surfaces.

Reflector surfaces and wave-fronts are described in terms of curvature parameters of the bi-parabolic expansions in [73]. It is an indirect ray-tracing based synthesis method for dual offset reflector antennas. To get the aperture mapping exact extra variables are added to the mapping, i.e., by allowing the radial lines of the aperture ray grid to be curved. Using the bi-parabolic expansions for surfaces and wave-fronts makes the solution easier to control [73]. The synthesis technique has been used for shaped offset dual reflectors antennas and for a dual reflector feed for a spherical reflector.

In [35], an indirect ray-tracing based synthesis method, with first-order approximation for the surfaces, is presented. The method is used to design a dual reflector feed system (DRFS) for a single reflector CATR. The system is described as a tri-reflector system with two shaped reflectors of the DRFS and the parabolic reflector of the original CATR. Another indirect ray-tracing based synthesis method, with first-order approximation for the surfaces, is presented in [74].

4.4.3 Substrate lens synthesis methods

A direct GO-based method for axis-symmetric substrate lens is presented in [75]. GO is used to obtain a first guess of the lens shape and PO formulation is used to compute the actual far-field radiation pattern. In [76], this method is used for a 3D shaped lens that is interpolated from two profiles that are calculated independently for two planes of the lens. In [77], the method is generalised also for a shaped double-shell dielectric lens antenna.

A direct GO-based method for 3D substrate lenses of arbitrary shape is presented in [78]. Second-order partial-differential equation derived from GO principles is solved with iterative algorithm. Then, a local surface optimisation of the lens profile a multi-dimension conjugate-gradient method is carried out to finally optimise the lens profile.

4.4.4 Dielectric lens synthesis methods

Indirect GO-based dielectric lens synthesis method is presented in [79]. The profiles of rotationally symmetric lens surfaces are calculated numerically from a non-linear differential equation.

Indirect ray-tracing based dielectric lens synthesis method is presented in [43]. A first-order approximation is used for the surfaces of the rotationally symmetric lens. Also, coma correction zoning is used to correct the cubic phase errors associated with the shaped lens for off-axis beams [43].

In [80], an asymmetric lens is designed by optimising polynomial describing the second surface of the lens, while the first surface collimates the beam. The shaped surface is used to produce a shaped phase distribution to the aperture. GO and two dimensional integration of the aperture distribution is used to calculate radiation patterns.

In [81], a multi-beam lens antenna is designed by optimising the coordinates of the lens shape and the feed positions with a genetic algorithm (GA). The radiation patterns are calculated with ray-racing and aperture integration. The GA optimisation is done based on both high gain and low side-lobe level requirements.

4.5 Feed systems for hologram-based CATR

Feed system for a hologram-based CATR is used to provide the desired modified illumination for the hologram. The advantages of using a modified illumination are discussed in Section 2.3.3.2. Desired modified illumination has a spherical wave, low cross-polarisation, and amplitude pattern with flat amplitude to the centre of the hologram and edge tapering to the hologram edge. The desired main polarisation amplitude distribution is illustrated in Figure 4.9.

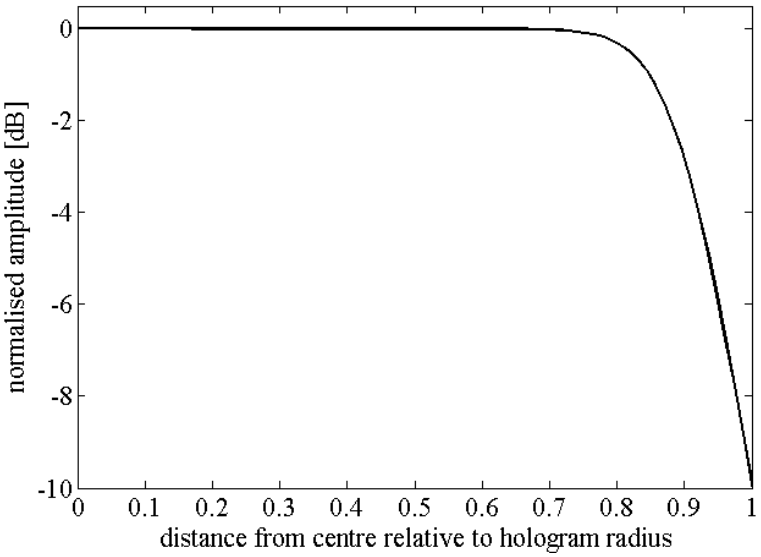

Figure 4.9: Desired hologram illumination; rotationally symmetric Butterworth-type amplitude pattern.

A feed system with two shaped surfaces is used to modify both the amplitude and phase patterns of a primary feed. A feed system for a hologram-based CATR is either a dual reflector feed system (DRFS), explained in Chapter 6, or a shaped lens feed system, explained in Chapter 7. In practice, the first shaped surface modifies the amplitude pattern and the second corrects the phase pattern.

A corrugated horn is a good choice for a primary feed because corrugated horn typically has a symmetrical beam and low cross-polarisation. A corrugated feed horn has been used as the feed in all the designed feed systems for hologram-based CATR. Amplitude and phase patterns of a 650 GHz feed horn are shown in Figure 4.10.

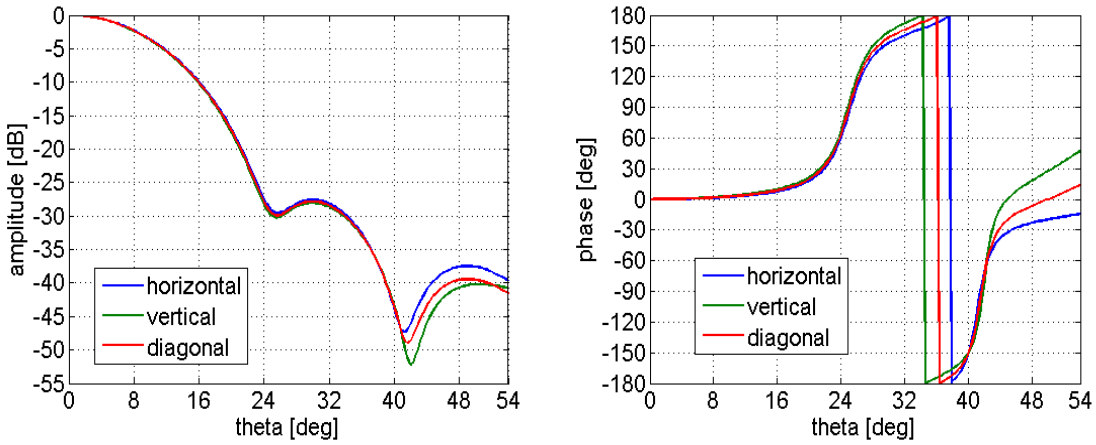

Figure 4.10: Feed horn radiation pattern; amplitude and phase of the horizontal, vertical and diagonal cuts at the vertical polarisation.

The feed system modifies the feed radiation pattern in Figure 4.10 into the hologram illumination in Figure 4.9. In general, the hologram is not in the far-field of the feed system, therefore the far-field pattern of the feed system is not of interest. The feed system is designed to provide the illumination for the hologram area to a given distance, i.e., to a circular area with the hologram diameter D_{holo} at distance of the hologram focal length f_{holo}. In practice, a feed system can be used for any hologram if the ratio f_{holo}/D_{holo} remains the same.

A hologram, designed for a modified illumination, is used only to transform the spherical wave to a plane wave. Therefore, the amplitude pattern of the illumination, i.e., the width of the area with the flat amplitude, determines the QZ size. The beam width of the feed system needs to be as wide as possible. Amplitude tapering is needed to the edge of the hologram to avoid strong diffraction from the hologram edges. The combination of a wide beam and amplitude tapering to the edge is difficult to realise and a compromise has to be made.

5 Numerical synthesis method

Numerical synthesis method for designing a feed system for a hologram-based CATR is described in this chapter. The synthesis method was developed specifically for designing a dual reflector feed system (DRFS) for a hologram-based compact antenna test range (CATR) [14], [13]. In this thesis the method is generalised also for lens antenna feed systems. Both reflector and lens feed systems are based on modifying the field radiated by the primary feed with two shaped surfaces.

The synthesis method is a direct ray-tracing-based synthesis procedure, that is based on the method described in [73] with some simplifications. In the synthesis the electromagnetic fields are represented with rays that represent the local plane wave amplitude and phase. The surfaces are approximated with locally planar sections. The synthesis of the feed system starts with defining the basic geometry. Then input and output fields and rays are defined. Finally, the reflector (or lens) surfaces are synthesised and the edges are rounded.

This synthesis method was developed because existing synthesis methods were not directly applicable [13]. For example, methods in [35] and [74] are based on similar ray-tracing principles, but are developed for different antenna type. This results in a somewhat different approach in the synthesis [13]. Also, the optimisation procedure, as explained in Section 5.2, is an important part of the developed synthesis method.

The basic properties of rays and ray-tracing are explained in Section 5.1 in homogenous, isotropic, lossless medium using the local plane wave approximation for the wave fronts. Section 5.1 provides the ray properties that are used in the synthesis of shaped surfaces in Section 5.3 and in ray-tracing simulation in Section 5.4.2.

The design procedure, explained in Section 5.2, is an iterative process in which the shaped antenna structure is synthesised (Section 5.3), simulated (Section 5.4) and the simulation results analysed. The antenna parameters are optimised based on the simulation results.

Two dual reflector feed systems have been designed using this synthesis method, one for 310 GHz [14], [13] and one for 650 GHz [16], [17]. These feed systems are presented in Chapter 6. Design of the 650 GHz DRFS is presented in more detail in Section 6.2. A lens antenna feed system is presented in Chapter 7 to demonstrate that the synthesis method is usable also for lens antennas.

5.1 Properties of rays and ray-tracing

Properties of geometrical optics fields and rays are described in this section in homogenous, isotropic, lossless medium using a local plane wave approximation for the wave fronts. These ray properties are derived from the theory of geometrical optics introduced in Section 3.4. With these approximations the geometrical optics equations are greatly simplified. In ray-tracing, a geometrical optics field is represented with a discrete number of rays, the path of each ray is calculated, and then the field is calculated from the known rays.

The purpose of this section is to provide a detailed list of ray properties with the approximations listed above. First rays and ray tubes are defined and then their properties and relation to fields are explained in the following sub-sections. Some of the ray properties, described in this section, are not used in the synthesis of feed systems. Most importantly polarisation properties are not taken into account in the synthesis.

5.1.1 Ray, ray tube, and field

A ray is a local representation of the electro-magnetic field. A ray represents a plane wave. Ray properties are the starting point, end point, direction, length, properties of the medium, and complex electric field vector (field amplitude, phase, and polarisation). Field phase changes along the ray, therefore, it has to be defined at least at some point along the ray. The ray amplitude is not (necessarily) the same as the field amplitude (Section 5.1.7).

A ray tube is a volume between rays (see example in Figure 5.4).

A field is a complex valued vector field $\bar{E}$. A field is defined as continuous function or in discrete points. A field has amplitude, phase and polarisation.

5.1.2 Ray direction

In general, a ray path is solved from Equation (3.29) (ray equation). For homogenous medium *n(r) = n*, a ray can be described simply as

$$\bar{r}_0 + s\bar{r}, \tag{5.1}$$

where *s* is distance along a ray and $\bar{r}$ is the ray direction and $\bar{r}_0$ is the starting point of the ray. A ray in a homogenous medium is a straight line. The ray represents the direction of propagation, which is the same as that of the local wave vector $\bar{k}(\bar{r})$.

5.1.3 First-order wave front approximation

A wave front is a surface where the field phase is constant. A wave front is normal to a ray direction. In GO, the wave front is approximated locally for each ray. Often the wave front is approximated with a second-order approximation that is characterised with two principal radii and directions of curvature [54], [55], [73]. A wave front can also be approximated with a plane-wave, i.e., a first-order approximation [13], [16]. The second- and first-order approximations are illustrated in Figure 5.1.

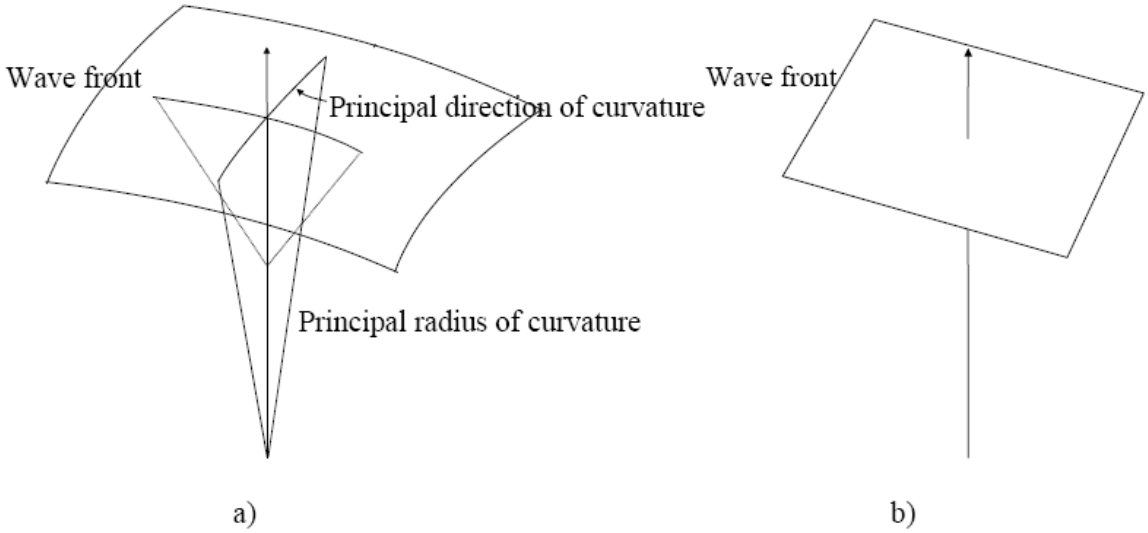

Figure 5.1: Local approximation of a wave front; a) second-order and b) first-order approximation [13].

The most important difference between these approximations is that with the second-order approximation amplitude changes along a ray, which is described with the wave front curvature parameters. With the first-order approximation the ray amplitude does not change along the ray and the changing field amplitude is represented (or calculated) using ray tubes as explained in Section 5.1.7.

5.1.4 Amplitude, phase, and polarisation along a ray

One ray represents a plane wave in a homogenous, isotropic, lossless medium. The ray amplitude $\left|\overline{E}\right|$ or polarisation does not change along the ray. Phase decreases along the ray linearly in the direction of propagation (ray direction), so that distance of one wavelength corresponds to a phase change of -360°. The phase Ψ depends on a distance *s* along a ray as:

$$\Psi(s) = -ks = -\frac{2\pi}{\lambda}s = -\frac{2\pi}{\lambda_0}\sqrt{\varepsilon_r \mu_r}\, s\,. \tag{5.2}$$

With one ray (or parallel rays), if the field is known at a point s_0 along the ray, the field at point *s* along the ray is:

$$\overline{E}(s) = \overline{E}(s_0)e^{-jk(s-s_0)}\,. \tag{5.3}$$

The field phase is a relative quantity defined in relation to a phase reference; therefore also the ray length calculated from the field phase is a relative quantity.

5.1.5 Ray direction and known focal point

Ray directions can be determined from a known far-field pattern that is defined as an angular field distribution originating from a focal point. All rays originate from the focal point. The field phase affects the ray length, not the ray direction.

5.1.6 Ray direction and field phase

The ray direction can be determined from a known field phase. The phase derivatives determine tangential vectors of a plane, i.e., the constant phase wave front of a plane wave. The wave front plane is determined from the phase derivatives using the relation of the phase and ray length in (5.2). The ray direction is normal to the wave front plane.

For example, let's consider a rotationally symmetric geometry in Figure 5.2. The field phase is known on z = 0 plane and the phase pattern is rotationally symmetric, i.e., $\partial\Psi / \partial\phi = 0$. The field source is known to be somewhere above the z = 0 plane. The ray direction angle θ, angle relative to the z-axis, is [82]:

$$\sin(\theta) = -\frac{1}{k}\frac{\partial\Psi}{\partial\rho}. \tag{5.4}$$

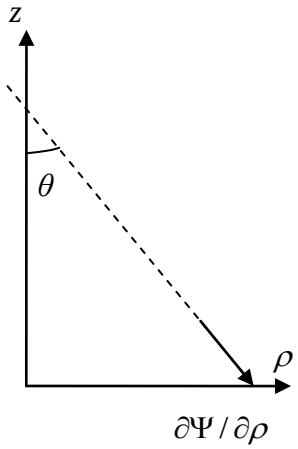

Figure 5.2: Determining ray direction from field phase; a rotationally symmetric geometry.

Similarly, if the field is known at discrete points, the ray direction can be calculated from the geometry shown in Figure 5.3, where Δs is calculated from the phase difference:

$$\Delta s = -\frac{\lambda}{2\pi}\left(\Psi(n+1) - \Psi(n)\right). \tag{5.5}$$

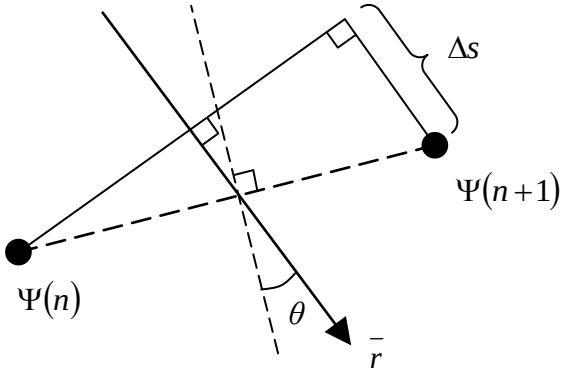

Figure 5.3: Determination of ray direction from known field phase in case of $\Psi(n+1) < \Psi(n)$.

5.1.7 Power, amplitude and ray tubes

Power stays inside a volume bounded by rays, i.e., inside a ray tube. Power density varies as a function of cross-sectional area of the ray tube. Power that propagates in a ray tube that has cross-sectional surface *S* is calculated from the real part of Poynting's vector

$$P = \frac{1}{2}\mathrm{Re}\left\{\int_S \overline{E} \times \overline{H}^* \cdot \overline{dS}\right\} = \frac{1}{2\eta}\int_S \left|\overline{E}\right|^2 \bar{r} \cdot \bar{n} dS, \tag{5.6}$$

where $\overline{E}$ is the electric field on the surface *S*, $\bar{r}$ is ray direction unit vector and $\bar{n}$ is normal unit vector of the surface *S*.

Lets examine a simple ray tube between three rays $\bar{r}_1$, $\bar{r}_2$, and $\bar{r}_3$ with electric fields $\overline{E}_1$, $\overline{E}_2$, and $\overline{E}_3$, respectively. The ray tube and its planar cross-section are shown in Figure 5.4. In general, a ray tube can be defined between anything from three to an infinite number of rays and the cross-section does not have to be a plane. Three rays and planar cross-section is the simplest example without making assumptions on the ray directions.

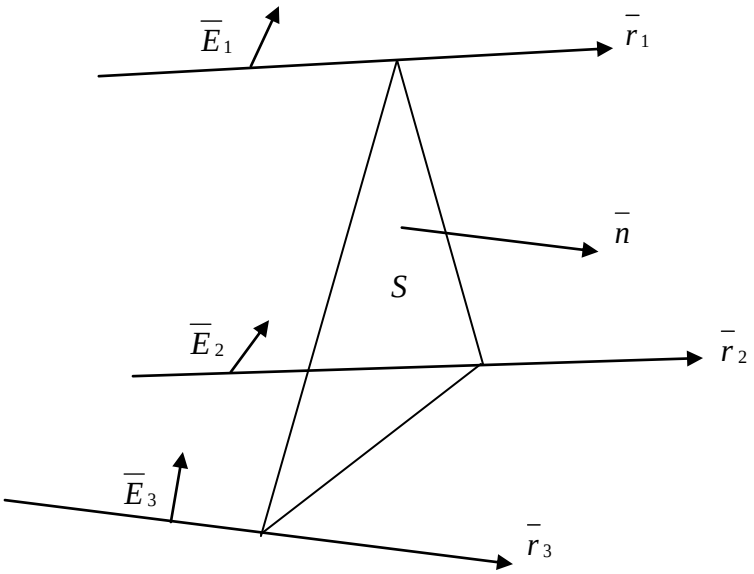

Figure 5.4: Example of a ray tube and its planar cross-section.

The power going through surface *S* in Figure 5.4 cannot be calculated exactly because the electric field and ray directions are known only on the discrete points where the rays intersect the surface. Integral in (5.6) can be approximated for example with an average

$$P = \frac{1}{2\eta}\int_S \left|\bar{E}\right|^2 \bar{r}\cdot\bar{n}dS \approx \frac{1}{2\eta}\frac{A}{3}\left[\left|\bar{E}_1\right|^2\left(\bar{r}_1\cdot\bar{n}\right)+\left|\bar{E}_2\right|^2\left(\bar{r}_2\cdot\bar{n}\right)+\left|\bar{E}_3\right|^2\left(\bar{r}_3\cdot\bar{n}\right)\right]. \qquad (5.7)$$

Sometimes it can be approximated that $\bar{r}\cdot\bar{n}\approx 1$. This approximation is accurate if the ray direction $\bar{r}$ is parallel to the normal vector $\bar{n}$ of the cross-sectional surface, i.e., if the rays are parallel (or almost parallel) to each other and to the normal $\bar{n}$. In this case the tube power is simply

$$P \approx \frac{1}{2\eta}E_{ave}^2 A, \qquad (5.8)$$

where E_{ave}^2 is the average of squared amplitudes of the rays that define the tube.

5.1.8 Reflection and refraction from a planar surface

When a ray (a plane-wave) encounters a boundary between two different media it is reflected and refracted from the boundary, as illustrated in Figure 5.5. The incident wave comes at an angle θ_1 compared to the normal $\bar{n}$. Part of the incident wave is reflected at an angle θ'_1 and a part is refracted (transmitted) into medium 2 at an angle θ_2. The tangential components of the wave vectors are identical.

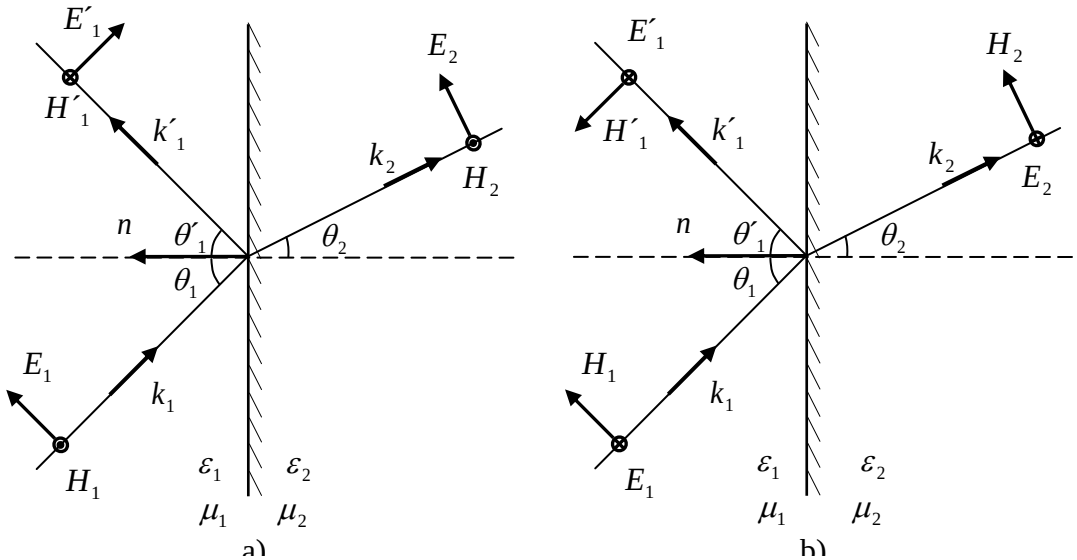

Figure 5.5: Reflection and refraction of a plane wave at a planar interface of two lossless media: a) parallel polarisation, and b) perpendicular polarisation [83].

Let us assume in the following that $\mu_1 = \mu_2 = \mu_0$. The angle of incidence and the angle of reflection are equal $\theta_1 = \theta'_1$ and the refraction angle is calculated from Snell's law [83]:

$$n_1 \sin(\theta_1) = n_2 \sin(\theta_2), \tag{5.9}$$

where $n_1 = \sqrt{\varepsilon_{r1}}$ and $n_2 = \sqrt{\varepsilon_{r2}}$ are the refractive indices of the two media.

The polarisation of the incident wave can be thought to be a superposition of parallel (transverse magnetic- or TM-polarisation) and perpendicular (transverse electric- or TE-polarisation) polarisations. Reflection $\rho_{\parallel}$ and transmission $\tau_{\parallel}$ coefficients for parallel polarisation are [83]:

$$\rho_{\parallel} = \frac{E'_1}{E_1} = \frac{\sqrt{\frac{\varepsilon_2}{\varepsilon_1} - \sin^2\theta_1} - \frac{\varepsilon_2}{\varepsilon_1}\cos\theta_1}{\sqrt{\frac{\varepsilon_2}{\varepsilon_1} - \sin^2\theta_1} + \frac{\varepsilon_2}{\varepsilon_1}\cos\theta_1} \tag{5.10}$$

$$\tau_{\parallel} = \frac{E_2}{E_1} = \frac{2\sqrt{\frac{\varepsilon_2}{\varepsilon_1}}\cos\theta_1}{\sqrt{\frac{\varepsilon_2}{\varepsilon_1} - \sin^2\theta_1} + \frac{\varepsilon_2}{\varepsilon_1}\cos\theta_1}. \tag{5.11}$$

Reflection $\rho_{\perp}$ and transmission $\tau_{\perp}$ coefficients for perpendicular polarisation are [83]:

$$\rho_{\perp} = \frac{E'_1}{E_1} = \frac{\cos\theta_1 - \sqrt{\frac{\varepsilon_2}{\varepsilon_1} - \sin^2\theta_1}}{\sqrt{\frac{\varepsilon_2}{\varepsilon_1} - \sin^2\theta_1} + \cos\theta_1} \tag{5.12}$$

$$\tau_{\parallel} = \frac{E_2}{E_1} = \frac{2\cos\theta_1}{\sqrt{\frac{\varepsilon_2}{\varepsilon_1} - \sin^2\theta_1} + \cos\theta_1}. \tag{5.13}$$

In (5.10) – (5.13), E_1, E'_1, and E_2 are the ray amplitudes of the incident, reflected, and refracted rays, respectively.

Ray directions can be calculated from Snell's law and the geometry in Figure 5.5. Other possibility is to calculate the wave vectors $\bar{k}_1$, $\bar{k}'_1$, and $\bar{k}_2$, as the ray direction is the same as the wave vector direction. The tangential components of these wave vectors are identical and the wave-numbers $|\bar{k}_1| = |\bar{k}'_1|$ and $|\bar{k}_2|$ are known:

If $\varepsilon_1 > \varepsilon_2$, a total reflection occurs if [83]:

$$\theta_1 \geq \sin^{-1}\sqrt{\frac{\varepsilon_2}{\varepsilon_1}}. \tag{5.14}$$

In case of a total reflection, reflection coefficients become complex numbers and $|\rho_{\parallel}| = 1$ and $|\rho_{\perp}| = 1$, i.e., all of the incoming power is reflected. Reflection coefficients are calculated from (5.10) and (5.12) and they affect only the phase of the reflected ray. The ray amplitude of the refracted ray is set to zero $E_2 = 0$.

In general, metal can be considered to be perfect electric conductor (PEC). Reflection coefficient from metal surface for all polarisations and for all incident angles is $\rho = -1$.

5.1.9 Polarisation of reflected and refracted rays

The electric field vectors of the reflected and refracted (transmitted) rays are calculated first by dividing the incident field $\bar{E}_1$ to the parallel $E_1^{\parallel}\bar{u}_1^{\parallel}$ and perpendicular $E_1^{\perp}\bar{u}_1^{\perp}$ components.

$$\bar{E}_1 = E_1^{\parallel}\bar{u}_1^{\parallel} + E_1^{\perp}\bar{u}_1^{\perp}, \tag{5.15}$$

where the amplitudes and directional unit vectors are:

$$E_1^{\perp} = \overline{E}_1 \cdot \overline{u}_1^{\perp} \quad , \quad E_1^{\parallel} = \overline{E}_1 \cdot \overline{u}_1^{\parallel}, \tag{5.16}$$

$$\overline{u}_1^{\perp} = \frac{\overline{n} \times \overline{k}_1}{\left| \overline{n} \times \overline{k}_1 \right|} \quad , \quad \overline{u}_1^{\parallel} = \frac{\overline{k}_1 \times \overline{u}_1^{\perp}}{\left| \overline{k}_1 \times \overline{u}_1^{\perp} \right|}. \tag{5.17}$$

The reflected field is:

$$\overline{E'}_1 = \rho_{\parallel} E_1^{\parallel} \overline{u'}_1^{\parallel} + \rho_{\perp} E_1^{\perp} \overline{u'}_1^{\perp}, \tag{5.18}$$

where directional unit vectors of reflected perpendicular and parallel polarisations are:

$$\overline{u'}_1^{\perp} = \frac{\overline{n} \times \overline{k'}_1}{\left| \overline{n} \times \overline{k'}_1 \right|} \quad , \quad \overline{u'}_1^{\parallel} = -\frac{\overline{k'}_1 \times \overline{u'}_1^{\perp}}{\left| \overline{k'}_1 \times \overline{u'}_1^{\perp} \right|} = \frac{\overline{u'}_1^{\perp} \times \overline{k'}_1}{\left| \overline{u'}_1^{\perp} \times \overline{k'}_1 \right|}. \tag{5.19}$$

The refracted (transmitted) field is:

$$\overline{E}_2 = \tau_{\parallel} E_1^{\parallel} \overline{u}_2^{\parallel} + \tau_{\perp} E_1^{\perp} \overline{u}_2^{\perp}, \tag{5.20}$$

where directional unit vectors of refracted perpendicular and parallel polarisations are:

$$\overline{u}_2^{\perp} = \frac{\overline{n} \times \overline{k}_2}{\left| \overline{n} \times \overline{k}_2 \right|} \quad , \quad \overline{u}_2^{\parallel} = \frac{\overline{k}_2 \times \overline{u}_2^{\perp}}{\left| \overline{k}_2 \times \overline{u}_2^{\perp} \right|}. \tag{5.21}$$

In (3.17), (3.19), and (3.21) $\overline{k}_1$, $\overline{k'}_1$, and $\overline{k}_2$ are the wave vectors, i.e., ray directions, and $\overline{n}$ is the surface normal. Field vector, wave vector, and surface normal directions are illustrated in Figure 5.5.

5.2 Feed system design procedure

The iterative design process used to design the feed systems for hologram-based CATRs is shown in Figure 5.6. One iteration round of the design process has three parts: the synthesis of the surfaces, simulations and analysis of the results. The synthesis of a feed system can be divided into three parts: definition of the basic geometry, definition of input and output fields and their representation with rays and the synthesis of the reflector surfaces.

The simulation method depends on the antenna type. The dual reflector feed systems have been simulated with a commercial reflector antenna simulation software GRASP8W [84]. The lens antenna feed systems are simulated with a ray-tracing based simulation method, described in Section 5.4.2. Finally the simulation results are analysed, i.e., the amplitude and the phase are calculated from the simulation results, and compared to previous simulation results.

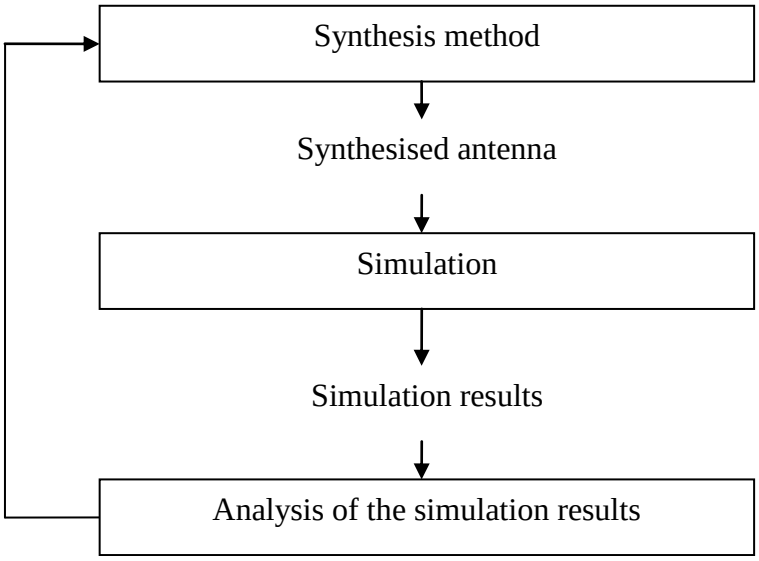

Figure 5.6: Design process.

The design process is an iterative optimisation process. In general, first 1) the parameters of the basic geometry are optimised, then 2) the input and output fields and their representation with rays are optimised, and finally 3) the parameters of the synthesis are optimised. Each of those three steps are discussed separately in detail in Sections 5.3.1 – 5.3.3. In practice the design process is not that straightforward because all of the steps in the design process affect each other.

Each parameter is optimised by synthesizing the surfaces with a number of different values for the parameter. Then the synthesised surfaces are simulated and the results analysed. The best value for the parameter, based on the simulation results, is used when the next parameters are optimised. In this way it is possible to study separately how each parameter affects the radiation of the antenna.

It is most important to find the electrical and geometrical parameters that can and must be optimised. After that it is fairly straightforward (but not easy) to parameterise and to find the optimal parameter values.

5.3 Synthesis of a feed system

The reflector (lens) surfaces are synthesised from known input and output rays and the geometry of the feed system by tracing the rays, using the Snell's law for reflections (refractions) and ray length adjustment. The synthesis has three steps: 1) defining the basic geometry, 2) representation of fields with rays, and 3) the synthesis of the surfaces.

Known information in the beginning of synthesis of the surfaces, in case of a dual reflector feed system, is illustrated in Figure 5.7.

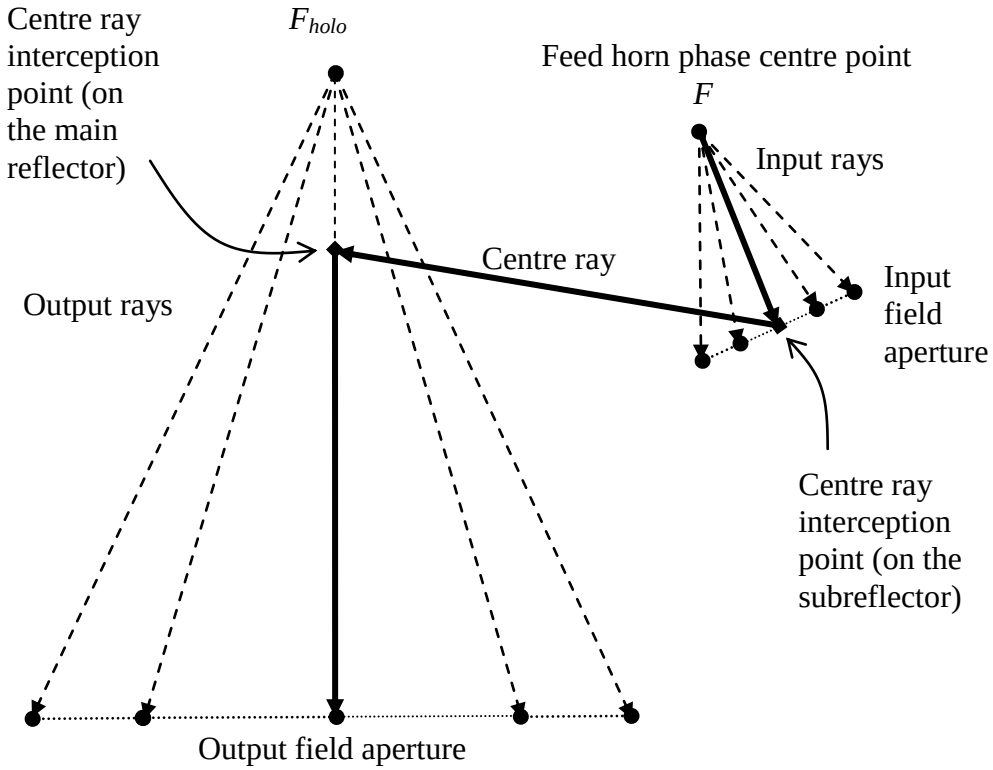

Figure 5.7: Known information in the beginning of synthesis of the surfaces.

The centre ray is known from the basic geometry. The centre ray interception points on the surfaces are the first known points of the surfaces. The origins and the end points of the input and output rays are determined from the focal points (from the geometry) and from the input and output fields.

5.3.1 Basic geometry

The basic geometry definition includes:

1. Two focal points: feed horn phase centre point and focal point of the feed system. The focal point of the feed system is usually the same as the hologram focal point F_{holo}.
2. Centre ray path from the feed horn phase centre point to the centre of the output field aperture, i.e., the hologram. The centre ray defines the first points of the surfaces.
3. Input and output field aperture planes and diameters. Input and output fields are defined in the aperture planes.
4. Coordinate systems; global coordinate system, feed horn coordinate system, input and output aperture plane coordinates.

The definition of the basic geometry is mostly responsible for the size of the reflectors (or lenses) and for the distances between feed horn, reflectors (lenses), and the hologram.

The final shape and size of the reflectors (or lenses) are defined only after the synthesis of the shaped surfaces.

5.3.2 Representation of fields with rays

The electromagnetic fields are represented with rays. A ray represents a plane wave perpendicular to the ray direction.

The ray grid is defined in polar coordinates in the input and output aperture planes, as illustrated in Figure 5.8. The ray grid is $N \times M$ matrix with N rings and M rays on each ring. The first ring is formed by M rays in the centre of the grid and the rays at $\phi = 0^o$ are duplicated at $\phi = 360^o$ to facilitate the calculations. Flux tubes are formed by four adjacent rays. The flux tubes are numbered so that tube (n_{tube}, m_{tube}) is cornered by rays (n_{ray}, m_{ray}), $(n_{ray}, m_{ray}+1)$, $(n_{ray}+1, m_{ray})$, and $(n_{ray}+1, m_{ray}+1)$.

Ray grid in Figure 5.8 is a constant angular and radial polar grid, i.e., a grid with constant $\Delta\phi$ and constant $\Delta\rho$. Sometimes a grid with varying $\Delta\rho$ is used.

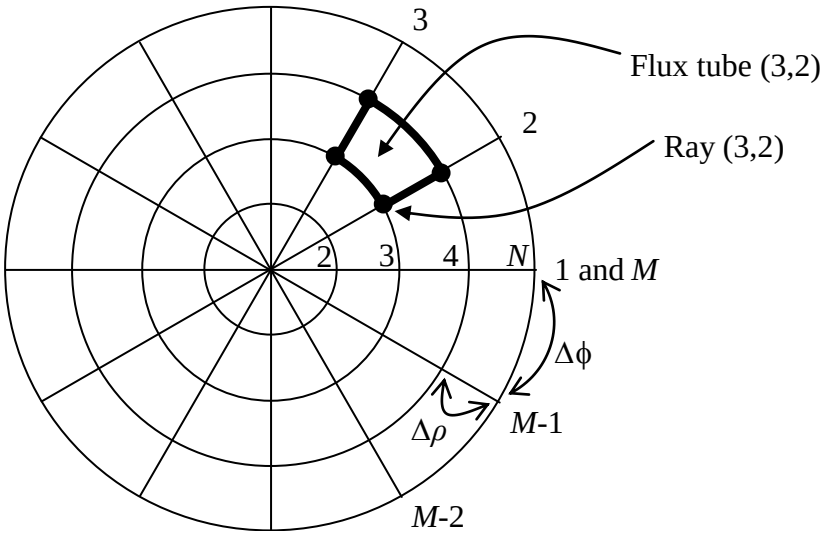

Figure 5.8: Ray grid and flux tubes.

5.3.2.1 Input field

The input ray amplitudes are interpolated from the vertical polarisation, i.e., main polarisation, of the radiation pattern of the feed horn. The input rays are defined so that they originate from the feed horn phase centre point and intersect the input field aperture plane at points defined by the input ray grid at $N \times M$ discrete points. The feed horn phase centre point and the input field aperture plane are illustrated in Figure 5.7. The phase of the feed horn main polarisation can be taken into account in ray length adjustment in the synthesis of the surfaces. Often the feed horn phase pattern has very small effect and it can be neglected in the synthesis.

5.3.2.2 Output field

The output field is defined in the output field aperture plane at constant angular and constant radial polar grid at $N \times M$ discrete points. Finally the output ray grid is determined in the aperture mapping. The output rays originate from the hologram focal point F_{holo} and end in the output field aperture plane, as shown in Figure 5.7. The desired output field (main polarisation) amplitude and phase are defined by the user.

The feed system is used to generate a spherical wave-front with flat amplitude in the centre of the beam and amplitude tapering towards the edge of the hologram. This can be achieved for example using a rotationally symmetric Butterworth-type function for the output field amplitude:

$$E(\rho') = \frac{1}{\sqrt{1+(\rho'/\rho_c)^{2N}}}, \tag{5.22}$$

where ρ_c and N are the –3 dB point and the degree of the Butterworth function and ρ' is the output field aperture coordinate. The output field phase is modified by adjusting the total lengths of the rays in the synthesis of the surfaces.

5.3.2.3 Aperture mapping

The input rays are mapped to the output rays, i.e., the output ray grid is changed so that the power in each ray tube is the same in the output as in the corresponding input ray tube.

The mapping is done in two parts, first the amplitudes of the output rays are scaled to make the total output power equal to the total input power and then the new output field aperture coordinates are calculated so that the power is equal for each ray tube, i.e.,

$$P_{in}(n_{tube}, m_{tube}) = P_{out}(n_{tube}, m_{tube}). \tag{5.23}$$

The input ray amplitudes and the output ray amplitudes have been normalised so that the peak values are set to one. The normalised output ray amplitudes $E_{out,norm}$ are scaled so that the total power of the output flux tubes is equal to the total power of the input flux tubes. The scaling factor α is

$$\alpha = \frac{\sum_{m_{tube}=1}^{M-1}\sum_{n_{tube}=1}^{N-1} P_{in}(n_{tube}, m_{tube})}{\sum_{m_{tube}=1}^{M-1}\sum_{n_{tube}=1}^{N-1} P_{out,norm}(n_{tube}, m_{tube})}. \tag{5.24}$$

The tube powers $P_{in}(n_{tube}, m_{tube})$ and $P_{out,norm}(n_{tube}, m_{tube})$ are calculated from (5.6) or (5.8). The new output field aperture coordinates, i.e., the output ray grid, are calculated from the integral expressions of (5.23) using scaled output ray amplitudes:

$$E_{out}\left(n_{ray},m_{ray}\right)=\sqrt{\alpha}E_{out,norm}\left(n_{ray},m_{ray}\right). \tag{5.25}$$

Aperture mapping does not take into account reflection (or transmission) coefficients or depolarisation ($\bar{u}_{in}^{\perp} \neq \bar{u}_{out}^{\perp}$, $\bar{u}_{in}^{||} \neq \bar{u}_{out}^{||}$).

5.3.2.4 Rotationally symmetric aperture mapping

Aperture mapping is greatly simplified if the fields are assumed to be rotationally symmetric. The ray grids are defined by N ray rings. The output field amplitude is defined as a rotationally symmetric function $E_{out,norm}(n_{ray})$ and the input field is averaged

$$E_{in}(n_{ray})=\frac{\sum_{m_{ray}=1}^{M-1}E_{in}(m_{ray},n_{ray})}{M-1}. \tag{5.26}$$

The output ray amplitudes are scaled

$$E_{out}\left(n_{ray}\right)=\sqrt{\alpha}E_{out,norm}\left(n_{ray}\right), \tag{5.27}$$

where the scaling factor is

$$\alpha=\frac{\sum_{n_{tube}=1}^{N-1}P_{in}(n_{tube})}{\sum_{n_{tube}=1}^{N-1}P_{out,norm}(n_{tube})}. \tag{5.28}$$

The ray ring power, with the approximation of $\bar{r}\cdot\bar{n}\approx 1$, in (5.8) becomes:

$$P_{in}(n_{tube})\approx\frac{1}{2\eta}E_{ave}^{2}A=\frac{1}{2\eta}\frac{E_{in}^{2}(n_{ray}+1)+E_{in}^{2}(n_{ray})}{2}\left(\pi\rho_{n+1}^{2}-\pi\rho_{n}^{2}\right), \tag{5.29}$$

where ρ_n and ρ_{n+1} are the input ray ring coordinates at the input aperture for ray rings n_{ray} and n_{ray}+1, respectively. The total power in each ray ring is known from (5.29). The new output field aperture coordinates are calculated so that the power is equal for each ray ring, i.e.,

$$P_{in}(n_{tube})=P_{out}(n_{tube}). \tag{5.30}$$

The output field $E_{out}(n_{ray})$ is known in a constant $\Delta\rho'$ grid (or some other user defined grid). The power density is approximated to be a linear function between the known points, i.e., when $\rho'_n \leq \rho' \leq \rho'_{n+1}$

$$E_{out}^{2}(\rho')=k(n_{tube})\rho'+b(n_{tube}), \tag{5.31}$$

where $k(n_{tube})$ and $b(n_{tube})$ are calculated from $E_{out}(n_{ray})$ and $E_{out}(n_{ray}+1)$

$$k(n_{tube}) = \frac{E_{out}^2\left(n_{ray}+1\right) - E_{out}^2\left(n_{ray}\right)}{\rho'_{n+1} - \rho'_n} \tag{5.32}$$

$$b(n_{tube}) = E_{out}^2\left(n_{ray}\right). \tag{5.33}$$

The new output aperture coordinates ρ' are calculated, starting from the centre of output field aperture, by solving ρ'_{n+1} from

$$P_{in}(n_{tube}) = P_{out}(n_{tube}) = \frac{1}{2\eta}\int_{\rho'_n}^{\rho'_{n+1}} E_{out}^2(\rho')2\pi\rho' d\rho', \tag{5.34}$$

where $E_{out}^2(\rho')$ is a piece-wise continuous function calculated using (5.31).

The incident angles of the rays to the aperture planes, i.e., $\bar{r}\cdot\bar{n}$, could be taken into account in the mapping by replacing E^2 with $E^2\,\bar{r}\cdot\bar{n}$ in (5.28)–(5.34).

5.3.3 Synthesis of the surfaces

The shaped surfaces are synthesised from the known input and output rays and from the geometry of the feed system by tracing the rays, using Snell's law for reflections (or refraction) and ray length adjustment. The surfaces are assumed locally planar. The synthesis procedure is similar for both dual reflector and lens feed systems as both have two shaped surfaces. The synthesis is explained for a general offset geometry. Rotational symmetry in case of lens feed systems in Chapter 7 simplifies the synthesis as only one radial cut is necessary to synthesise.

The known information in the beginning of the synthesis is illustrated in Figure 5.7. The centre ray is known from the basic geometry. The centre ray interception points on the surfaces are the first known points. Synthesis starts from the centre ray and progresses ring by ring in counter-clock wise direction to the aperture rim. After the centre ray the synthesis procedure is the same for each ray. The synthesis procedure is described in Figure 5.9.

The 1st shaped surface is directly illuminated by the feed horn and it is mainly responsible for modifying the amplitude. The 2nd shaped surface is used to correct the phase.

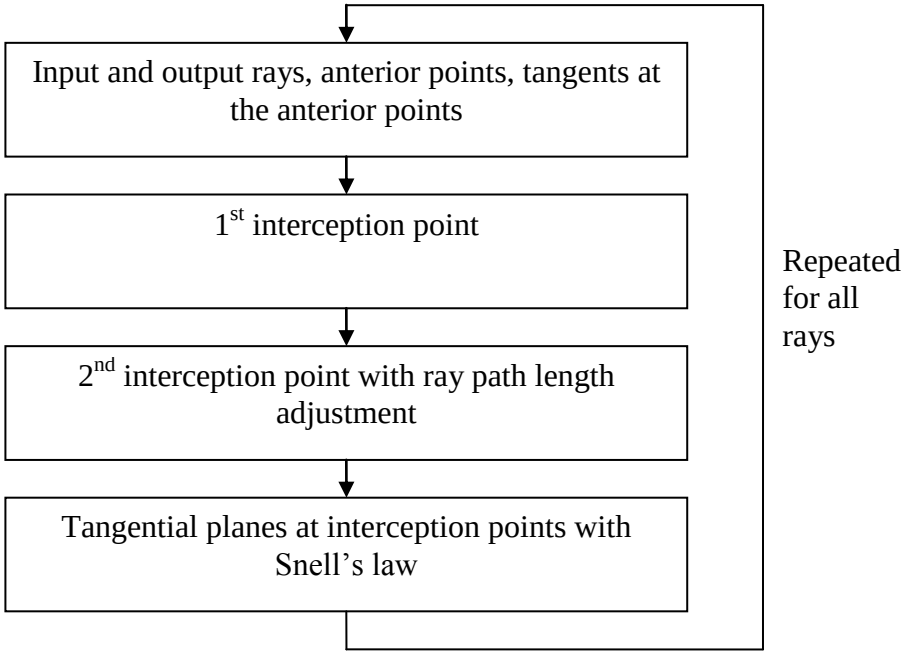

Figure 5.9: Synthesis procedure.

First the tangential planes at the centre ray interception points are calculated using Snell's law

$$\bar{n} = \frac{\bar{r}_r - \bar{r}_i}{\left|\bar{r}_r - \bar{r}_i\right|}, \tag{5.35}$$

where $\bar{n}$ is the surface normal vector, $\bar{r}_i$ is the directional vector of the incident ray and $\bar{r}_r$ is the directional vector of the reflected ray.

After the centre ray the synthesis procedure is the same for each ray. For a ray (n_{ray}, m_{ray}) the input and output rays, the anterior points (n_{ray}–1, m_{ray}) and the horizontal and vertical tangents at the anterior points are known. Calculation of the next point of a surface is illustrated in Figure 5.10.

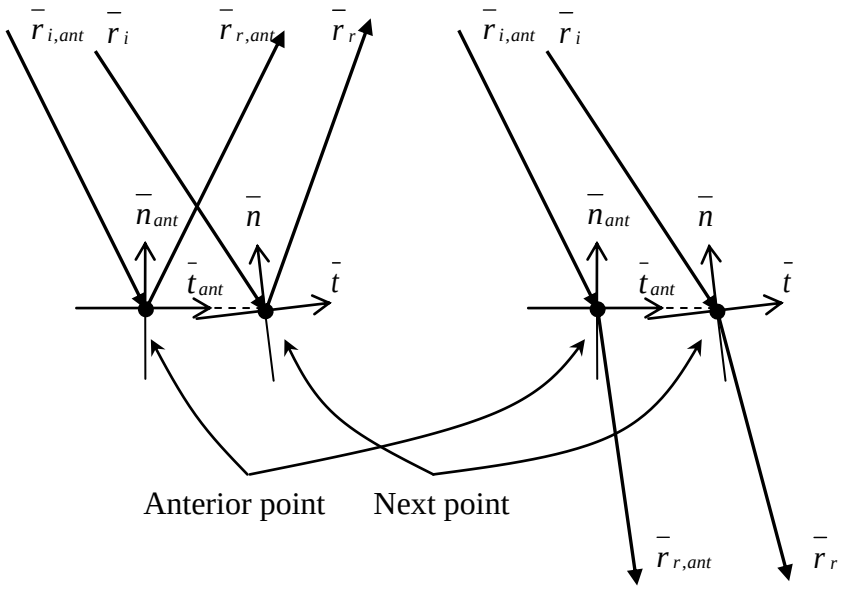

Figure 5.10: Calculation of the next point of the surface: a) reflection, b) refraction.

The 1st surface point (n_{ray}, m_{ray}) is the interception point of the input ray (n_{ray}, m_{ray}) and the tangential plane at the anterior point, i.e., at the point (n_{ray}–1, m_{ray}).

The 2nd surface point (n_{ray}, m_{ray}) is calculated in a similar way as the interception point of the output ray (n_{ray}, m_{ray}) and the tangential plane at the anterior point, i.e., point (n_{ray}–1, m_{ray}) of the 2nd surface. The 2nd surface point is then moved along the output ray to adjust the total length of the ray $l(n_{ray}, m_{ray})$ from the feed horn phase centre point to the output field aperture. The desired ray length is

$$l(n_{ray}, m_{ray}) = \sqrt{\rho'(n_{ray}, m_{ray})^2 + f_{holo}^2} - \frac{\lambda_0}{2\pi}\Psi_{in}(n_{ray}, m_{ray}) - \frac{\lambda_0}{2\pi}\Psi_{out}(n_{ray}, m_{ray}) + C, \tag{5.36}$$

where f_{holo} is the hologram focal length, Ψ_{in} is the feed horn phase pattern, Ψ_{out} is the desired output field phase, and C is a constant. The desired ray length is known for the centre ray from the geometry, therefore the constant C can be solved from (5.36) written for the centre ray. In case of a shaped lens feed system the desired ray length is an electrical ray length taking into account the electrical properties of the lens.

After the surface points are known, the horizontal and vertical tangents are calculated from the input ray, the ray from the 1st surface point to the 2nd surface point and the output ray using the Snell's law as explained in Section 5.1.8.

After the synthesis the shaped surfaces are fitted to planes with rounded sections. The rounding is needed to reduce edge diffraction. Also, the planar sections around the shaped surfaces facilitate the mechanical construction of the feed system.

5.4 Simulations

The design procedure, as explained in Section 5.2, is based on iterative optimisation of the synthesis parameters based on simulation results. The simulation method depends on the feed system type. The dual reflector feed systems are simulated with GRASP8W, as described in Section 5.4.1. A ray-tracing method is used to simulate the shaped lens feed systems. This ray-tracing method is described in Section 5.4.2.

5.4.1 Simulations with GRASP8W

GRASP8W is used to simulate the dual reflector feed systems [13], [16]. In GRASP8W physical optics (PO) is used to calculate the field radiated by a reflector antenna. Physical theory of diffraction (PTD) can be used to include diffracted fields from the reflector edges.

Simulated feed horn radiation pattern and data of the feed system geometry and shape of the reflectors are needed for the simulation. First, surface currents on the subreflector (1^{st} surface) are calculated from the feed horn radiation pattern. Then the surface currents on the main reflector (2^{nd} surface) are integrated from the currents on the subreflector. Finally the field illuminating the hologram is calculated from the current elements on the main reflector. Amplitude, phase and cross-polarisation level can be calculated from the field data given by the GRASP8W software.

5.4.2 Ray-tracing simulation

A ray-tracing method is used to simulate the shaped lens feed systems. The method is based on calculating the aperture field by ray-tracing through the lens (or lenses). The ray-tracing is based on the same principles and approximations as the synthesis in Section 5.3. The hologram illumination is integrated from the aperture field with Huygens' principle. Ray definition and ray-tracing is explained in Section 5.4.2.1, aperture field calculation in Section 5.4.2.2, and calculation of the hologram illumination in Section 5.4.2.3.

The shaped lens feed systems are rotationally symmetric and therefore also the ray-tracing simulation is rotationally symmetric. The rotational symmetry means that it is necessary to find the ray paths for only one radial cut. After the ray paths have been found ray tube powers and transmission coefficients can be calculated for both vertical and horizontal cuts. The two-dimensional hologram illumination field is integrated from the two-dimensional aperture field, i.e., without the rotational symmetry assumption.

5.4.2.1 Ray definition and ray tracing to the aperture

Rays are set to originate from the feed horn focal point. Number of rays and the input beam half-beam width θ_{feed} are, in general, different than in the synthesis. The ray path is calculated from the feed horn focal point to the aperture plane that is a plane perpendicular to the symmetry axis immediately after the lens (or after lenses).

The geometry and the lens surfaces are known from the synthesis. The surfaces include the shaped surfaces and the rounded edge regions. The shaped surfaces are defined by the

interception points of input and output rays and the tangential planes of the anterior points in the synthesis. In the simulation the surfaces are approximated with planar sections between the known points from the synthesis.

Calculation of the ray path is identical for each surface of the lens (or lenses). The geometry involved in calculating the refracted ray is illustrated in Figure 5.11. The incident ray is known, it is either a ray originating from the feed horn focal point or a refracted ray from a previous surface. First the interception point of the incoming ray and the surface is calculated. The refraction angle θ_2 is calculated from the incident angle θ_1 and from the electrical properties (ε_1 and ε_2) using Snell's law (5.9). The refracted ray can be calculated from the refraction angle θ_2.

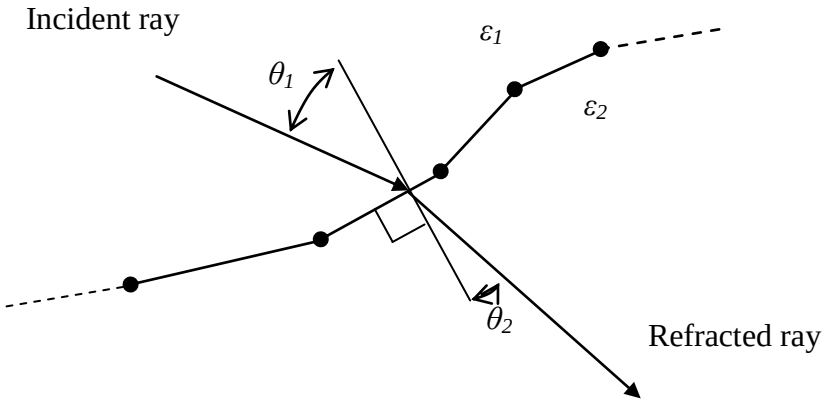

Figure 5.11: Calculation of refracted ray.

An example of ray-tracing through two shaped lenses is shown in Figure 7.7 on page 85. In Figure 7.7, the feed horn focal point is at z = 295 mm and the aperture plane at z = 0 mm.

The final result of the ray-tracing for each ray n = 1 ... N includes: ray end point at the aperture ρ'_n , incident angles θ_1 for each surface, and total electrical ray length $l_{el,tot}(n)$. The θ_1 angles are used to calculate the transmission coefficients. The electrical ray length is

$$l_{el} = \sqrt{\varepsilon_r}\, l, \tag{5.37}$$

i.e., the electrical ray length is $\sqrt{\varepsilon_r}$ times longer than the geometrical ray length inside a lens. Total electrical ray length is the sum of ray lengths from the feed horn focal point to the aperture.

5.4.2.2 Calculation of the aperture field

The ray tube powers $P_{in}(n_{tube})$ are calculated using (5.29) as in the synthesis, except that now the rays and input aperture plane are the ones used in the ray-tracing simulation. The vertical polarisation, i.e., the main polarisation, of the radiation pattern of the feed horn is used in the ray tube power calculations.

In the aperture plane the ray tube ring n_{tube} is between rays n_{ray} and n_{ray}+1, i.e., between ray end points ρ'_n and ρ'_{n+1}. The aperture field amplitude is calculated from the ray tube powers. Instead, the ray lengths and transmission coefficients are determined at the ray end points. Therefore, the aperture field is first calculated at points

$$\rho'(n_{tube}) = \frac{1}{2}(\rho'_n + \rho'_{n+1}). \tag{5.38}$$

Total electrical ray lengths are

$$l_{el,tot}(n_{tube}) = \frac{1}{2}\left(l_{el,tot}(n_{ray}) + l_{el,tot}(n_{ray}+1)\right). \tag{5.39}$$

Transmission coefficients are calculated with (5.11) and (5.13). The total transmission coefficient at $\rho'(n_{tube})$ is

$$T(n_{tube}) = \frac{1}{2}\left(\prod_{i=1}^{N_{surf}} \tau_i(n_{ray}) + \prod_{i=1}^{N_{surf}} \tau_i(n_{ray}+1)\right), \tag{5.40}$$

where N_{surf} is the number of surfaces, and $\tau_i(n_{ray})$ is the transmission coefficient of i^{th} surface for ray n_{ray}.

The tube power at the aperture is

$$P_a(n_{tube}) = T(n_{tube})^2 P_{in}(n_{tube}). \tag{5.41}$$

The field amplitude at points $\rho'(n_{tube})$ is calculated from the tube powers at the aperture. Using the expression for the tube power in (5.8) the tube power at the aperture is

$$P_a(n_{tube}) = \frac{1}{2\eta_0} E_a(n_{tube})^2 A_a(n_{tube}), \tag{5.42}$$

where $A_a(n_{tube})$ is the ray ring area in the aperture:

$$A_a(n_{tube}) = \left(\pi\rho'^2_{n+1} - \pi\rho'^2_n\right). \tag{5.43}$$

The field amplitude at points $\rho'(n_{tube})$ is

$$|E_a(n_{tube})| = T(n_{tube})\sqrt{\frac{P_{in}(n_{tube})\cdot 2\eta_0}{A_a(n_{tube})}} = |E_{in}(n_{tube})|\cdot T(n_{tube})\sqrt{\frac{A_{in}(n_{tube})}{A_a(n_{tube})}}. \tag{5.44}$$

The aperture field phase is calculated from the electrical ray lengths, therefore aperture field is

$$E_a(n_{tube}) = |E_a(n_{tube})| e^{-jk_0 l_{el,tot}(n_{tube})}. \tag{5.45}$$

The radiation pattern of the feed horn is different for vertical and horizontal cuts. Also, the transmission coefficients depend on the polarisation. The vertical and horizontal cuts

of the ray amplitudes in the aperture $E_{ver}(n_{tube})$ and $E_{hor}(n_{tube})$ are calculated from (5.45); $E_{ver}(n_{tube})$ with $\tau_{||}$ (5.11) and vertical cut of P_{in}, and $E_{hor}(n_{tube})$ with $\tau_{\perp}$ (5.13) and horizontal cut of P_{in}.

The final two-dimensional aperture field $E_a(\rho',\phi')$ is calculated at constant angular and radial polar grid, i.e., a grid with constant $\Delta\phi'$ and constant $\Delta\rho'$.

$$\overline{E}_a(a,b) = E_a(\rho'_a,\phi'_b)\overline{u}_y, \quad \begin{cases} \rho'_a = (a-½)\Delta\rho', & a = 1,2,3,..A \\ \phi'_b = (b-½)\Delta\phi', & b = 1,2,3,..B \end{cases}. \tag{5.46}$$

In (5.46), the aperture field points are defined so that $\rho'_A = \rho'_{\max} - ½\Delta\rho'$ and $\phi'_B = 2\pi - ½\Delta\rho'$. $\rho'_{\max}$ defines the size of the aperture.

Vertical and horizontal cuts of $E_a(\rho'_a,\phi'_b)$, i.e., $E_{ver}(\rho'_a)$ and $E_{hor}(\rho'_a)$, are interpolated from $E_{ver}(n_{tube})$ and $E_{hor}(n_{tube})$. The aperture field between the field cuts is interpolated as:

$$E_a(\rho'_a,\phi'_b) = \sin^2(\phi'_b)E_{ver}(\rho'_a) + \cos^2(\phi'_b)E_{hor}(\rho'_a). \tag{5.47}$$

5.4.2.3 Calculation of hologram illumination with Huygens' principle

The field at the hologram is calculated from the aperture field with Huygens' principle as explained in Section 3.1. Let's first define the aperture field and the hologram illumination field.

Aperture field is $\overline{E}_a(n,m) = E_a(\rho'_n,\phi'_m)\overline{u}_y$ from (5.46). The aperture field is defined at $z' = z_a$, i.e., at the aperture plane. The polarisation of the aperture field is linear vertical polarisation. The hologram illumination field is: (at $z = 0$)

$$\overline{E}_h(k,l) = E_h(\rho_k,\phi_l)\overline{u}_y, \quad \begin{cases} \rho_k = k\Delta\rho, & k = 1,2,3,..K \\ \phi_l = l\Delta\phi, & l = 1,2,3,..L \end{cases}. \tag{5.48}$$

From (3.9), the vertical polarisation of the hologram illumination is:

$$\overline{E}_h(k,l) = \sum_{b=1}^{B}\sum_{a=1}^{A}\overline{F}(a,b,k,l)dA(a,b), \tag{5.49}$$

where

$$\overline{F}(a,b,k,l) = \frac{E_a(a,b)e^{-jkR(a,b,k,l)}}{2\pi}\left(\frac{jk}{R(a,b,k,l)^2} + \frac{1}{R(a,b,k,l)^3}\right)(z_a)\overline{u}_y \tag{5.50}$$

$$R(a,b,k,l) = \left|\overline{r}(k,l) - \overline{r}'(a,b)\right| = \left|(\rho_k - \rho'_a)\overline{u}_\rho + (\phi_l - \phi'_b)\overline{u}_\phi + z_a\overline{u}_z\right| \tag{5.51}$$

$$dA(a,b) = \frac{\Delta\phi'}{2\pi}\left(\pi(\rho'_a + ½\Delta\rho')^2 - \pi(\rho'_a - ½\Delta\rho')^2\right). \tag{5.52}$$

Equation (5.49) gives the hologram illumination accurately only if the number of aperture field points is high enough. The required number of aperture field points can be tested by increasing the number of points and testing the convergence of the resulting hologram illumination.

In (5.49) the closed integral from (3.9) is replaced with a finite sum. This means that the aperture field is assumed to be zero outside the area where the aperture field has been calculated. In practice absorbers are used to limit the aperture size.

6 Dual reflector feed systems

Two dual reflector feed systems (DRFSs) for compact antenna test ranges (CATRs) based on a hologram have been designed, manufactured, and tested. The synthesis method in Chapter 5 was first developed and used to design a 310 GHz DRFS [13], [14]. The 310 GHz DRFS is briefly presented in Section 6.1. Later, a 650 GHz DRFS was designed as part of an ESA project aiming at measurement of a 1.5 m antenna at 650 GHz during autumn 2006 [12]. Design of the 650 GHz DRFS is presented in Section 6.2.

The design of a DRFS always starts from the definition of basic geometry, and the input and output fields, for the synthesis. The chosen basic geometry of both of the DRFSs is illustrated in Figure 6.1. The figure is not in scale. This basic geometry allows a diverging beam with a reasonably compact structure [13]. Based on the location of the focal points, the geometry can be called dual shaped hyperboloid geometry. The first reflector is called subreflector and the second main reflector.

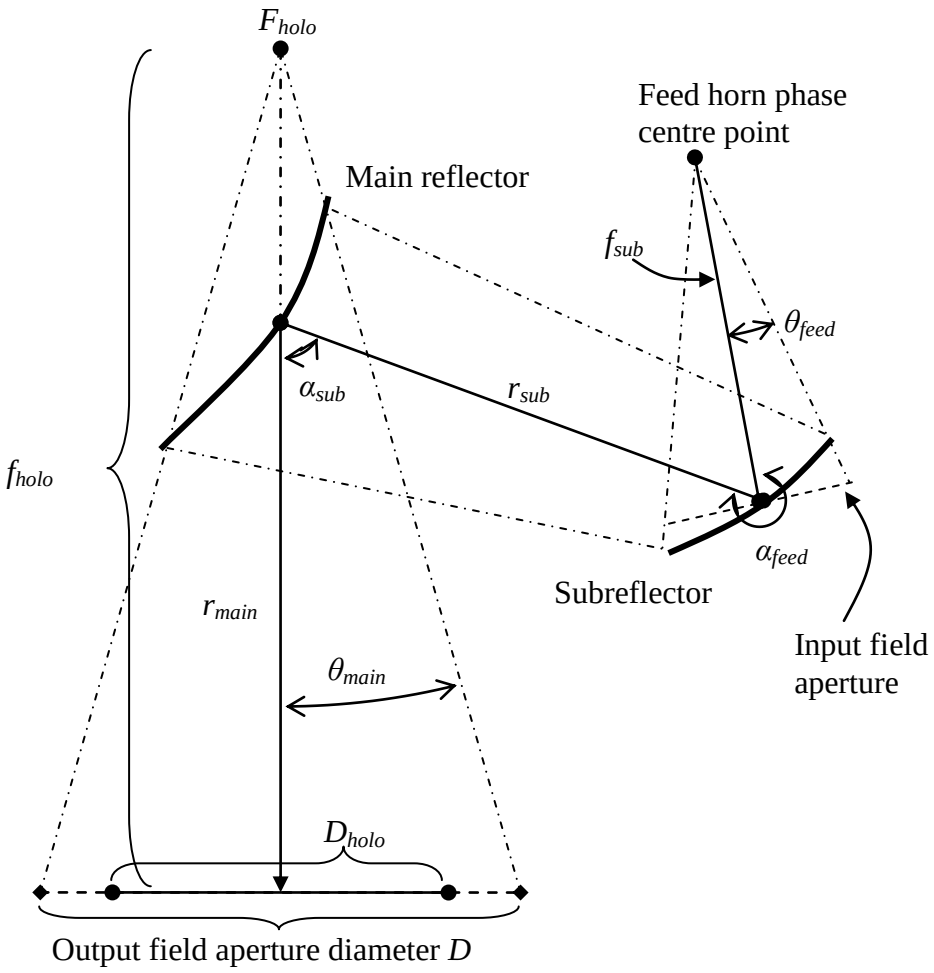

Figure 6.1: Basic geometry of a DRFS. Figure is not in scale.

The solid line in Figure 6.1 is the centre ray path. The feed horn location is defined by the feed horn phase centre point. The feed angle is α_{feed}. The focal length of the subreflector f_{sub} is the distance between the feed horn phase centre point and the centre point of the subreflector. The subreflector offset angle is α_{sub} and the distance between the reflectors is r_{sub}. The focal point of the hologram is F_{holo} and that is also the focal point of the feed system. The diameter of the hologram is D_{holo}. The focal length of the system is f_{holo} and the distance from main reflector to the hologram centre point is r_{main}.

For the synthesis of the shaped surfaces, the input and output fields are defined at the aperture planes illustrated in Figure 6.1. Input field is defined at the input field aperture from the far-field pattern of the feed horn. Input half-beam width, i.e., the feed half-beam width, is θ_{feed}. The output field for the synthesis is defined at the output field aperture. The output half-beam width is θ_{main}. The output field aperture diameter is in general larger than the hologram diameter.

6.1 A 310 GHz DRFS

Previously, a 310 GHz dual reflector feed system for a hologram-based compact antenna test range has been designed. This DRFS was designed with a numerical synthesis method and optimised to illuminate a 600 mm hologram at 310 GHz [13], [14].

The feed horn used is a corrugated horn with Gaussian beam. The –17.5 dB half-beam width of the 310 GHz horn is about 20º. The desired output field was a Butterworth-type function in (5.22), where ρ_c is 210 mm and N is 5. The geometrical parameters are listed in Table 6.1.

Table 6.1: Geometrical parameters for the 310 GHz DRFS [13].

D	700 mm
D_{holo}	600 mm
f_{holo}	1800 mm
f_{sub}	100 mm
r_{sub}	150 mm
r_{main}	1550 mm
α_{feed}	270º
α_{main}	90º
θ_{feed}	20º
θ_{main}	11º

Edge illumination was chosen to be less than –15 dB for both reflectors [14] and below –15 dB for the hologram [13]. 423 × 401 rays were used in the synthesis. The dimensions of the concave subreflector are approximately 122 mm × 83 mm × 4.6 mm and dimensions of the convex main reflector 165 mm × 119 mm × 2.8 mm. The DRFS was manufactured at Thomas Keating Engineering Physics, Ltd., in England. Horizontal

cross-cuts the shaped reflector surfaces are shown in Figure 6.2. Accuracy of the synthesis and assemble tolerances are studied with simulations in [13].

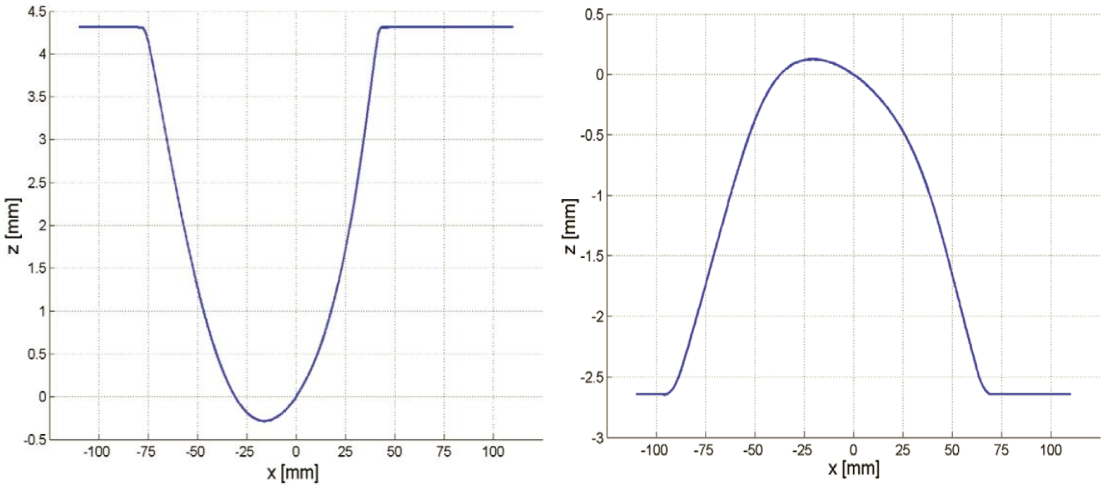

Figure 6.2: Horizontal cross-cuts of the subreflector (left-hand-side) and of the main reflector (right-hand-side) [13].

Simulated and measured hologram illumination of the 310 GHz dual reflector feed system is presented in [13]. The simulations were done with GRASP8W software [84] using physical optics (PO) and physical theory of diffraction (PTD). The field radiated by the DRFS at 310 GHz was measured with planar near-field probing [13]. The measurements were done with millimetre wave vector network analyser AB Millimétre MVNA-8-350. The desired, simulated and measured horizontal and vertical beam-cuts are shown in Figure 6.3 and Figure 6.4, respectively.

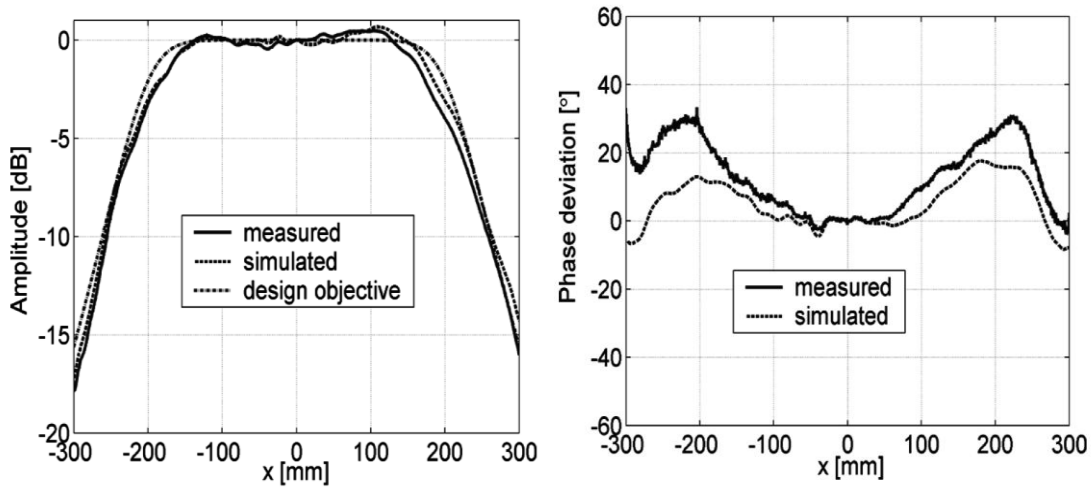

Figure 6.3: Measured and simulated amplitude and phase deviation from the spherical wave in a horizontal beam cross-cut at 310 GHz [14].

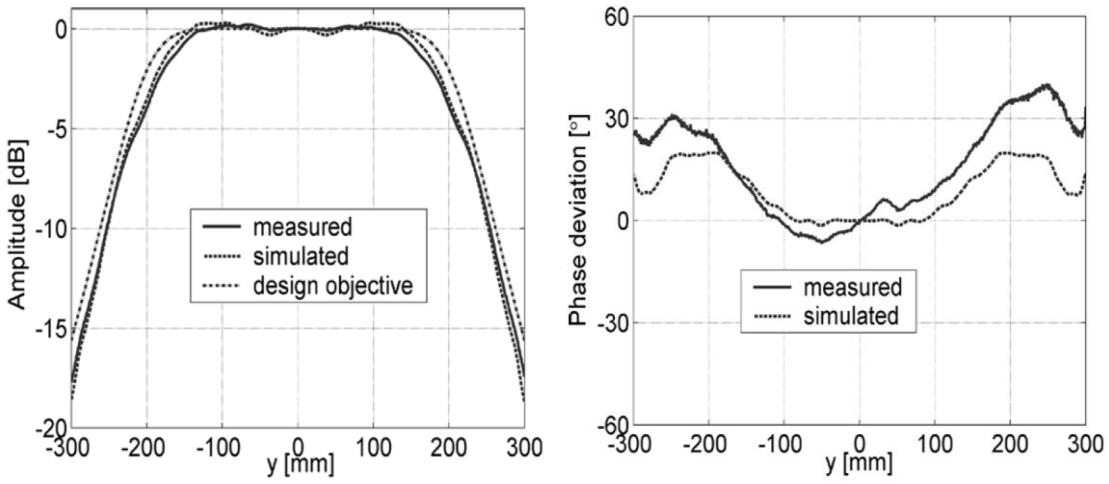

Figure 6.4: Measured and simulated amplitude and phase deviation from the spherical wave in a vertical beam cross-cut at 310 GHz [14].

The measured amplitude is within ±0.3 dB from the simulated amplitude in the beam cross-cuts in the central region [13]. The measured phase is within 30° from the ideal spherical phase within the radius of 150 mm from the centre of the beam. The phase deviation can be mostly compensated by placing the DRFS about 12 millimetres closer to the hologram. Measured cross-polarisation level is at maximum about –23 dB.

The 310 GHz DRFS was tested with a demonstration hologram [13]. For comparison, a hologram illuminated with a Gaussian beam was designed and tested. The main advantages of using a DRFS were found to be improved manufacturability of the hologram and the operation of the hologram also at the horizontal polarisation [13]. Conservatively chosen beam width of the DRFS was limiting the size of the quiet zone.

6.2 Design of a 650 GHz DRFS

The design of the 650 GHz DRFS is described in this chapter. The 650 GHz DRFS was designed as a part of an ESA project aiming at the measurement of a 1.5 m antenna in a hologram-based CATR at 650 GHz [12]. The design goals and limitations set before starting the designing were:

- Optimised for a 3.18 metre diameter hologram with $f_{holo}/D_{holo} = 4$.
- Optimised for vertical linear polarisation at 650 GHz.
- –1 dB beam width corresponding to a 2 metre diameter of QZ, i.e., –1 dB beam width radius of 1190 mm in the hologram illumination.
- Hologram edge illumination under –10 dB.
- The amplitude ripple should be less than 0.7 dB peak-to-peak and the deviation from a spherical phase originating from the hologram focal point F_{holo} should be less than 7° peak-to-peak.

- The maximum diameter of the reflectors about 200 mm. Also the size of the whole feed system structure should be kept moderate.
- Corrugated feed horn with a Gaussian beam and the –30 dB half-beam width about 25°.

The design procedure is described in Section 5.2 and the synthesis of the shaped surfaces in Section 5.3. The design procedure is an iterative optimisation of the parameters based on simulation results. The simulations of the dual reflector feed systems are done with GRASP8W using physical optics (PO) and physical theory of diffraction (PTD), as described in Section 5.4.1. Measurement results of the 650 GHz DRFS are presented in Section 8.2.

6.2.1 Basic geometry

The basic geometry parameters of the designed 650 GHz DRFS are listed in Table 6.2. The geometry is illustrated in Figure 6.1. The f_{holo}/D_{holo} ratio is 4. f_{holo} and D_{holo} are predetermined from the layout of the CATR, in Figure 2.9, and the output field aperture diameter D is defined by f_{holo} and θ_{main}. The other seven parameters (f_{sub}, r_{sub}, r_{main}, α_{feed}, α_{main}, θ_{feed}, and θ_{main}) in Table 6.2 define the basic geometry of a DRFS and are optimised.

Table 6.2: Geometrical parameters of the 650 GHz DRFS.

D	5.883 m
D_{holo}	3.180 m
f_{holo}	12.720 m
f_{sub}	112 mm
r_{sub}	200 mm
r_{main}	12.408 m
α_{feed}	280º
α_{main}	80º
θ_{feed}	24º
θ_{main}	13º

The reflector sizes are mainly determined by the basic geometry. The subreflector size is determined by f_{sub}, θ_{feed} and α_{feed} and the main reflector size is determined by r_{main}, θ_{main} and α_{sub}. Also the choice of the input and output fields affect the sizes of the reflectors. It was discovered that the size of the reflectors should be as large as possible to facilitate the shaping and enable lower edge illumination of the reflectors.

The reflector angles α_{feed} and α_{sub} are 80° and 280° (instead of 90° and 270° in the 310 GHz DRFS) to keep the structure compact and reflector size reasonable even though f_{sub} and r_{sub} are increased. This also decreases the maximum cross-polarisation level by about 1.5 dB according to the simulations.

The basic geometry parameters, together with the input and output field patterns, are used to choose the reflector edge illuminations. The edge illuminations need to be minimised to reduce ripples caused by edge diffraction.

6.2.2 Input and output fields and rays

Input and output fields are defined before the synthesis of the shaped surfaces. The input field is defined at the input field aperture plane. The output field is defined at the output field aperture plane. These aperture planes are illustrated in Figure 6.1. The input and output rays are calculated from the field distributions.

The input field is calculated from the simulated radiation pattern of the feed horn. The radiation pattern used in designing the 650 DRFS is shown in Figure 4.10 on page 41. The feed horn has a Gaussian beam and the -30 dB half-beam width is about 25°. Amplitude level at the edge of the input field aperture plane defines the subreflector edge illumination. Input half-beam width θ_{feed} is chosen to achieve low edge illumination.

The output field is optimised to achieve the desired hologram illumination field to the output of the feed system. A Butterworth-type function (5.22) is used for the amplitude patterns in the area corresponding to the hologram area. A Butterworth-type function with $\rho_c \approx 1355$ mm and $N = 10.7$ was used in the final design of the 650 GHz DRFS. Also the amplitude pattern corresponding to the area outside of the hologram area needs to be optimised. The field pattern towards the edge of the output field aperture determines the main reflector edge illumination and also has a large effect on the shape and size of the main reflector.

The desired output field beam has to be chosen to be wider and the hologram edge illumination of the output field to be lower than for the desired hologram illumination. The difference between the output field defined for the synthesis and the simulated output aperture field is larger if a wider beam is attempted and smaller if a narrower beam is attempted. Also ripples in the simulated output field are larger with wider output field beam. Also, the ratio of the input and output field beam widths (and shapes) has to be right. For a given input beam width there is an optimum output beam width.

The final optimised input and output field normalised amplitude patterns at the field aperture planes are shown in Figure 6.5.

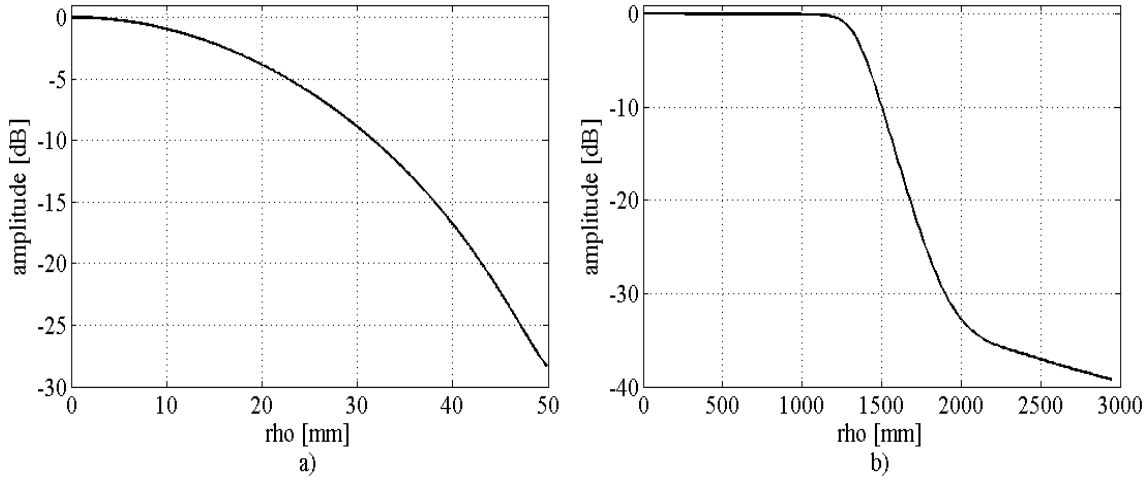

Figure 6.5: Input and output fields used in the synthesis of the 650 GHz DRFS: a) input field amplitude in the input field aperture, and b) output field amplitude in the output field aperture.

The input and output field phase patterns need to be defined for the synthesis. The phase patterns affect the desired total ray length in (5.36). For simplicity, the feed horn phase pattern, shown in Figure 4.10, is not taken into account in the synthesis. In the simulations the feed horn phase pattern is taken into account.

In the 650 GHz DRFS the output field phase pattern, shown in Figure 6.6, was optimised. It was found that the shape of both the amplitude and the phase patterns of the DRFS can be modified by changing the output field phase pattern. The maximum of about –70° corresponds to 90 μm longer rays.

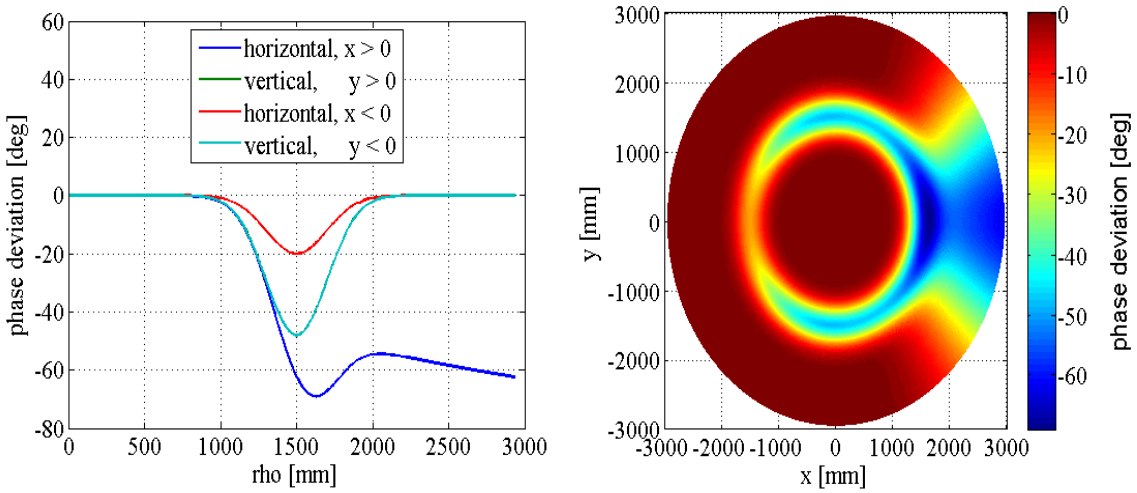

Figure 6.6: Phase deviation from the spherical wave of the output field phase in the output field aperture.

The input and output rays are calculated with rotationally symmetric aperture mapping, as described in Section 5.3.2.4. First the input rays are chosen then the output rays are calculated so the ray tube powers are same in the output as in the input. Only the

amplitude patterns affect the ray directions. Both input and output fields are assumed rotationally symmetric. 601 × 601 rays were used.

The ray grids define the points in the field aperture planes where the rays intersect these planes. For both the input and output, the ray grids are constant in angular direction, i.e., $\Delta\phi$ is constant. With 601 rays in angular direction $\Delta\phi = 0.6°$.

Ray spacing in the radial direction in the input and output ray grids is shown in Figure 6.7. The input ray grid was made denser towards the edge of the aperture plane in radial direction. With a constant $\Delta\rho$ the distance between the synthesised surface data points would be larger, which could lead to interpolation problems. The output ray grid coordinates in radial direction are calculated in the aperture mapping. With the maximum $\Delta\rho'$ of the output ray grid of about 47 mm, the maximum distance between the synthesized surface data points is only a few millimetres.

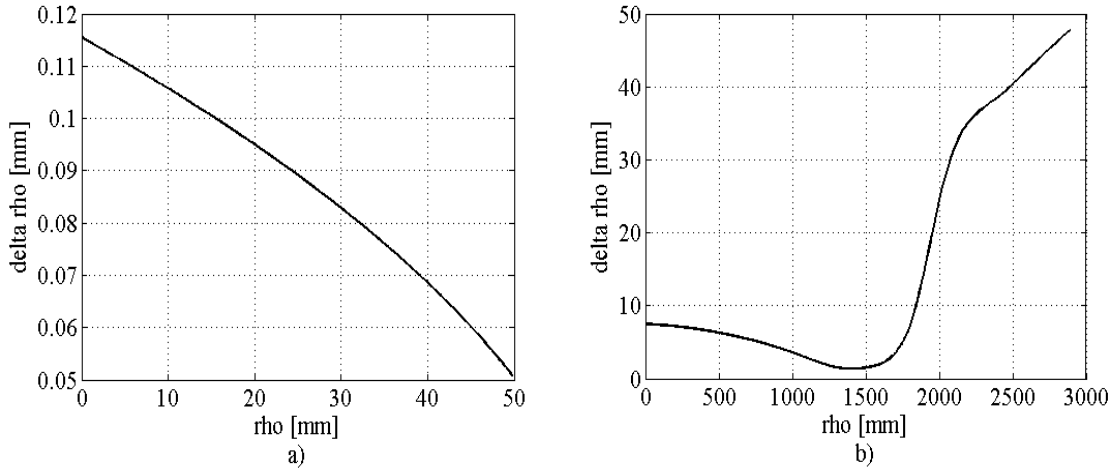

Figure 6.7: Ray spacing in the radial direction: a) $\Delta\rho$ of the input ray grid, and b) $\Delta\rho'$ of the output ray grid.

6.2.3 Synthesised reflector surfaces and mechanical design

The synthesis of the shaped surfaces is described in Section 5.3.3. The reflector surfaces are synthesised from the basic geometry, and the input and output rays. The reflector surface point is determined as the interception point of the input ray (or output ray) and the tangential plane at the anterior point (the closest known point in radial direction). The ray path length is adjusted to correspond to the desired spherical phase by moving the point of the main reflector.

Planes are fitted around the shaped surfaces. The manufacturing of the reflectors require the milling profile to be known. The fitting is done with a linear extrapolation and circular rounding illustrated in Figure 6.8. The linear extrapolation is needed because the rim of the shaped area is not exactly on a same plane. For the final design of the 650 GHz DRFS, a circular rounding of height $3\cdot\lambda/4$ in the subreflector and $\lambda/4$ in the main reflector was used.

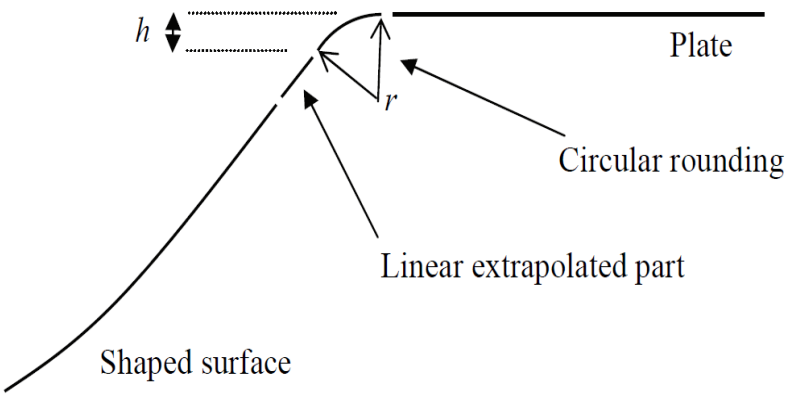

Figure 6.8: Reflector edge treatment.

Horizontal cuts of the reflector surfaces are shown in Figure 6.9. The dimensions of the reflectors of the designed 650 GHz DRFS are 146 mm × 109 mm × 7.0 mm (width × height × depth) for the concave subreflector and 203 mm × 160 mm × 4.4 mm for the convex main reflector.

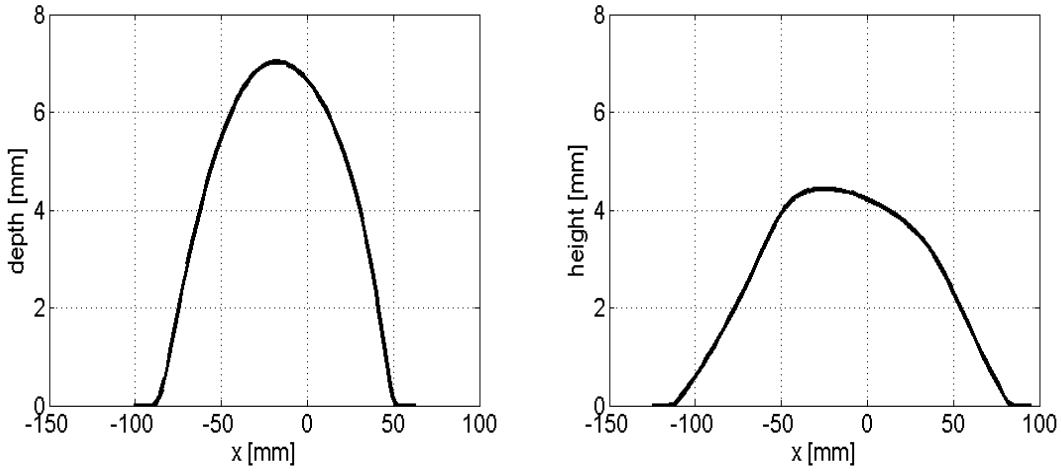

Figure 6.9: Horizontal cuts of the subreflector and the main reflector surfaces.

The 650 GHz DRFS was manufactured in England at Thomas Keating Engineering Physics, Ltd. The surface data of the reflectors for the manufacturing were defined in 99 × 99 points. The surface data for the milling machine are computed with meshing software, which generates NURBS (non-uniform rational B-spline) surfaces. The NURBS surfaces give a good fit to the given surface data despite the relatively small number of data points.

Figure 6.10 shows a 3-D model of the whole DRFS structure. The dimensions of the whole DRFS are approximately 400 mm × 210 mm × 270 mm, not including the 140 mm × 220 mm area reserved for the transmitter behind the feed horn. All the internal walls around the reflectors and the feed horn, the floor, and the ceiling inside the DRFS structure are coated with radar absorbing material (RAM). A photograph of the 650 GHz DRFS is shown in Figure 6.11.

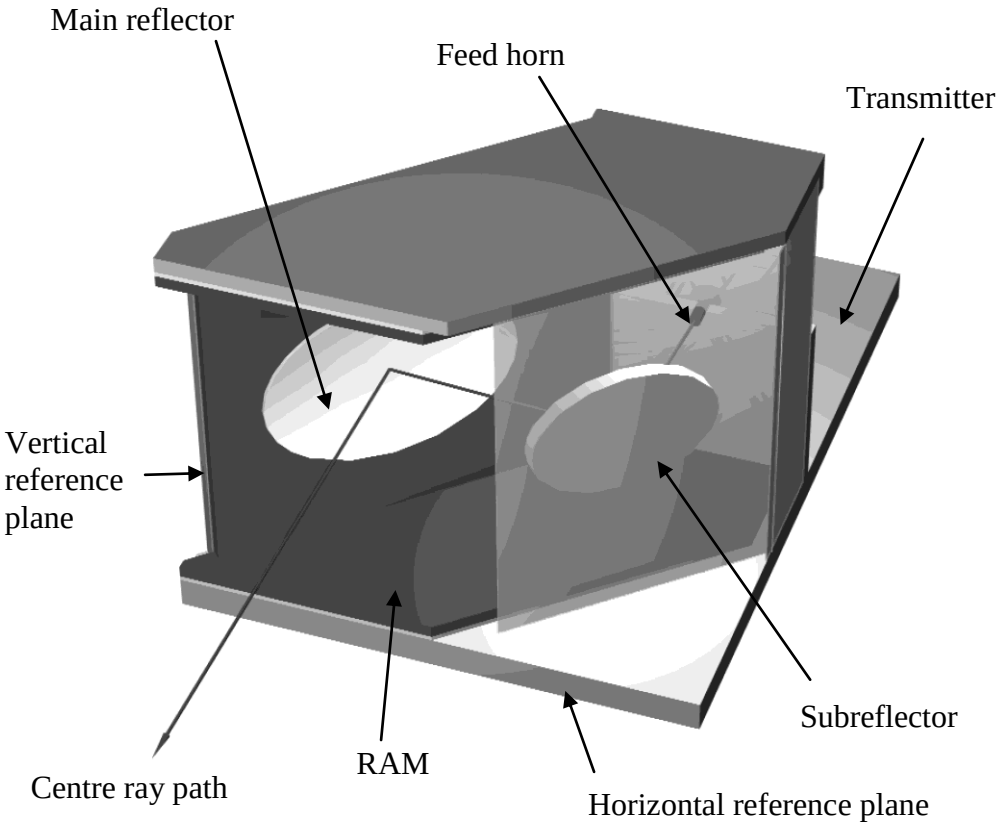

Figure 6.10: 3-D model of the DRFS structure.

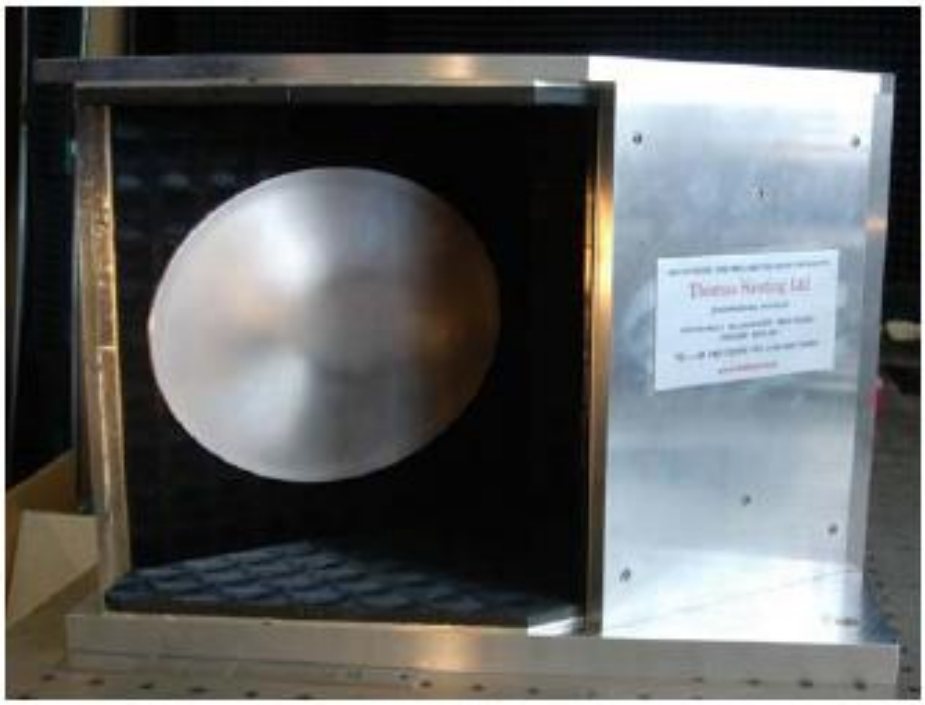

Figure 6.11: A photograph of the 650 GHz DRFS.

6.2.4 Simulation results

The simulations were done with GRASP8W software by Ticra Engineering Consultants [84] using physical optics (PO). Sometimes also physical theory of diffraction (PTD) was used. The effect of the PTD currents to the output aperture field was very small when the edge illuminations of the reflectors were small. The computation time of simulations with the PO currents was only a fraction of the time needed for simulations with both PO and PTD. Therefore, only PO was used during the optimisation. For the final results, both PO and PTD were used.

To ensure that sufficient number of current elements was used *PO Convergence*-object of the GRASP8W was used. The *PO Convergence*-object calculates the required number of current elements as the function of the desired field accuracy defined by the user [56].

The reflector surface data for the simulations was interpolated at a regular *xy*-grid, with $\Delta x = \Delta y = 0.5$ mm. Cubic interpolation is used in GRASP8W to calculate the surfaces at the points where the currents are calculated. Large number of points was used to ensure good accuracy of the surface points despite these two interpolations. Grid with $\Delta x = \Delta y =$ 0.5 mm was found to be dense enough.

The simulated amplitude and phase deviation of the 650 GHz DRFS are presented in Figure 6.12. The phase deviation is defined as a deviation from the phase pattern of a spherical wave originating from the hologram focal point F_{holo}. The –1 dB beam area of the simulated amplitude and phase deviation patterns are shown in Figure 6.13.

The –1 dB beam radius is about 1170 mm (74% of the hologram radius) and the hologram edge illumination is less than –10 dB. The beam width corresponds to a 1.96-metre diameter QZ. The amplitude ripple in the –1 dB beam area is 0.45 dB peak-to-peak and the phase deviation is 5° peak-to-peak. Based on simulations, the phase deviation in Figure 6.12 can be mostly compensated by moving the whole feed system 2 mm closer to the hologram. The simulated hologram illumination meets the requirements set for the 650 GHz DRFS.

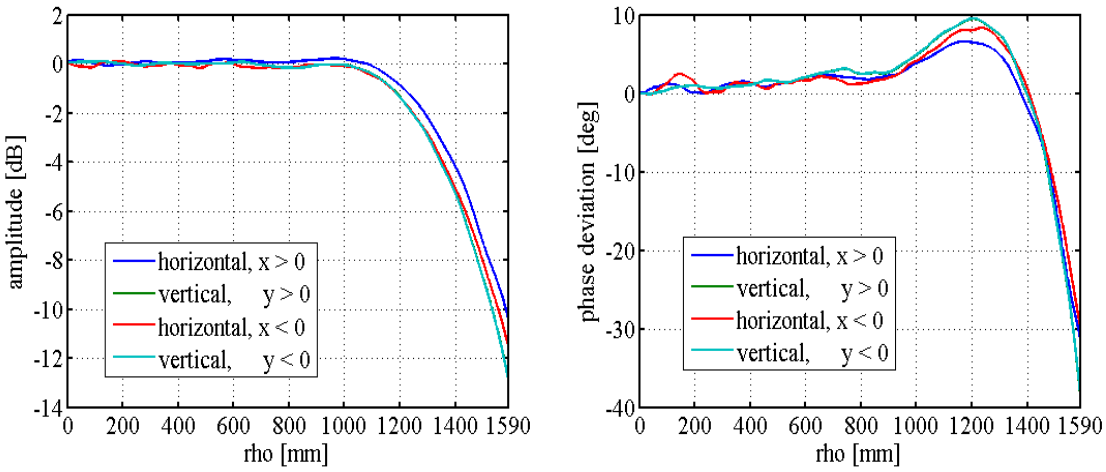

Figure 6.12: Simulated amplitude and phase deviation of the 650 GHz DRFS at the linear vertical polarisation.

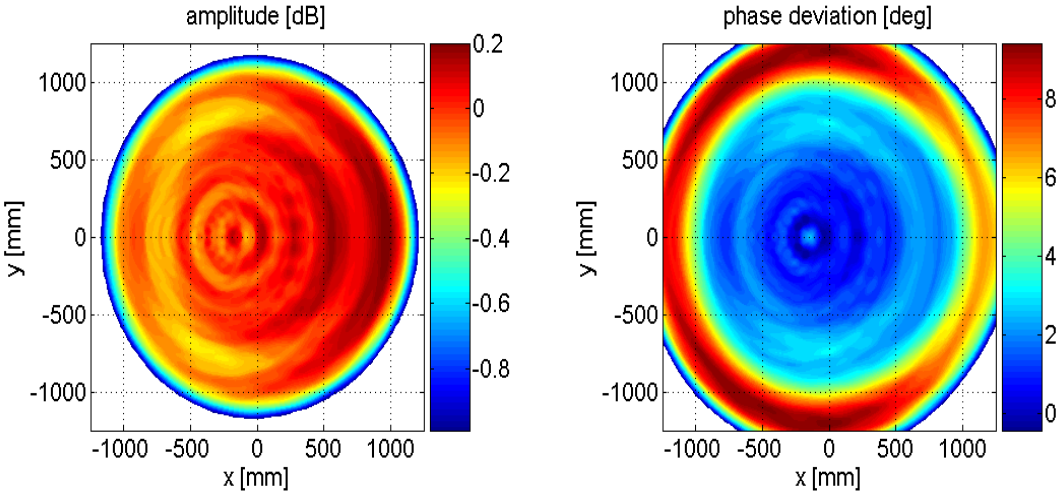

Figure 6.13: Simulated amplitude and phase deviations in the –1 dB beam area.

Simulated cross-polarisation level is at maximum about –20 dB below main polarisation maximum. The simulated cross-polarisation level and phase is presented in Figure 6.14. The cross-polarisation is the linear horizontal polarisation.

The cross-polarisation level of the feed horn is very small. The cross-polarisation in the hologram illumination is caused by depolarisation caused by the offset structure and the shaped surfaces of the reflectors. Cross-polarisation is not taken into account in the synthesis. There was not any specific design goal set for the cross-polarisation level.

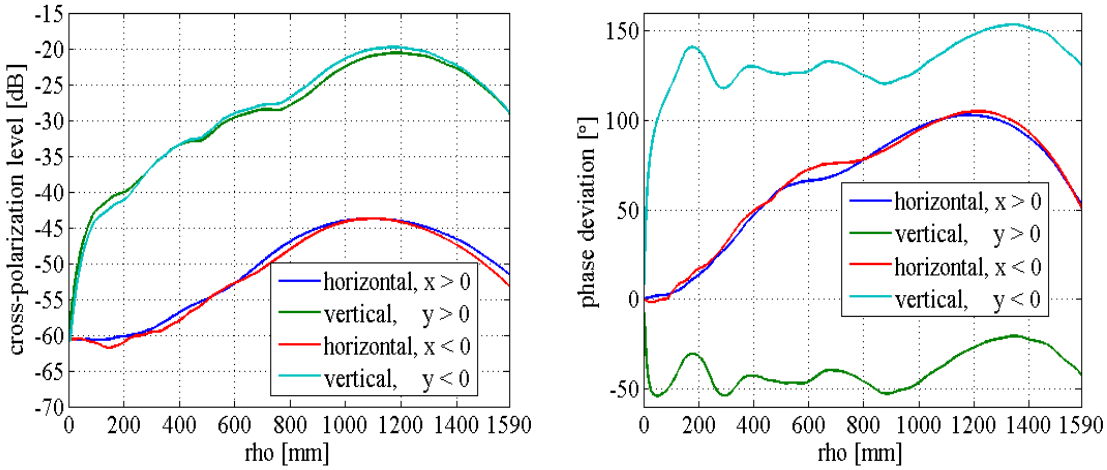

Figure 6.14: Simulated cross-polarisation and phase deviation of the 650 GHz DRFS.

6.2.5 Comparison of the 650 GHz DRFS to the 310 GHz DRFS

The designed 650 DRFS has a wider beam and better beam quality than the 310 GHz DRFS despite the higher frequency. The most important reasons for this are described in this section.

Perhaps the most important improvement to the synthesis procedure was that also the output field phase pattern was optimised. The output field phase optimisation was found to be very effective for optimising the simulated hologram illumination.

In the 310 GHz DRFS designing [13], the desired hologram illumination and the output field for the reflector synthesis were thought to be the same. The difference between those fields can be considered as a synthesis error. This synthesis error is larger with a wider beam of the output field for the synthesis. In the 650 GHz DRFS designing, it was accepted that the desired hologram illumination and the output field for the synthesis are not the same. A larger synthesis error can be accepted if the (simulated) hologram illumination is acceptable.

In the 650 GHz DRFS the edge illuminations of the reflectors are lower than in the 310 GHz DRFS. The ripples in the hologram illumination field are largely caused by edge diffractions.

The time required for one DRFS simulation was reduced significantly. In that version of the GRASP that was available for designing the 310 GHz DRFS, the reflector surfaces had to be originally defined for the GRASP in an irregular grid and interpolated with quintic pseudosplines (QPS) [13]. The QPS interpolation is computationally heavy. Using the much faster cubic interpolation from the regular *xy*-grid (and not calculating the PTD currents every time) reduced the computation time significantly. The reduction in computation time allowed more simulations to be done.

In the beginning of the design process of the 650 GHz DRFS it was not known how to get wider beam with a better beam quality. Therefore, also other improvements were attempted (with less success), for example; non-symmetric aperture mapping, reflector surface extrapolation from several known points instead of using only one anterior point, different shapes for the reflector edge rounding, compensation of the feed horn phase error, and correction functions to the ray end points in the output field aperture and to the interception points at the subreflector. These attempted improvements had undesired effects or no effects and therefore were not included in the current version of the synthesis method.

6.3 Elliptical and hyperbolical DRFS geometries

The possibility to use other than the dual hyperbolical basic geometry for DRFS has been speculated in [13] and also in [16]. The synthesis program has been generalised for all elliptical and hyperbolical DRFS geometries, illustrated in Figure 6.15. Both the 310 GHz and the 650 GHz DRFS are based on hyperboloid-hyperboloid geometry in Figure 6.15 a). Other possible basic geometries are ellipsoid-hyperboloid in Figure 6.15 b), ellipsoid-ellipsoid in Figure 6.15 c), or hyperboloid-ellipsoid in Figure 6.15 d).

Possible advantages are more compact structure, lower cross-polarisation, stronger shaping allowed, etc. Further study would be needed to test these other basic geometries.

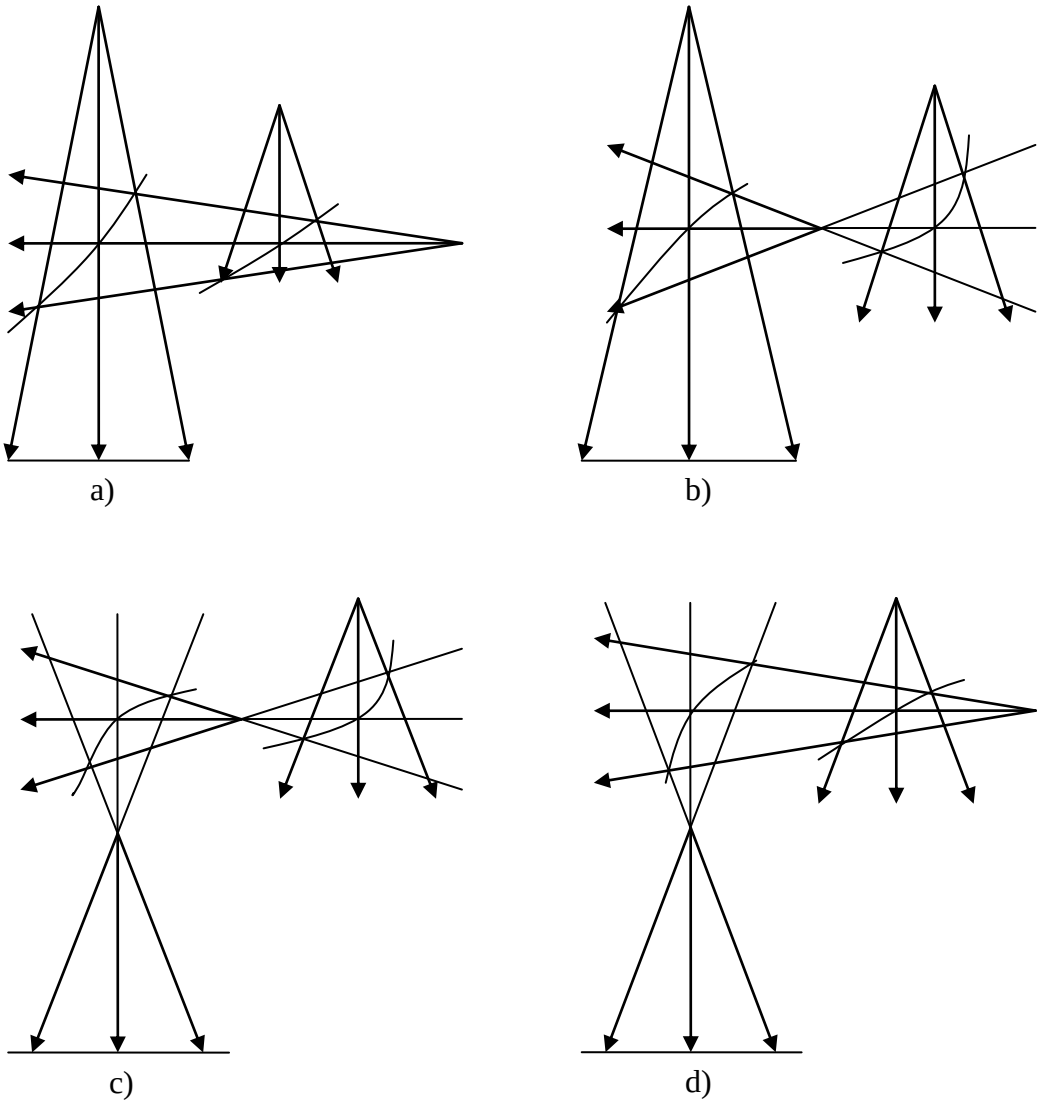

Figure 6.15: Examples of possible DRFS basic geometries: a) hyperboloid-hyperboloid, b) ellipsoid-hyperboloid, c) ellipsoid-ellipsoid, and d) hyperboloid-ellipsoid. Hyperboloid surfaces can be either convex or concave.

7 Shaped lens feed systems

Shaped lens feed system is used to modify the radiation of a primary feed, i.e., the amplitude and the phase of the corrugated feed horn. Both amplitude and phase can be modified by using two shaped surfaces, as in the dual reflector feed systems. The feed system can have one or two lenses, as illustrated in Figure 7.1. In a single lens feed system both lens surfaces are shaped. In a dual lens system both lenses have one shaped and one non-shaped lens surface.

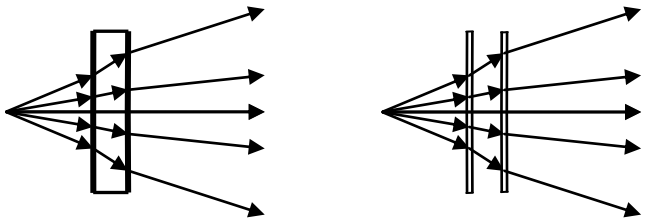

Figure 7.1: Single and dual lens feed systems.

The shaped lens feed systems are rotationally symmetric. Also fields are assumed rotationally symmetric. This greatly facilitates both designing and manufacturing. In the synthesis it is necessary to calculate fields, rays, and surfaces only in one radial cut.

To demonstrate that the synthesis method in Chapter 5 is usable also for shaped lens systems a feed system has been designed with the same design goals as those for the 650 GHz DRFS in Section 6.2.

First a synthesis program was developed for a single lens feed system. But soon it became apparent that the lens would have to be very thick to enable strong shaping to the beam shape. The distance between the shaped surfaces needs to be relatively large, as the distance between the rays, i.e., the power density, changes between the shaped surfaces.

Using two lenses, each of them with one shaped surface, the distance between shaped surfaces can be chosen to be large. The designed dual lens feed system is described in Section 7.1.

The dual lens feed system was designed using the iterative design procedure described in Section 5.2. The parameters of the feed system were optimised by successive synthesis and simulation. The ray-tracing based simulation method in Section 5.4.2 was used in the simulations.

7.1 Dual lens feed system

A shaped lens feed system has been designed for a 650 GHz hologram-based CATR. Same design goals were used as in the 650 GHz DRFS:

- Optimised for a 3.18 metre diameter hologram with $f_{holo}/D_{holo} = 4$.
- Optimised for vertical linear polarisation at 650 GHz.

- –1 dB beam width corresponding to a 2 metre diameter of QZ, i.e., –1 dB beam width radius of 1190 mm in the hologram illumination.
- Hologram edge illumination under –10 dB.
- The amplitude ripple should be less than 0.7 dB peak-to-peak and the deviation from a spherical phase originating from the hologram focal point F_{holo} should be less than 7° peak-to-peak.
- The maximum diameter of the lenses about 200 mm. Also the size of the whole feed system structure should be kept moderate.
- Corrugated feed horn with a Gaussian beam and the –30 dB half-beam width about 25°.

The geometry of the dual lens feed system is described in Section 7.1.1 and the input and the output fields and rays used in the synthesis are described in 7.1.2. The final synthesised surfaces are described in Section 7.1.3 and the simulated hologram illumination in 7.1.4.

7.1.1 Geometry

The geometrical parameters of a dual lens feed system are illustrated in Figure 7.2. The feed system is not in scale. Figure 7.2 shows one radial cut of the rotationally symmetric geometry. The lens directly illuminated by the feed horn is called the first lens and the other is called the second lens.

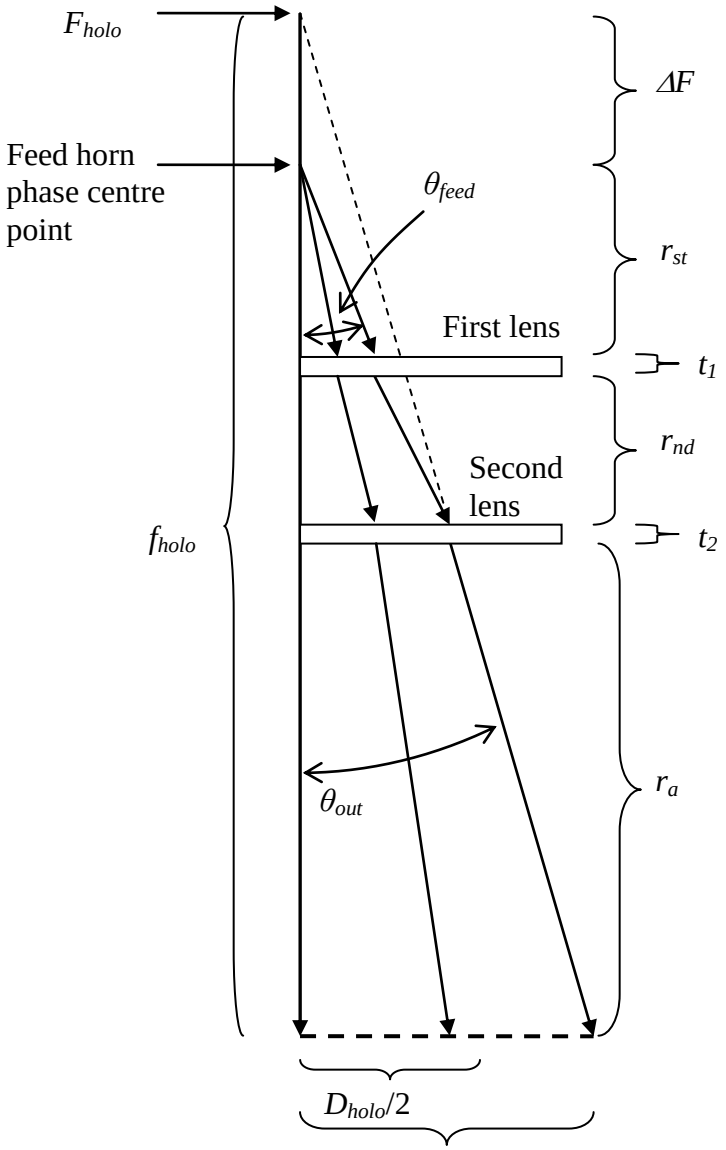

Figure 7.2: Basic geometry of a dual lens feed system. The figure is not in scale.

Geometrical parameters of the designed dual lens feed system are listed in Table 7.1. The hologram and the feed horn phase centre points are at the symmetry axis. The distance between the focal points is

$$\Delta F = f_{holo} - r_{st} - t_1 - r_{nd} - t_2 - r_a \,. \tag{7.1}$$

The thickness of the lenses t_1 and t_2 at the centre, i.e., at the symmetry axis, is predefined before the synthesis. Also the diameters of lenses are largely defined by the geometrical parameters; the diameter of the first lens by θ_{feed} and r_{st}, and the diameter of the second lens by θ_{out} and r_a/f_{holo}. The shape of the synthesised shaped surfaces (in Figure 7.6) finally determines the thicknesses and the diameters of the lenses.

Table 7.1: Geometrical parameters of the designed dual lens feed system.

D	5404 mm
D_{holo}	3180 mm
f_{holo}	12.720 m
r_{st}	100 mm
r_{nd}	160 mm
r_a	12.2045 m
t_1	22.5 mm
t_2	15 mm
θ_{feed}	24º
θ_{out}	12º
ε_r	2.06
ΔF	218 mm

The lens material was chosen to be Teflon with relative permittivity $\varepsilon_r = 2.06$. The choice of lens material is always a compromise between lens size, reflectivity, manufacturing properties, etc. With very low relative permittivity the reflection coefficients are small but the lens size tends to be large, and vice versa for high permittivity.

Two lenses have in total four surfaces. Both lenses have one shaped surface and one non-shaped surface. The four surfaces are chosen to be; counting from the closest to the feed horn towards the hologram, 1) planar, 2) shaped, 3) shaped, and 4) planar.

In general, the order of shaped and non-shaped surfaces could be chosen differently, but the chosen order is easiest for synthesis as then the rays inside the lenses are known before the synthesis. Also, the non-shaped surfaces can be of any predefined shape. Planar surfaces are the easiest for the synthesis and also for manufacturing.

7.1.2 Input and output fields in synthesis

The input and output field amplitudes used in the synthesis are shown in Figure 7.3. 1500 rays were used in the synthesis.

The input field amplitude comes from the radiation pattern of the corrugated feed horn with a Gaussian beam and the -30 dB half-beam width about 25°. In fact the feed horn radiation pattern is not precisely rotationally symmetric, but a rotational symmetry is assumed in the synthesis. Deviation from the rotational symmetry can be taken into account in the simulations. The phase pattern of the feed horn is not included in the synthesis.

The output field is computed from a rotationally symmetric Butterworth-type function:

$$E(\rho) = \frac{1}{\sqrt{1+(\rho/\rho_c)^{2N}}}, \tag{7.2}$$

where $\rho_c \approx 1355$ mm and $N = 10.7$ are the –3 dB point and the degree of the Butterworth function and ρ is the output field aperture coordinate. The output field amplitude outside the hologram area $\rho > 1590$ mm is optimised separately.

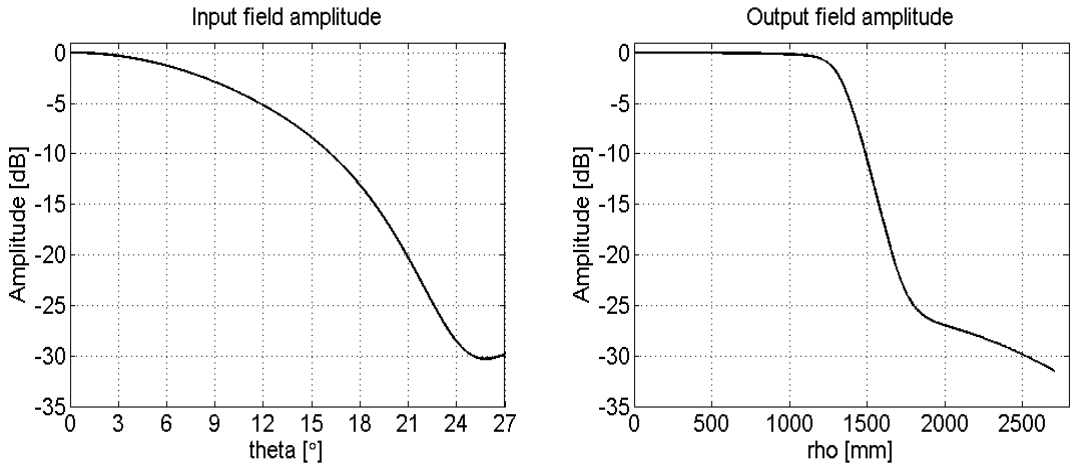

Figure 7.3 Input and output field amplitudes. Input field up to $\theta_{feed} = 24°$ is used in the synthesis. The hologram edge is at $\rho = D_{holo}/2 = 1590$ mm.

Input and output fields and ray grids are defined at the input and output aperture planes. Because the focal points are on the symmetry axis it is convenient to define both aperture planes to be at the hologram plane. Input rays originate from the feed horn focal point and end at the hologram plane at points defined by the input ray grid. The output rays originate from the hologram focal point F_{holo} and end at the hologram plane at points defined by the output ray grid.

The input ray grid has been made denser towards the edge of the input aperture plane, in order to get more rays to where the output field changes rapidly. The output ray grid is calculated in the rotationally symmetric aperture mapping as explained in Section 5.3.2.4 using (5.34). Ray grids can be best described by distance between neighbouring ray grid points shown in Figure 7.4.

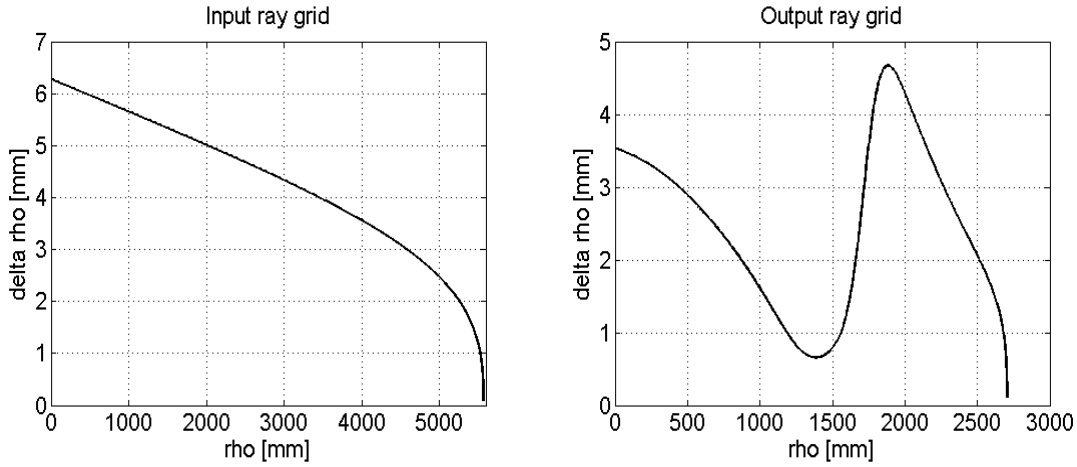

Figure 7.4: Ray spacing $\Delta\rho$ of the input and output ray grids.

Modifying the output field phase did not have the same effect as in the case of 650 GHz DRFS. That is because the angle between the incoming ray and reflected ray is about 90° and angle between the incoming ray and refracted ray is about 0°. Therefore in case of the DRFS the direction of the ray between shaped surfaces changes much more than in the case of a shaped lens feed system. Modifying the direction of the rays between shaped surfaces modifies the amplitude. The output field phase affects both amplitude and phase for DRFS but it affects mostly only the phase in shaped lens feed system. Of course, it is not that simple, as the ray length correction changes the surface shape, but the basic principle is as explained.

7.1.3 Synthesis and the synthesised surfaces

The centre ray is known from the definition of the geometry in Figure 7.2. After the centre ray the synthesis procedure is the same for each ray. Ray directions inside the lenses are known; only the two middle surfaces and rays between lenses need to be determined. The synthesis procedure is as explained in Section 5.3.3, except that only one radial cut is synthesised, i.e., rays n_{ray}= 1 ... N.

The total ray length is corrected by moving the points in the shaped surface of the second lens. These points are moved in direction of the rays inside the second lens. The desired ray length is calculated from (5.36), in which the constant *C* can be calculated from the centre ray geometry:

$$C = f_{holo} - \left(r_{st} + \sqrt{\varepsilon_r}\,t_1 + r_{dn} + \sqrt{\varepsilon_r}\,t_2 + r_a\right) \approx 201.68\,mm\,. \tag{7.3}$$

The synthesised surfaces and some of the rays are shown in Figure 7.5. For clarity only 40 of the 1500 rays are shown.

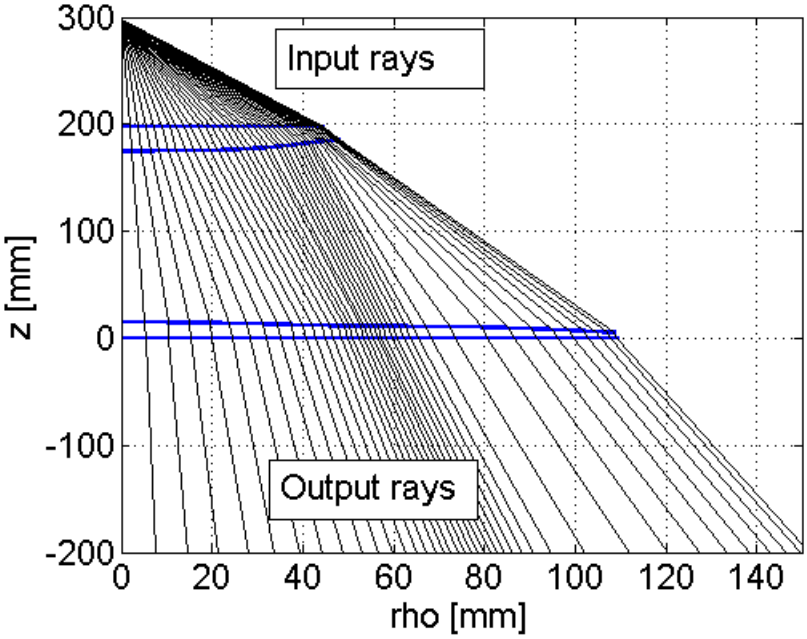

Figure 7.5: Rays in synthesis. Only 40 of the 1500 rays shown.

Circular rounding and planar section are fitted around the shaped surfaces; in a same way as in case of the dual reflector feed systems in Chapter 6. The final lens profiles of the first and the second lens surfaces are shown in Figure 7.6. The first lens is 22.5 mm thick and has a diameter of about 120 mm. The second lens is 15 mm thick and has a diameter of about 260 mm. The final diameters of the lenses depend on the mechanical design, i.e., how large planar area is needed to attach the lenses to mechanical supports.

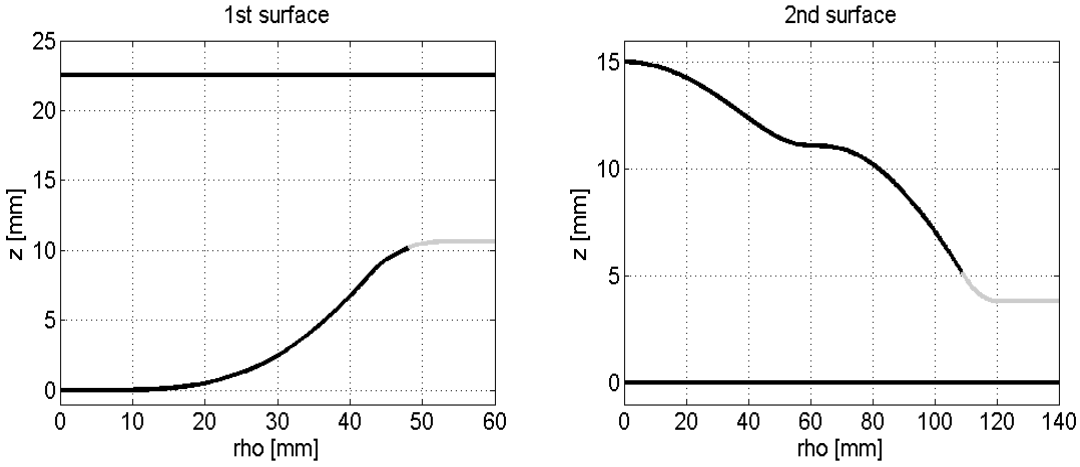

Figure 7.6: Lens profiles of the first and the second lens surfaces. The synthesised surfaces are shown in black and edge rounding and added planar section in gray line.

7.1.4 Simulated hologram illumination

The ray-tracing based simulation method described in Section 5.4.2 is used to calculate the field at the hologram. The field at the aperture of the feed system (at $z = 0$ in Figure

7.5 and Figure 7.7) is calculated by ray-tracing (Sections 5.4.2.1 and 5.4.2.2) and the field at the hologram is calculated from the aperture field with Huygens' principle (Section 5.4.2.3). Same feed horn radiation pattern is used as in the synthesis.

The final results were calculated using 4000 rays. The rays were launched from the feed horn phase centre point at angles θ = 0°...27° with a constant $\Delta\theta$. 40 of the rays are shown in Figure 7.7.

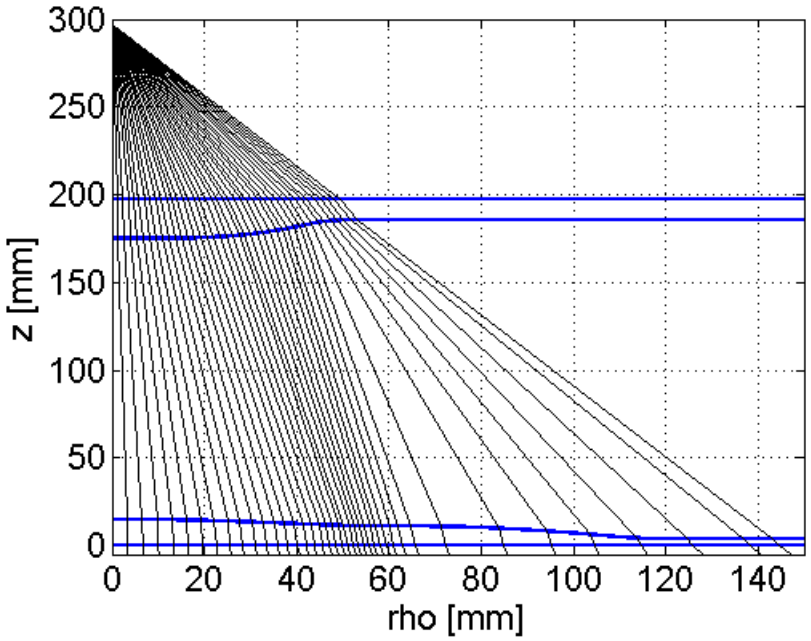

Figure 7.7: Rays in the ray-tracing simulation. Only 40 of the 4000 rays shown.

The aperture field, at z = 0 in Figure 7.7, is calculated from the rays as explained in Section 5.4.2.2. The aperture field amplitude is calculated from the input field amplitude shown in Figure 7.3 and the transmission coefficients shown in Figure 7.8 as function of the ray end point in the aperture. The transmission coefficients in (5.11) and (5.13) depend on incident angle θ_1 (calculated for each ray on each surface when the ray path is calculated) and on the polarisation compared to the surface. Because the feed horn has a linear vertical polarisation, the polarisation is at the horizontal cut of the aperture perpendicular and at the vertical cut the polarisation is parallel. The total transmission coefficients T are calculated from (5.40).

Aperture field phase in Figure 7.9 is determined from the total electrical lengths of the rays. Vertical and horizontal cuts of the aperture field amplitude are also shown in Figure 7.9. The aperture field between the field cuts is interpolated as in (5.47). Aperture field up to ρ = 120 mm was calculated in 1199 points in ρ–direction and 240 points in ϕ–direction.

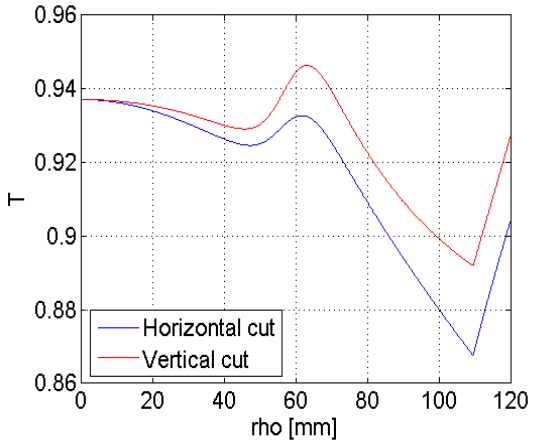

Figure 7.8: Total transmission coefficient at the aperture; perpendicular polarisation at the horizontal cut and parallel polarisation at the vertical cut.

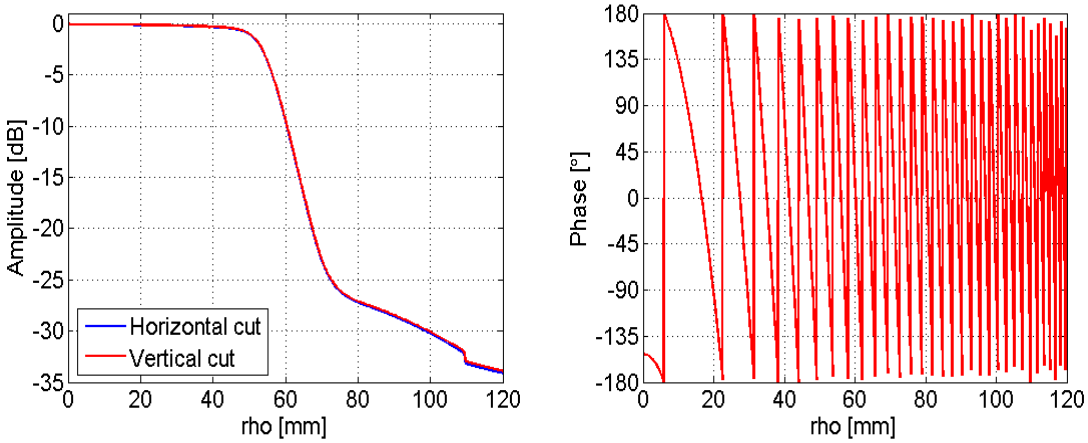

Figure 7.9: Aperture field, behind the 2nd lens, at z = 0; amplitude and phase at vertical polarisation at 650 GHz.

The hologram illumination was calculated from the aperture field with Huygens' principle as explained in Section 5.4.2.3. The amplitude and phase deviation from the spherical wave at the vertical polarisation at 650 GHz is shown in the hologram area in Figure 7.10.

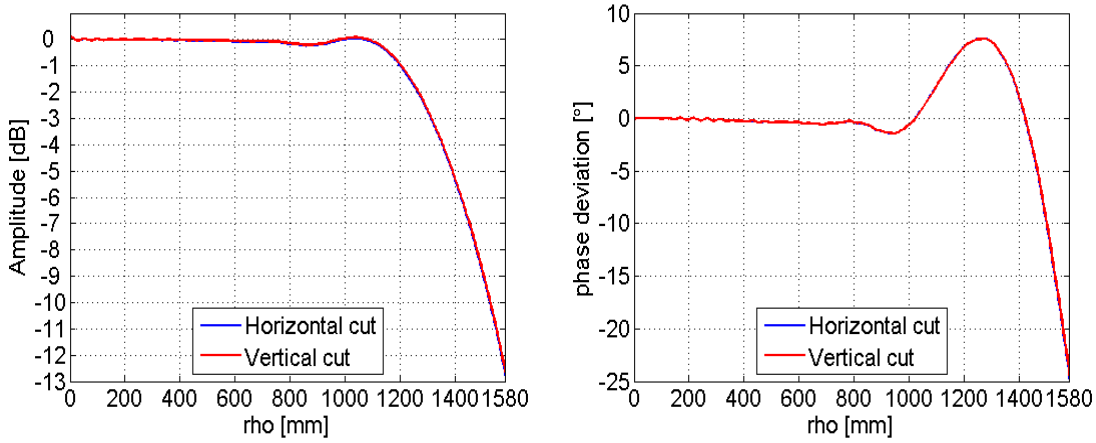

Figure 7.10: Simulated hologram illumination; amplitude and phase deviation from the spherical wave at the vertical polarisation at 650 GHz.

The –1 dB beam width radius is about 1200 mm, which corresponds to a 2 metre diameter of QZ. Hologram edge illumination is about –12.5 dB, i.e., clearly better than the required –10 dB. The horizontal and vertical field cuts are nearly identical.

The simulated amplitude and phase deviation ripples are clearly lower than the minimum requirements specified for the feed system. The amplitude ripple is about 0.32 dB peak-to-peak. The phase deviation ripple is about 8° peak-to-peak. The phase deviation could be partially compensated by placing the feed system a few millimetres closer to the hologram. In the area corresponding to the centre of the QZ, $\rho < 800$ mm in Figure 7.10, the amplitude ripple is only 0.26 dB peak-to-peak and the phase ripple only about 0.7° peak-to-peak. In principle, smooth variations (but not ripple) could be taken into account in the hologram design.

7.1.5 Comparison to the 650 GHz DRFS

The 650 DRFS, described in Section 6.2, and the designed dual lens feed system are designed with same design goals. The simulated hologram illuminations are compared in Table 7.2. The corresponding QZ diameter is calculated to be $\cos(33°)$ times the –1 dB beam width of the feed system at the hologram plane. Also, peak-to-peak amplitude and phase ripples and the hologram edge illumination are given.

Table 7.2: Comparison of the designed dual lens feed system to the designed 650 GHz DRFS; simulated amplitude and phase patterns.

	650 GHz DRFS	Dual lens feed system
QZ diameter	1.962 m	2.013 m
Amplitude ripple; peak-to-peak	0.45 dB	0.26 dB
Phase ripple; peak-to-peak	5°	0.7°
Hologram edge illumination	–10 dB	–12.5 dB

All the simulation results in Table 7.2 are in favour of the dual lens feed system. It appears that a wide beam with an edge tapering is easier to design with a dual lens feed system than with a dual reflector feed system. The cross-polarisation level from the DRFS is relatively high, at maximum about –20 dB. Cross-polarisation is not included in the lens simulation method, but in general lens antennas cause relatively low cross-polarisation levels.

For comparison reasons, the maximum size of a lens was limited to be approximately same as the size of the larger reflector in the DRFS. Size limitations, for both the whole feed system and for the shaped surfaces, have a significant influence on the design process. Both with reflectors and with lenses, a beam-shaping is easier with larger shaped surfaces and with more freedom to choose the geometry of the feed system. Size limitations should be based on practical manufacturing accuracy limitations.

The simulation method used for the DRFS can be considered to be very accurate. The simulation method used for dual lens feed system is based on ray-tracing with many approximations, as explained in Section 5.4.2. Importantly, reflections from the lens surfaces are not taken into account. The reflections can potentially have significant effect to the amplitude and phase ripples and should be calculated for reliable comparison to the DRFS.

As explained in Section 2.3.2, the surface accuracy requirement is not as stringent for a lens as for a reflector. With a Teflon lens at 650 GHz about four times larger surface errors in a lens, compared to a reflector, result in equal phase error for the rays. Also, the designed lenses are rotationally symmetric which makes the manufacturing easier.

8 Measurements

Antenna measurements relevant to this thesis are presented in this chapter. These measurements are all related to the measurement of the representative test object (RTO) in a hologram-based CATR at 650 GHz [12]. The 650 DRFS, presented in Section 6.2, was used to provide the modified illumination for the hologram. A corrugated horn antenna was used in both the DRFS and in the RTO. The beam widths of the horns were measured and the results are presented in Section 8.1. The 650 DRFS was measured with a planar near-field scanner. The 650 DRFS measurements are presented in Section 8.2. The measured QZ of a hologram-based CATR is presented in Section 8.3.

8.1 The 650 GHz feed horns

The RTO feed horn and the DRFS feed horn was measured together with a third 650 GHz probe horn using a three antenna method. All the three antennas are corrugated horn antennas manufactured by Thomas Keating Ltd. with the same specifications.

The antenna technique used to measure the feed horns is the so-called three antenna method. The gain patterns for antennas A, B, and C are calculated, according to (8.1)-(8.3), from three measurements.

$$G_A(dB) = 10 \cdot \log\left(\sqrt{\frac{P_{AB} \cdot P_{AC}}{P_{BC}}}\right) \tag{8.1}$$

$$G_B(dB) = 10 \cdot \log\left(\sqrt{\frac{P_{AB} \cdot P_{BC}}{P_{AC}}}\right) \tag{8.2}$$

$$G_C(dB) = 10 \cdot \log\left(\sqrt{\frac{P_{AC} \cdot P_{BC}}{P_{AB}}}\right), \tag{8.3}$$

where $P_{ij} = G_i(\theta)G_j(\theta)$ is the measured amplitude with antennas *i* and *j*. The three measurements needed were:

P_{BC} : RTO feed horn in the transmitter and the probe in the receiver.

P_{AC} : DRFS feed horn in the transmitter and the probe in the receiver.

P_{AB} : DRFS feed horn in the transmitter and the RTO feed horn in the receiver.

The objective of this measurement was to determine the beam widths of the feed horns. The horizontal cuts of the measured and simulated amplitude of the 650 GHz corrugated feed horns are presented in Figure 8.1. To determine the beam width, the simulated amplitude pattern was slightly modified to best fit to the measured patterns. Therefore, the measured amplitude ripples are not included in the resulting patterns of the feed horns.

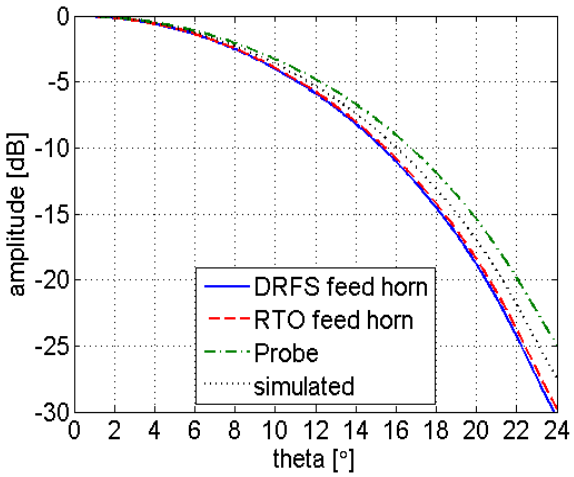

Figure 8.1: Horizontal cuts of the measured and simulated amplitude of the 650 GHz corrugated feed horns.

As seen from Figure 8.1, the beam width of the DRFS feed horn is narrower than the simulated beam width that was used in designing the DRFS, and in the simulations presented in Section 6.2. Due to the narrower feed horn beam, the hologram illumination and also the quiet-zone is slightly narrower. But the difference can be considered to be relatively small.

8.2 The 650 GHz DRFS

The 650 GHz DRFS was measured by near-field scanning with a planar scanner [85]. Amplitude and phase patterns at the main polarisation and the cross-polarisation level were measured. The measurement was done to ensure that the DRFS was designed and manufactured successfully.

The measurement setup is presented in Section 8.2.1. Due to the very high frequency (short wavelength) several error compensation techniques were used, as explained in Section 8.2.2. A special planarity error correction technique that was used is explained in Section 8.2.3. Finally the measurement results are presented and compared to the simulation results in Section 8.2.4.

8.2.1 Measurement setup

The DRFS was measured with a planar near-field scanner, shown in Figure 8.2, at 650 GHz. A corrugated horn was used in the receiver to probe the radiated field. This probe horn is one of the horns measured in Section 8.1. The receiver is mounted on the planar scanner. The DRFS is placed on a positioner used to move the DRFS. The AUT positioner was needed for the planarity error correction technique in Section 8.2.3. The two-dimensional scanning area was measured using vertical scans and the tie-scans were horizontal.

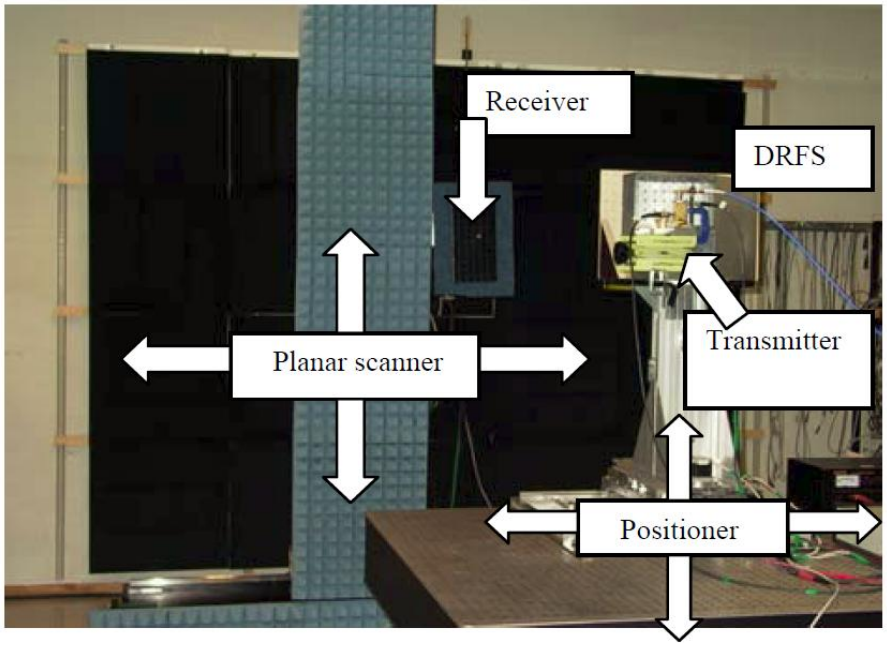

Figure 8.2: The measurement setup; the AUT positioner and the planar scanner.

The measurement distance was 1.1 meters. In the CATR the distance from the DRFS to the hologram is 12.72 metres. According to simulations the beam shape is about the same at both of these distances. Therefore, the beam shape can be verified at the shorter distance. The measurement distance corresponds to $f_{holo} \approx 1508$ mm, i.e., to a hologram diameter of about 377 mm.

AB Millimetre MVNA-8-350 vector network analyzer was used with a 5^{th}-harmonic multiplier in the transmitter and a 5^{th}-harmonic mixer in the receiver as the sub-millimetre wave extensions.

8.2.2 Error compensation techniques

Several measurement techniques were used to reduce measurement errors; averaging of measurements, drift compensation with tie-scans, probe correction, and planarity error correction. The planarity correction is discussed in Section 8.2.3.

Random errors can be reduced by taking an average of several measurements. The measurements uncertainty related to random errors is reduced by the square root of the number of measurements.

During the long two-dimensional measurements amplitude and phase drift can be significant. The two-dimensional measurements were done with vertical scans. The amplitude and phase at the centreline was normalised to amplitude and phase of a separately measured horizontal scan, i.e., a tie-scan.

Probe correction is necessary as the measurement area covers relatively large direction of arrival area of the probe. The effect of the measured probe amplitude pattern (“Probe” in Figure 8.1) was removed computationally from the measurements.

8.2.3 Planarity error correction technique

Planarity error is the most significant phase error source in submillimetre wave planar field probing [86]. The effects of known planarity error can be corrected from the measured phase pattern. The phase error $\Delta\Psi(x, y)$ caused by the planarity error $z(x, y)$ is given in (2.3).

The planarity of the used near-field scanner was measured with a laser tracker interferometer. The measurement uncertainty in the laser tracker interferometer measurements was ±20 μm (with 2 sigma specifications), i.e., the planarity correction accuracy would be ±16° at 650 GHz. Planarity error correction based on laser tracker measurements was used at 310 GHz in [13], but for the measurement at 650 GHz the planarity data based on the laser tracker measurement is not accurate enough.

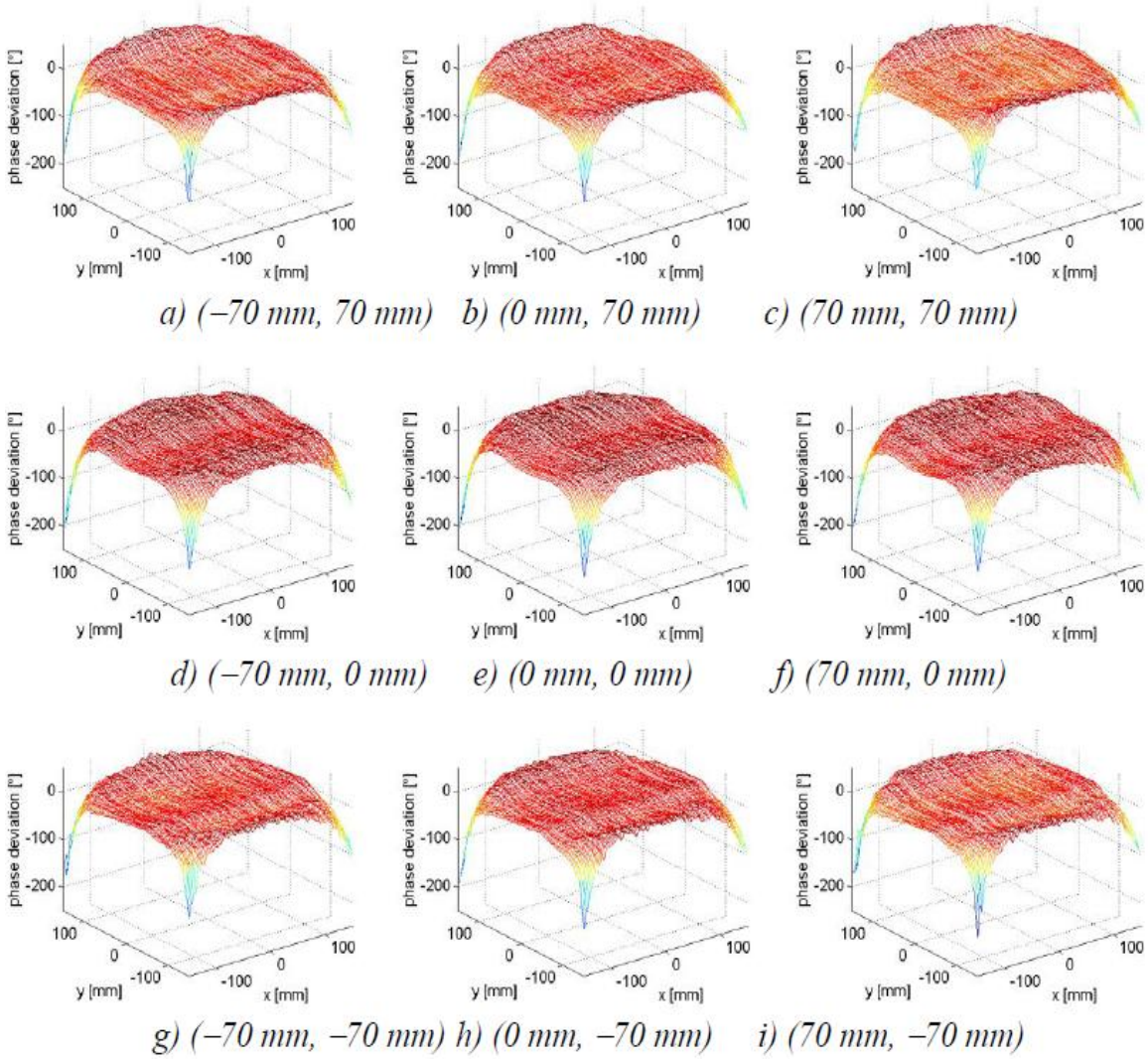

Figure 8.3: Phase deviation with planarity correction based on the laser tracker using different areas of the scanning plane; a) – i) offsets (x, y) of the measurement areas. Location of the focal point calculated separately for each of these measurements.

To test the planarity correction, first the measurement was repeated in a few different measurement areas, i.e., both the DRFS and the two-dimensional measurement area were moved between the measurements. After drift compensation with tie-scans, probe correction, and planarity error correction based on the laser scanner measurements the resulting phase deviation patterns were clearly different depending on which part on the scanning plane had been used. In Figure 8.3, there are examples of this kind of phase deviation patterns.

The differences between the measured phase patterns are caused by errors related to the position of the probe on the scanning plane. The scanner planarity and position errors as well as the cable flexing errors can be calculated by minimizing the differences between the error compensated phase patterns. The error correction method is based on two principles, as explained in [85]: 1) the planarity corrected phase pattern should be independent of the used area of the scanning plane, and 2) the differences between the planarity corrected phase patterns when using different parts of the scanning plane are caused by the errors in the planarity correction.

The new planarity correction was calculated by optimising parameters h_m and h_n in (8.4). The parameter optimisation is based on minimising the average standard deviation of the planarity error compensated phase deviation patterns in the central region [85].

$$z(x,y) = z_{LS}(x,y) + \sum_{m=1}^{23} h_m e^{-\frac{1}{2}\left(\frac{x-\mu_m}{\sigma}\right)^2} + \sum_{n=1}^{23} h_n e^{-\frac{1}{2}\left(\frac{y-\mu_n}{\sigma}\right)^2}, \tag{8.4}$$

where:

$$\begin{aligned} \mu_n &= -330\ mm + (n-1)\cdot 30\ mm \\ \mu_m &= -330\ mm + (m-1)\cdot 30\ mm \\ \sigma &= 30\ mm, \end{aligned} \tag{8.5}$$

and x and y are the coordinates on the scanning plane. $z_{LS}(x,y)$, is the planarity measured with laser tracker and it provides a good initial value for the planarity correction optimisation.

The differences between the planarity corrected phase patterns were clearly reduced. The average standard deviation using the planarity correction measured with laser tracker is 4.8° and with the planarity correction calculated from the measured phase patterns it was 2.7°. The measurement uncertainty due to planarity correction was almost halved.

The planarity correction based on the laser tracker measurements is presented in Figure 8.4 a) and the planarity correction calculated from measured phases is presented in Figure 8.4 b).

For each of the measurements the focal point of the spherical wave was calculated from the planarity corrected phase patterns. In practice this means that linear slope in the phase deviation from the spherical wave was assumed to be due to error in the AUT positioner movement error and not due to linear slope in the planarity.

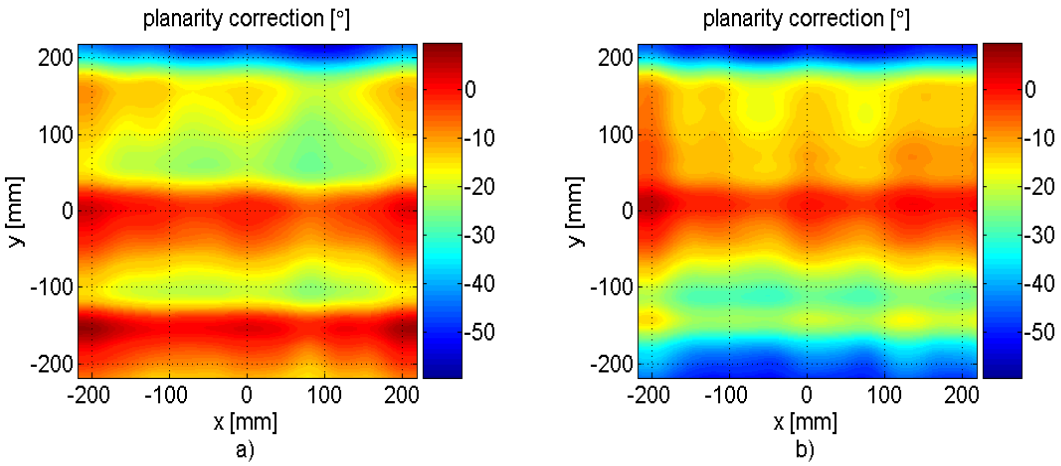

Figure 8.4: Planarity correction (degrees in phase at 650 GHz), a) measured with laser tracker, b) calculated from measured phases [85].

8.2.4 Measurement results of the 650 GHz DRFS

The measured and simulated amplitude patterns at 650 GHz at the vertical polarisation are presented in Figure 8.5. These simulations were done with GRASP8W with the feed horn beam width based on the measurements in Section 8.1. The measured amplitude pattern is an average of all of the measured and drift compensated amplitude patterns with probe correction.

The measured and simulated phase deviation patterns are shown in Figure 8.6. The measured phase deviation pattern is an average of all of the measured and drift compensated amplitude patterns with the calculated planarity correction from Figure 8.4 b).

The two-dimensional and the tie-scan measurements at the vertical polarisation were repeated using 13 times slightly different areas of the scanning. In total 20 two-dimensional measurements were done, reducing the effect of random errors significantly.

The beam shape, i.e., the −1 dB beam width and the hologram edge illumination, is about the same in the measured and the simulated amplitude patterns. The amplitude ripple in the central region of the beam is about 0.8 dB peak-to-peak in the measured and about 0.45 dB peak-to-peak in the simulated. The measured phase ripple in the central region is about 15° peak-to-peak and in the simulated about 5° peak-to-peak.

The cross-polarisation level was measured by turning the DRFS feed horn by 90°. The measured cross-polarisation level was at maximum about –14.3 dB below the main polarisation maximum. The simulated cross-polarisation is at maximum about −20 dB. The difference is probably mainly caused by probe orientation errors, feed horn orientation, and possible misalignment of the reflectors in the DRFS structure.

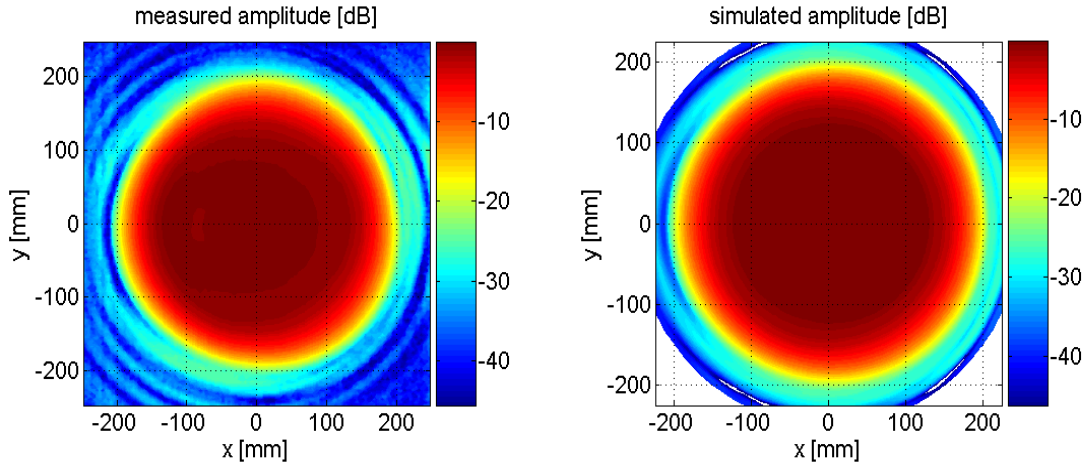

Figure 8.5: Measured and simulated normalised amplitude at 650 GHz at the vertical polarisation [85].

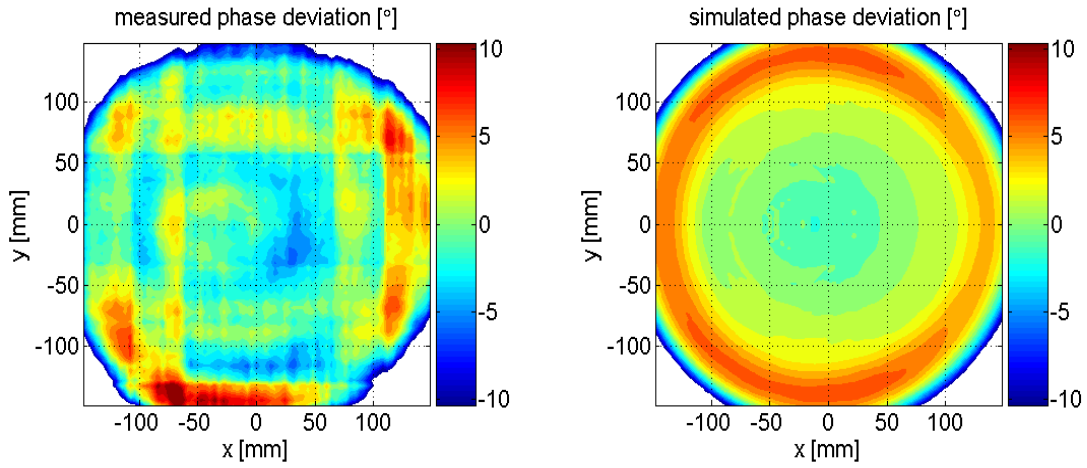

Figure 8.6: Measured and simulated phase deviation from the spherical wave at 650 GHz at the vertical polarisation [85].

The measurement results of the 650 GHz DRFS prove that no significant design or manufacturing errors were made. The beam shape is only slightly different, the ripples and the cross-polarisation level are larger, but considering the accuracy requirements for the DRFS structure, and for the surface accuracy, the differences are small.

8.3 Hologram-based CATR at 650 GHz

The 650 GHz DRFS was used in antenna test in a hologram-based compact antenna test range [12]. This was a first time a feed system has been used in an antenna measurement in a hologram-based CATR. The description of the CATR, instrumentation, quiet-zone test results, and the antenna measurement result are presented in [12]. The CATR layout is illustrated in Figure 2.9. The antenna under test was the RTO, shown in Figure 2.8. This is the highest frequency at which a large antenna has ever been measured in any CATR [12].

Horizontal and vertical scans of the QZ field are shown in Figure 8.7 and Figure 8.8, respectively. The effects of the ripples in the illuminating beam and the effects due to the hologram can be identified from the QZ field scans. For example, by comparing Figure 6.12 to Figure 8.7 it can be seen that the beam shape remains the same, including the ripples in the illuminating field. The hologram adds more ripples and also the effect of the upper seam of the hologram is clearly visible in the vertical scan at the probe position of about 650 mm.

The measured QZ phase deviations were very large. Due to problems with the quiet-zone scanner, and the resulting high quiet-zone phase measurement uncertainty, QZ phase quality is difficult to estimate reliably. In the region of the AUT, the maximum measured cross-polarization level is –25 dB.

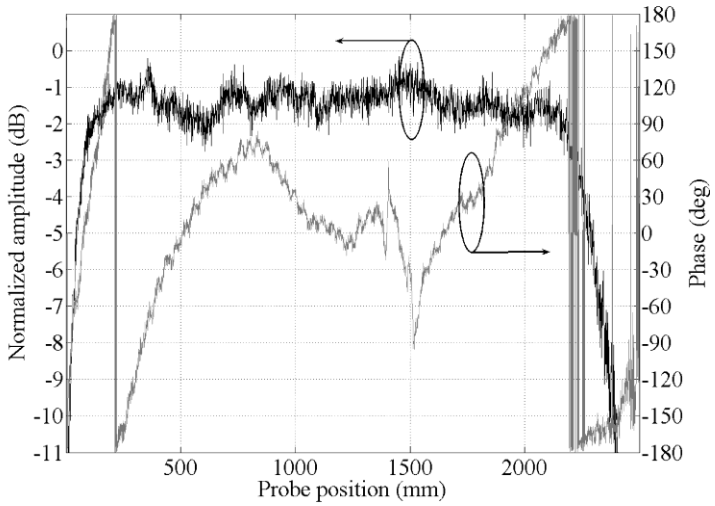

Figure 8.7: Horizontal scan of the quiet-zone field. AUT centre at 1290 mm [12].

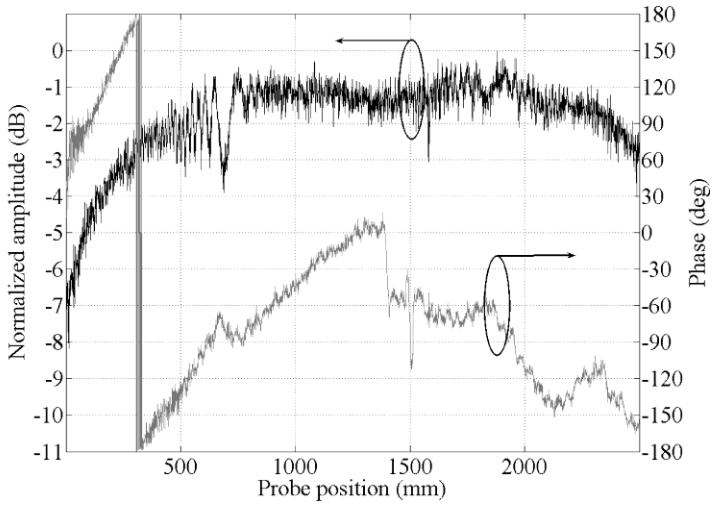

Figure 8.8: Vertical scan of the quiet-zone field. AUT centre at 1290 mm [12].

9 Conclusions

Feed systems for hologram-based compact antenna test ranges (CATRs) have been developed. Feed system can be used to provide a modified illumination for the hologram with shaped amplitude and phase patterns. Hologram-based CATR can be used to test large antennas at high frequencies.

The main advantage of using a feed system to provide the illumination for the hologram, instead of a traditional horn antenna, is that narrow slots can be avoided in the hologram pattern. Narrow slots are difficult to manufacture accurately and limit the polarisation properties of the hologram.

A numerical synthesis method based on ray-tracing is used to design feed systems for hologram-based CATRs. Two dual reflector feed systems (DRFSs) have been designed, manufactured, and tested. The synthesis method was first developed and used to design a 310 GHz DRFS. In this work a 650 GHz DRFS is designed as part of an ESA project aiming at the measurement of a 1.5 m antenna at 650 GHz.

In the synthesis method, the electromagnetic fields are represented with rays. The rays and ray tubes represent the local plane wave amplitude and phase. The synthesis of the feed system starts with defining the basic geometry. Then input and output fields and rays are defined. Finally, the shaped surfaces are synthesised based on the defined geometry and fields. The shaped surfaces are approximated with locally planar sections. The design process used to design the feed systems is based on an iterative optimisation procedure. One iteration round has three parts: the synthesis of the surfaces, simulation, and analysis of the simulation results.

The 650 GHz DRFS, presented in this thesis, was optimised based on the simulations with GRASP8W that were done with physical optics (PO). The simulation results are better than the minimum requirements defined for the feed system; the beam width corresponds to a 1.96 metre diameter QZ, the hologram edge illumination is less than –10 dB, amplitude ripple in the –1 dB beam area is 0.45 dB peak-to-peak, and the phase deviation from a spherical wave is 5° peak-to-peak.

The designed 650 DRFS has a wider beam and better beam quality than the 310 GHz DRFS despite the higher frequency. The most important reason for this is that also the output field phase pattern was optimised. The output field phase optimisation was found to be very effective for optimising the simulated hologram illumination. In the 650 GHz DRFS the edge illuminations of the reflectors are lower than in the 310 GHz DRFS. The ripples in the hologram illumination field are largely caused by edge diffractions.

The 650 GHz DRFS was manufactured at Thomas Keating Engineering Physics, Ltd. It was measured by near-field scanning with a planar scanner at 650 GHz. The measured beam shape is about the same as the simulated one. The measured amplitude ripple in the central region of the beam is about 0.8 dB peak-to-peak and the phase ripple is about 15° peak-to-peak. The measurement results of the 650 GHz DRFS prove that no significant design or manufacturing errors were made.

The 650 GHz DRFS was used in a large antenna measurement campaign in which a 1.5 m antenna was tested at 650 GHz in a hologram-based compact antenna test range.

The feed system design and synthesis method has been extended also for feed systems based on shaped dielectric lenses. A dual lens feed system design example was designed, with same design goals as those with the 650 GHz DRFS. In the simulations, the aperture field of the feed system was calculated with the same ray-tracing principles that are used also in the synthesis method. The design example proves that the synthesis method can be used also for feed systems based on shaped lenses.

References

[1] N. Mandolesi and F. Villa, “FIRST/Planck mission,” *16th IEEE Instrumentation and Measurement Technology Conference (IMTS’97)*, vol. 2, Venice, Italy, May 1999, pp. 975–980.

[2] P. de Maagt, D. de Chambure, D. Doyle, and G. Crone, “Planck and Herschel instruments and antenna technology,” *Antennas and Propagation International Symposium, 2007 IEEE*, Honolulu, Hawaii, USA, 9–15 June 2007, pp. 4361–4364.

[3] D. Leisawitz, et al., “SPECS: The kilometer-baseline far-IR interferometer in NASA's space science roadmap,” *Optical, Infrared, and Millimeter Space Telescopes*, edited by John C. Mather, *Proceedings of SPIE*, vol. 5487, pp. 1527–1537, 2004.

[4] J. W. Waters, et al., “The Earth Observing System Microwave Limb Sounder (EOS MLS) on the Aura satellite,” *IEEE Transactions on Geoscience and Remote Sensing*, vol. 44, pp. 1075–1092, 2006.

[5] T. Manabe, “Development of superconducting submillimeter-wave limb-emission sounder (JEM/SMILES) aboard the International Space Station,” *Journal of the Communications Research Laboratory*, vol. 49, no. 2, pp. 9–20, 2002.

[6] Y. J. Kasai, J. Urban, C. Takahashi, S. Hoshino, K. Takahashi, J. Inatani, M. Shiotani, and H. Masuko, “Stratospheric ozone isotope enrichment studied by submillimeter wave heterodyne radiometry: the observation capabilities of SMILES,” *IEEE Transactions on Geoscience and Remote Sensing*, vol. 44, no. 3, pp. 676–693, Mar. 2006.

[7] J. Tuovinen, A. Vasara, and A. Räisänen, “A new type of compact antenna test range,” in *Proceedings of the 22nd European Microwave Conference*, Espoo, Finland, 1992, pp. 503–508.

[8] T. Hirvonen, J. Ala-Laurinaho, J. Tuovinen, and A. V. Räisänen, “A compact antenna test range based on a hologram,” *IEEE Transactions on Antennas and Propagation*, vol. 45, no. 8, pp. 1270–1276, Aug. 1997.

[9] T. Sehm, J. Ala-Laurinaho, T. Hirvonen, and A. V. Räisänen, “Antenna measurements using a hologram CATR,” *Electronics Letters*, vol. 35, no. 10, pp. 757–758, May 1999.

[10] J. Ala-Laurinaho, T. Hirvonen, P. Piironen, A. Lehto, J. Tuovinen, A. V. Räisänen, and U. Frisk, "Measurement of the Odin telescope at 119 GHz with a hologram-type CATR," *IEEE Transactions on Antennas and Propagation*, vol. 49, no. 9, pp. 1264–1270, Sept. 2001.

[11] J. Häkli, T. Koskinen, A. Lönnqvist, J. Säily, V. Viikari, J. Mallat, J. Ala-Laurinaho, J. Tuovinen, and A. V. Räisänen, "Testing of a 1.5-m reflector antenna at 322 GHz in a CATR based on a hologram," *IEEE Transactions on Antennas and Propagation*, vol. 53, no. 10, pp. 3142–3150, Oct. 2005.

[12] A. Karttunen, J. Ala-Laurinaho, M. Vaaja, T. Koskinen, J. Häkli, A. Lönnqvist, J. Mallat, A. Tamminen, V. Viikari, and A. V. Räisänen, "Antenna tests with a hologram-based CATR at 650 GHz," *IEEE Transactions on Antennas and Propagation*, vol. 57, no. 3, pp. 711–720, Mar. 2009.

[13] J. Häkli, *Shaped reflector antenna design and antenna measurements at sub-mm wavelengths*, Doctoral Thesis, Helsinki University of Technology, 2006, 217 p. Available: URL: http://lib.tkk.fi/Diss/2006/isbn9512283409/.

[14] J. Häkli, T. Koskinen, J. Ala-Laurinaho, and A. V. Räisänen, "Dual reflector feed system for hologram-based compact antenna test range," *IEEE Transactions on Antennas and Propagation*, vol. 53, no. 12, pp. 3940–3948, Dec. 2005.

[15] J. Häkli, J. Ala-Laurinaho, and A. V. Räisänen, "Numerical synthesis method for designing a shaped dual reflector feed system," *IEE Proceedings – Microwaves, Antennas and Propagation*, vol. 152, no. 5, pp. 311–318, Oct. 2005.

[16] A. Karttunen, *Design of a 650 GHz dual reflector feed system*, Master's Thesis, Helsinki University of Technology, 2006, 70 p. Available: URL: http://lib.tkk.fi/Dipl/2006/urn006242.pdf.

[17] A. Karttunen, J. Häkli, and A. V. Räisänen, "Design of a 650 GHz dual reflector feed system for a hologram-based CATR," in *Proceedings of the European Conference on Antennas and Propagation (EuCAP 2006)*, Nice, France, Nov. 6–10, 2006, CD-ROM SP-626, paper 359216.

[18] *IEEE Standard Test Procedure for Antennas*, IEEE Standard 149-1979, the Institute of Electrical and Electronics Engineers, USA, 1979, 149 p.

[19] *IEEE Standard Definitions of Terms for Antennas*, IEEE Standard 145-1983, the Institute of Electrical and Electronics Engineers, USA, 1983, 31 p.

[20] R. C. Hansen, "Measurement distance effects on low sidelobe patterns," *IEEE Transactions on Antennas and Propagation*, vol. AP-32, no. 6, pp. 591–594, 1984.

[21] E. B. Joy and D. T. Paris, “Spatial sampling and filtering in near-field measurements,” *IEEE Transactions on Antennas and Propagation*, vol. 20, no. 3, pp. 253–261, 1972.

[22] D. Slater, P. Stek, R. Cofield, R. Dengler, J. Hardy, R. Jarnot, and R. Swindlehurst, “A large aperture 650 GHz near-field measurement system for the Earth Observing System Microwave Limb Sounder,” in *Proceedings of 23rd AMTA*, Denver, USA, Oct. 2001, pp. 468−473.

[23] E. B. Joy, “Near-field range qualification methodology,” *IEEE Transactions on Antennas and Propagation*, vol. 36, no. 6, pp. 836–844, 1988.

[24] A. C. Newell, “Error analysis techniques for planar near-field measurements,” *IEEE Transactions on Antennas and Propagation*, vol. 36, no. 6, pp. 754–768, 1988.

[25] G. A. Woonton, R. B. Borts, and J. A. Caruthers, “Indoor measurements of microwave antenna radiation patterns by means of a metal lens,” *Journal of Applied Physics*, 11, May 1950, pp. 428–430.

[26] A. D. Olver, “Compact antenna test ranges,” in *Proceedings of the Seventh International Conference on Antennas and Propagation (ICAP 91)*, 15–18 April 1991, vol. 1, pp. 99–108.

[27] R. C. Johnson, H. A. Ecker, and R. A. Moore, “Compact range techniques and measurements,” *IEEE Transactions on Antennas and Propagation*, vol. 17, no. 5, pp. 568–576, 1969.

[28] C. G. Parini, “Radiation pattern measurements of electrically large antennas using a compact antenna test range at 180 GHz,” *Electronics Letters*, vol. 24, no. 25, pp. 1552–1554, 1988.

[29] J. Habersack, H.-J. Steiner, and E. Dudok, “Millimetre wave application up to 204 GHz of the compensated compact range,” in *IEE Colloquium on Antenna Measurements using the Compact Antenna Test Range*, 25 Jan. 1991, pp. 3/1–3/7.

[30] J. Hartmann, J. Habersack, H.-J. Steiner, J. Lemanczyk, and P. de Maagt, “Calibration and verification measurements in compensated compact ranges up to 500 GHz,” in *Proceedings of 23rd AMTA*, Denver, USA, Oct. 2001, pp. 377–382.

[31] A. Lehto and A. Räisänen, *Mikroaaltomittaustekniikka* (in Finnish), Otatieto, No. 875, Helsinki 2001, 215 p.

[32] V. J. Vokurka, “Compact-antenna range performance at 70 GHz,” in *Proceedings of the IEEE Antennas and Propagation Society Symposium*, Quebec, Canada, vol. 1, 1980, pp. 260–263.

[33] C. W. Pistorius, G. C. Clerici, and W. D. Burnside, ”A dual chamber Gregorian subreflector system for compact range applications,” *IEEE Transactions on Antennas and Propagation*, vol. 37, no. 3, pp. 305–313, 1989.

[34] V. Galindo-Israel, S. R. Rengarajan, W. A. Imbriale, and R. Mittra, “Offset dual-shaped reflectors for dual chamber compact ranges,” *IEEE Transactions on Antennas and Propagation*, vol. 39, no. 7, pp. 1007–1013, 1991.

[35] J. R. Descardeci and C. G. Parini, “Trireflector compact antenna test range,” *IEE Proceedings Microwaves, Antennas and Propagation*, vol. 144, no. 5, pp. 305–310, 1997.

[36] C. Rieckmann, M. R. Rayner, and C. G. Parini, “Optimisation of cross-polarisation performance for tri-reflector CATR with spherical main reflector,” *Electronic Letters*, vol. 35, pp. 1403–1404, 1999.

[37] Y. Mizugutch, M. Akagawa, and H. Yokoi, “Offset dual reflector antenna,” in *Proceedings of Antennas and Propagation Society International Symposium*, vol. 14, 1976, pp. 2–5.

[38] H. H. S. Luh, “Equivalent hyperboloid (ellipsoid) and its application,” *IEEE Transactions on Antennas and Propagation*, vol. 48, no. 4, pp. 581–584, April 2000.

[39] T.-H. Lee and W. D. Burnside, “Performance trade-off between serrated edge and blended rolled edge compact range reflectors,” *IEEE Transactions on Antennas and Propagation*, vol. 44, no. 1, pp. 87–96, Jan. 1996.

[40] J. R. Mentzer, “The use of dielectric lenses in reflection measurements,” *Proceedings of the IRE*, 41, Feb 1953, pp. 252–256.

[41] A. D. Olver and A. A. Saleeb, “Lens type compact antenna range,” *Electronics Letters*, vol. 15, pp. 409–410, 1979.

[42] T. Hirvonen, J. Tuovinen, and A. Räisänen, “Lens-type compact antenna test range at mm-waves,” in *Proceedings of the 21st European Microwave Conference*, Stuttgart, Germany, 1991, pp. 1079–1083.

[43] J. J. Lee, “Dielectric lens shaping and coma correction zoning, Part 1: Analysis,” *IEEE Transactions on Antennas and Propagation*, AP-31, no. 1, pp. 211–216, 1983.

[44] T. Koskinen, *Studies on an amplitude hologram as the collimator in a submillimeter-wave compact antenna test range*, Doctoral Thesis, Helsinki University of Technology, 2007, 70 p. Available: URL: http://lib.tkk.fi/Diss/2007/isbn9789512287963/.

[45] A. Lönnqvist, J. Mallat, and A. V. Räisänen, "A phase hologram based compact RCS range for scale models," in *Proceedings of the 25th Annual Meeting & Symposium of the Antenna Measurement Techniques Association (AMTA)*, October 19–20, 2003, Irvine, CA, pp. 118–123.

[46] J. Meltaus, J. Salo, E. Noponen, M. M. Salomaa, V. Viikari, A. Lönnqvist, T. Koskinen, J. Säily, J. Häkli, J. Ala-Laurinaho, J. Mallat, and A. V. Räisänen, "Millimeter-wave beam shaping using holograms," *IEEE Transactions on Microwave Theory and Techniques*, vol. 51, no. 4, pp. 1274–1280, Apr. 2003.

[47] E. Noponen, J. Häkli, T. Koskinen, A. Lönnqvist, V. Viikari, J. Ala-Laurinaho, J. Mallat, and A. V. Räisänen, "Synthesis of reflector-type phase hologram for compact antenna test range at 310 GHz," in *Proceedings of 4th ESA Workshop on Millimetre-Wave Technology and Applications 8th Topical Symposium on Millimeter Waves – TSMMW2006 7th Millimeter-Wave International Symposium – MINT-MIS2006*, 15–17 February 2006, Espoo, Finland, pp. 391–396.

[48] J. Ala-Laurinaho, T. Sehm, J. Säily, and A. V. Räisänen, "Cross-polarization performance of the hologram compact antenna test range," *Microwave and Optical Technology Letters*, vol. 27, no. 4, pp. 225–229, Nov. 2000.

[49] T. Sehm, A. Lehto, and A. V. Räisänen, "A large planar antenna consisting of an array of waveguide fed horns," in *Proceedings of 26th European Microwave Conference*, 9-12 September 1996, Prague, Czech Republic, vol. 2, pp. 610–613.

[50] F. von Schéele, "The Swedish Odin satellite to eye heaven and earth," *47th International Astronautical Congress*, IAF, October 1996.

[51] A. Lönnqvist, T. Koskinen, J. Häkli, J. Säily, J. Ala-Laurinaho, J. Mallat, V. Viikari, J. Tuovinen, and A. V. Räisänen, "Hologram-based compact range for submillimeter-wave antenna testing," *IEEE Transactions on Antennas and Propagation*, vol. 53, pp. 3151–3159, 2005.

[52] T. Koskinen, J. Ala-Laurinaho, J. Häkli, and A. V. Räisänen, "Studies on an amplitude hologram as a submillimeter-wave collimator at circular polarisation," in *Proc. European Conference on Antennas & Propagation (EuCAP)*, Nice, France, Nov. 6–10, 2006, CD-ROM, ISBN: 92-9092-937.

[53] T. Koskinen, J. Häkli, J. Ala-Laurinaho, A. Lönnqvist, V. Viikari, J. Mallat, and A. V. Räisänen, "Study on the dual polarized operation of the hologram based compact antenna test range," in *Proceedings of 28th ESA Antenna Workshop on Space Antenna Systems and Technologies*, ESTEC, Noordwijk, The Netherlands, May 31 – June 3, 2005, pp. 401–406.

[54] I. Lindell and K. Nikoskinen, *Antenniteoria* (in Finnish), Otatieto, no. 848, Helsinki 1997, 347 p.

[55] R. E. Collin, *Antennas and Radiowave Propagation*, McGraw-Hill Book Company, United States of America, 1985, 508 p.

[56] K. Pontoppidan, *Technical Description of GRASP8*, Ticra engineering consultants, 2003, 376 p.

[57] P. M. Johansen, "Uniform physical theory of diffraction equivalent edge currents for truncated wedge strips," *IEEE Transactions on Antennas and Propagation*, vol. 44, no. 7, pp. 989–995, July 1996.

[58] M. Kline and I. W. Kay, *Electromagnetic theory and geometrical optics*, John Wiley & Sons, Inc., New York, United States of America, 1965, 527 p.

[59] V. Jamnejad-Dailami and Y. Rahmat-Samii, "Some important geometrical features of conic-section-generated offset reflector antennas," *IEEE Transactions on Antennas and Propagation*, AP-28, no. 6, pp. 952–957, Nov. 1980.

[60] R. A. Shore, "A simple derivation of the basic design equation for offset dual reflector antennas with rotational symmetry and zero cross-polarization," *IEEE Transactions on Antennas and Propagation*, AP-33, no 1, pp. 114–116, Jan. 1985.

[61] R. Sauleau, C. A. Fernandes, and J. R. Costa, "Review of lens antenna design and technologies for mm-wave shaped-beam applications," *ANTEM 2005*, Saint Malo, France, June 15–17, 2005, pp. 414–416.

[62] D. F. Filipovic, S. S. Gearhart, and G. M. Rebeiz, "Double-slot antennas on extended hemispherical and elliptical silicon dielectric lenses," *IEEE Transactions on Microwave Theory and Techniques*, vol. 41, no. 10, pp. 1738–1749, Oct. 1993.

[63] H. Mosallaei and Y. Rahmat-Samii, "Non-uniform luneburg and two-shell lens antennas: radiation characteristics and design optimization," *IEEE Transactions on Antennas and Propagation*, vol. 49, no. 1, pp. 60–69, Jan. 2001.

[64] A. D. Greenwood and J. Jian-Ming, "A field picture of wave propagation in inhomogeneous dielectric lenses," *IEEE Antennas and Propagation Magazine*, vol. 41, no. 5, pp. 9–18, Oct. 1999.

[65] V. Galindo, "Design of dual reflector antennas with arbitrary phase and amplitude distribution," *IEEE Transactions on Antennas and Propagation*, vol. AP-12, pp. 403–408, July 1964.

[66] B. S. Westcott, F. A. Stevens, and F. Brickell, "GO synthesis of offset dual reflectors," *IEE Proceedings*, vol. 128, pp. 11–18, 1981.

[67] G. Bjøntegaard and T. Pettersen, "An offset dual-reflector antenna shaped from near-field measurements," *IEEE Transactions on Antennas and Propagation*, vol. 31, no. 6, pp. 973–977, Nov. 1983.

[68] J. Bergman, R. C. Brown, P. J. B. Clarricoats, and H. Zhou, "Synthesis of shaped-beam reflector antenna patterns," *IEE Proceedings*, vol. 135, Pt. H, no.1, pp. 48–53, Feb. 1988.

[69] B. S. Westcott, A. A. Zaporozhets, and A. D. Searle, "Smooth aperture distribution synthesis for shaped beam reflector antennas," *Electronic Letters*, vol. 14, no. 14, pp. 1275–1276, July 1993.

[70] D.-W. Duan and Y. Rahmat-Samii, "A generalized diffraction synthesis technique for high performance reflector antennas," *IEEE Transactions on Antennas and Propagation*, vol. 43, no. 1, pp. 27–40, Jan. 1995.

[71] S. G. Hay, "Dual-shaped-reflector directivity pattern synthesis using the successive projections method," *IEE Proceedings - Microwaves, Antennas and Propagation*, vol. 146, no. 2, pp. 119–124, Apr. 1999.

[72] J. J. Lee, L. I. Parad, and R. S. Chu, "A shaped offset-fed dual-reflector antenna," *IEEE Transactions on Antennas and Propagation*, vol. AP-27, no. 2, 1979, pp. 165–171, 1979.

[73] P.-S. Kildal, "Synthesis of multireflector antennas by kinematic and dynamic ray tracing," *IEEE Transactions on Antennas and Propagation*, vol. 38, no. 10, pp. 1587–1599, Oct. 1990.

[74] J. O. Rubiños-Lòpez and A. García-Pino, "A ray-by-ray algorithm for shaping dual-offset reflector antennas," *Microwave and Optical Technology Letters*, vol. 15, no. 1, pp. 20–26, May 1997.

[75] C. A. Fernandes, "Shaped dielectric lenses for wireless millimeter-wave communications," *IEEE Antennas and Propagation Magazine*, vol. 41, no. 5, pp. 141–150, Oct. 1999.

[76] C. A. Fernandes and L. M. Anunciada, "Constant flux illumination of square cells for mm-wave wireless communications," *IEEE Transactions on Microwave Theory and Techniques*, vol. 49, no. 11, pp. 2137–2141, Nov. 2001.

[77] M. Silveirinha and C. A. Fernandes, "Shaped double-shell dielectric lenses for wireless millimeter wave communications," in *Proceedings of 2000 IEEE AP-S International Symposium*, Salt Lake City, Utah, July 2000, pp. 1674–1677.

[78] B. Chantraine-Barès, R. Sauleau, L. Le Coq, and K. Mahdjoubi, "A new accurate design method for millimeter-wave homogeneous dielectric substrate lens antennas of arbitrary shape," *IEEE Transactions on Antennas and Propagation*, vol. 53, no. 3, pp. 1069–1082, March 2005.

[79] D. K. Waineo, "Lens design for arbitrary aperture illumination," in *Proceedings of Antennas and Propagation Society International Symposium*, 1976, Amherst, Mass., U.S.A., pp. 476–479.

[80] J. Thornton, "A low sidelobe asymmetric beam antenna for high altitude platform communications," *IEEE Microwave and Wireless Components Letters*, vol. 14, no. 2, pp. 59–61, Feb. 2004.

[81] T. Maruyama, K. Yamamori, and Y. Kuwahara, "Design of multibeam dielectric lens antennas by multiobjective optimization," *IEEE Transactions on Antennas and Propagation*, vol. 57, no. 1, pp. 57–63, Jan. 2009.

[82] J. Tuovinen, T. M. Hirvonen, and A. V. Räisänen, "Near-field analysis of a thick lens and horn combination: theory and measurements," *IEEE Transactions on Antennas and Propagation*, vol. 40, no. 6, pp. 613–619, June 1992.

[83] A. V. Räisänen and A. Lehto, *Radio Engineering for Wireless Communication and Sensor Applications*, Artech House, Boston 2003, 396 p.

[84] Ticra engineering consultants, Available: http://www.ticra.com/

[85] A. Karttunen, M. Vaaja, and A. V. Räisänen, "Antenna measurement at 650 GHz with a planar near-field scanner," in *Proceedings of the 29th Annual Antenna Measurement Techniques Association (AMTA) Meeting & Symposium*, St. Louis, MO, USA, Nov. 4–9, 2007, pp. 330–336.

[86] M. Vaaja, J. Häkli, J. Mallat, and A. V. Räisänen, "Assessment of a planar near-field range for quiet-zone measurements at 650 GHz," in *Proceedings of the 29th Annual Antenna Measurement Techniques Association (AMTA) Meeting & Symposium*, St. Louis, MO, USA, Nov. 4–9, 2007, pp. 325–329.